Realia et naturalia

DISSERTATIONES
CHIMICAE
UNIVERSITATIS
TARTUENSIS
148

ERIK ANDERSON

In situ Scanning Tunnelling Microscopy studies of the interfacial structure between Bi(111) electrode and a room temperature ionic liquid

TARTU ÜLIKOOL · UNIVERSITAS TARTUENSIS · 1632

DISSERTATIONES CHIMICAE UNIVERSITATIS TARTUENSIS
148

DISSERTATIONES CHIMICAE UNIVERSITATIS TARTUENSIS

148

ERIK ANDERSON

In situ Scanning Tunnelling Microscopy studies of the interfacial structure between Bi(111) electrode and a room temperature ionic liquid

UNIVERSITY OF TARTU
PRESS

Institute of Chemistry, Faculty of Science and Technology, University of Tartu, Estonia

Dissertation is accepted for the commencement of the degree of Doctor of Philosophy in Chemistry on June 25th, 2015 by the Council of Institute of Chemistry, University of Tartu.

Supervisors:	Prof. Enn Lust Institute of Chemistry, University of Tartu, Estonia
Opponent:	Prof. Pawel J. Kulesza Department of Chemistry, University of Warsaw, Poland
Commencement:	August 28th, 2015, at 16:00 14a Ravila Street, Tartu (Chemicum), auditorium 1021

Publication of this thesis is granted by the Institute of Chemistry, University of Tartu

European Union
European Social Fund

Investing in your future

ISSN 1406-0299
ISBN 978-9949-32-893-2 (print)
ISBN 978-9949-32-894-9 (pdf)

University of Tartu Press
www.tyk.ee

TABLE OF CONTENTS

LIST OF ORIGINAL PUBLICATIONS

1. E. Lust, R. Küngas, I. Kivi, H. Kurig, P. Möller, E. Anderson, K. Lust, K. Tamm, A. Samussenko, G. Nurk, Electrochemical and gas phase parameters of cathodes for intermediate temperature solid oxide fuel cells, Electrochim. Acta 55, 7669–7678 (2010).

2. **E. Anderson**, V. Grozovski, L. Siinor, C. Siimenson, V. Ivaništšev, K. Lust, S. Kallip, E. Lust, Influence of the electrode potential and *in situ* STM scanning conditions on the phase boundary structure of the single crystal Bi(111) | 1-butyl-4-methylpyridinium tetrafluoroborate interface, J. of Electroanal. Chem. 709, 46–56 (2013).

3. **E. Anderson**, V. Grozovski, L. Siinor, C. Siimenson, E. Lust, *In situ* STM studies of Bi(111) | 1-ethyl-3-methyl-imidazolium tetrafluoroborate + 1-ethyl-3-methylimidazolium iodide interface, J. of Electrochem. Commun. 46, 18–21 (2014).

Author's contribution:

1. Performed all scanning probe microscopy and cyclic voltammetry measurements and results analysis of Papers 1.–3.
2. Attended to text preparations, except the measurements of electrochemical impedance spectra of Papers 1.–3.

ABBREVIATIONS AND SYMBOLS USED

in situ	measurement under specific and / or unique or changing conditions
STM	scanning tunnelling microscopy
AFM	atomic force microscopy
C(0001)	basal plane of a graphite electrode
EDL	electrical double layer
EDLC	electrical double layer capacitor
HSC	hybrid supercapacitor
RTIL	room temperature ionic liquid
ΔE	potential region of ideal polarisability
NAS	non-aqueous solvent
E_{max}	maximum specific energy
P_{max}	maximum specific power
(*hkl*	the notation of the Bi or Au crystallographic plane (index)
EIS	electrochemical impedance spectroscopy
CV	cyclic voltammetry
HOPG	highly oriented pyrolytic graphite
HOPG(0001)	highly oriented pyrolytic graphite basal plane
E	electrode potential
RMS	root mean square roughness
$\mathrm{BMPyBF_4}$	1-butyl-4-methylpyridinium tetrafluoroborate
$\mathrm{EMImBF_4}$	1-ethyl-3-methylimidazolium tetrafluoroborate
$\mathrm{EMImBF_4}$ + EMImI	a mixture of $\mathrm{EMImBF_4}$ + 1-ethyl-3-methylimidazolium iodide
σ	surface charge density of an electrode
ε	dielectric constant
R(σ)	Debye-length-dependent electrochemical roughness
t	experimental time
$E_{\sigma=0}$	potential of zero charge
υ	potential sweep rate
i	current in an electrochemical system
q	electrode charge
R_{s}	solution resistance or high-frequency series resistance
C_{d}	capacitance of an electrical double layer
R	current resistance
I	flow of an electrical current
Z	complex impedance
ac	alternating current
E_{t}	value of potential E at time t
E_0	amplitude of a signal
ω	radial frequency
f	frequency

Φ	phase shift
I_t	value of current I at time t
I_0	amplitude of an ac current signal
Z_0	magnitude of impedance
j	imaginary unit, (j = √-1)
Z'	real part of impedance
Z''	imaginary part of impedance
EC	equivalent circuit
Z_w	Warburg impedance
δ	thickness of Nernstian diffusion layer
D	average value of diffusion coefficients
V	bias between tip and a substrate
x	distance between tip and a sample
R_tunnel	resistance of a tunnelling gap
E_tip	bias between tip and a substrate
WE	working electrode
CE	counter electrode
RE	reference electrode
E_WE	potential of a working electrode
i_tunnel	tunnelling current
υ_scan	image scanning rate
j	current density
C_s	series capacitance
R_d	mass transfer resistance
R_ct	charge transfer resistance
C_dl	high-frequency capacitance
C_ad	low-frequency capacitance
ε_0	dielectric constant of vacuum
d	effective thickness of an electrical double layer region
R_1	high frequency series resistance
C_p	parallel capacitance
τ_ch	characteristic time constant
$S(\omega)$	complex power
$P(\omega)$	active power (*i.e.* real) component of the complex power
$Q(\omega)$	reactive (*i.e.* imaginary) component of the complex power
t_pol	polarisation time
FTT	fast Fourier transform filtering technique
SOFC	solid oxide fuel cell
GD	grain distribution calculation method
T_sint	sintering temperature

I INTRODUCTION

Ionic liquids are electrolytes with the growing potential, being widely applied in many areas of science: in synthesis, deposition of noble metals and galvanic coatings, as electrolytes in supercapacitors, dye-sensitized solar cells, batteries and electrolysers, as well as solvents for various technological processes *etc*. Nowadays there are an infinite number of combinations of cations and anions that can be combined as novel ionic liquids with tuneable characteristics.

The surface properties of ionic liquids have been studied only in the case of a few metals, and therefore, the classical theories about the electrical double layer structure formation and their properties in the conditions of changing electrical field on atomically flat electrodes are often incomplete.

Scanning probe microscopy is a very informative tool for studying the solid electrode | electrolyte interface in general. High resolution *in situ* scanning tunnelling microscopy (STM) and atomic force microscopy (AFM) are the most powerful but simple analytical methods for investigation of the interfacial structure at electrode | electrolyte interface in real time and at the atomic or molecular level. However, only the modest number of studies which combine the results obtained with *in situ* STM and other surface sensitive electrochemical or crystallographic methods have been published so far.

During the past 30 years, single crystal and polycrystalline bismuth electrodes and their application in electrochemical kinetics and electro analysis studies have been of a great interest for the scientists at University of Tartu. Due to quick technological progress in the materials purification and production of metal single crystals it is nowadays essentially possible to obtain nearly perfectly atomically flat crystal surfaces, including Bi(111) electrodes.

The main aim of this work was to study the electrochemical behaviour and interfacial structure of three ionic liquids at Bi(111) electrodes with the *in situ* STM method. Cyclic voltammetry and electrochemical impedance methods have been used as complementary methods for a detailed analysis of the electrical double layer structure, adsorption kinetics and specific adsorption of I^- ions at the electrochemically polished and cleaved Bi(111) surface.

II LITERATURE OVERVIEW

2.1 General background

The structure of electrical double layer (EDL) at metal | electrolyte interface influences many important applications of electrochemistry, including design of electrical double layer capacitors (EDLC) and hybrid supercapacitors (HSC), corrosion-protective layers, fuel cells, battery-type devices, electrolysers, dye-sensitised solar cells and CO_2 electro reduction devices [1–18]. In the recent years, ionic liquids have been extensively studied as electrolytes applicable in these various modern technological devices. Use of the non-aqueous electrolytes and room temperature ionic liquids (RTIL) [19] in EDLCs has been initiated by the wider region of ideal polarisability of carbon electrodes (cell potential ΔE up to 3.6 V [15–21] compared to aqueous solutions). Application of RTILs with small additions of the non-aqueous solvents (NAS) (so-called RTIL + NAS mixtures) as an electrolyte has been initiated by the lower viscosity of RTIL + NAS mixtures, increase in ΔE, if compared with those based on the aqueous electrolytes [22–24]. Thus, for exponential increase in the maximum energy-density, $E_{\max}$, and power-density, $P_{\max}$, being both proportional to ΔE^2 of the EDLC. Our recent research, therefore, has been focused on using the RTILs, non-aqueous electrolytes and the RTIL + NAS mixtures as electrolytes for the high energy- and power density EDLCs based on the specially designed microporous–mesoporous carbon electrodes with hierarchical porous structure [15–21].

The high resolution microscopy studies combined with electrochemical measurements of a porous carbon electrode | RTIL interface are more complicated, time consuming and expensive, thus, some testing measurements have been carried out using the cleaved and electrochemically polished atomically flat Bi(111) electrodes [25,26]. Due to the absence of fundamental information on the influence of surface roughness of the carbon electrodes on the energy density and power density of supercapacitors, fuel cells and battery-type systems, the new experimental studies analysing the EDL structure at metal | ionic liquid interface, including analysis of the nano-roughness effects, are essential. Due to the technological progress, in the production and purification of single elements in recent years, sufficient prerequisites are met to produce nearly ideal single crystals for almost each element with highest purity (up to 99.999% and even higher). Therefore, the EDL structure at cleaved and electrochemically polished Bi(111) electrode | RTIL interface within wide region of electrode potentials has been studied in this work.

Wider application of RTILs is still hindered by limited fundamental understanding of the structural characteristics of interface between the electrode material and RTIL [27–35]. Only a few complex studies combining the electrochemical impedance spectroscopy (EIS) [1,3,36] and *in situ* scanning tunnelling microscopy (STM) [34,37] have been published so far. Influence of temperature and crystallographic structure of the metal single crystal plane electrode on the properties of the electrode | RTIL interface has been rarely studied [1,34,38,39], especially by the *in situ* STM or Atomic Force Microscopy (AFM) method combined with electrochemical methods for electrodes other than Au(*hkl*) or highly oriented pyrolytic graphite (HOPG(0001)).

However, the EDL structure [1] of the interface between a solid electrode and a RTIL [11,15,16,34,40–44] or a mixture of RTILs depends strongly on the chemical composition of RTIL cations and anions, as well as on the electrode potential, *E*, applied [8,45]. The structure of EDL depends also on the chemical nature of the electrode material (amorphous carbon, HOPG, carbon nanotubes, Pt-group metals, semi-metals (bismuth, antimony) cadmium [1,8,11,14–16,30,34,40–46]), as well as on the surface structure of the single crystal electrode.

Based on the results for the interfaces between Au(*hkl*), Bi(*hkl*) and Cd(*hklf*) planes and aqueous or non-aqueous electrolyte solutions [39,47–49], it can be concluded that the chemical composition, the crystallographic structure and the atomic-scale roughness [1,3,4,36,46] of electrode considerably influence the parameters of EDL and adsorption layer structural kinetics. The adsorption kinetics of molecules and ions on the chemically different metal electrodes, and even on various single crystal planes of the same metal is also affected by the crystallographic structure of the surface [1,2,4,5,47–49,51]. The atomically flat adsorption layers (including the 2D-layers), which exhibit a higher order of regularity, have only been observed for crystallographically nearly ideal metal surfaces, *i.e.* Au(*hkl*) [1,46–48,51,52], and Bi(*hkl*) planes [1,3,36,46,49,53,54].

In addition, based on the analysis of the experimental data [1,46,55,56], the real geometric surface structure in a nanoscopic scale has a decisive influence on the root mean square roughness (RMS) value of the system analysed. By applying *in situ* STM method, it was demonstrated that very slow adsorption layer reorganisation processes occur at the Bi(111) | 1-butyl-4-methyl-pyridinium tetrafluoroborate ($BMPyBF_4$), Bi(111) | 1-ethyl-3-methylimidazolium tetrafluoroborate ($EMImBF_4$) and Bi(111) | $EMImBF_4$ + 1-ethyl-3-methylimidazolium iodide (EMImI) interface after the shift of the electrode surface charge density (σ) from moderately negative to moderately positive surface charge values [40]. Cyclic voltammetry (CV) and EIS measurements demonstrated [40,56] that the structure of EDL and adsorption kinetics of $EMIm^+$ cations and I^- anions are strongly influenced by σ, explained by the specific adsorption of I^- ions at HOPG(0001) or Bi(111) from a mixture of $EMImBF_4$ and EMImI.

The interface of Au(*hkl*) | aqueous electrolyte solution has been intensely studied [1,14,34,51,52] and theoretically explained by Kornyshev and Vilfan [57]. Systematic theoretical analysis of the phase transition, physical adsorption−desorption and specific adsorption effects on the electrode | RTIL interface has been given by Kirchner *et al.* [58]. In comparison to Au(111) electrode, the Bi(111) electrode is known to be catalytically, chemically and electrochemically inactive, thus, the high stability is also expected for a Bi(111) | RTIL interface. There is no surface reconstruction induced by the electric field strength changes as well as diffusion of the surface atoms on the Bi(111) surface, unlike on Au(*hkl*) or Pt group metals [1,34,36,37,41–44,48,51–56]. Therefore, only reorganisation process of the adsorption layer is possible, including specific adsorption effects of the ions. For these reasons, the Bi(111) electrode has been selected as an electrode material in this work.

The Bi electrode is less toxic than Hg [1,3,36] and it has been proposed as a replacement of the thin layer mercury electrode for the analysis of heavy metal cations [59–61]. Due to its rhombohedral symmetry, layered structure, and van der Waals bonding between the neighbouring bilayers, the Bi(111) surface has also a number of similarities to the basal (0001) carbon plane [1,4,25,26,53,54]. In order to obtain the fresh electrode surface it is possible to cleave the Bi(111) electrode at the temperature of liquid nitrogen, which yields atomically flat surface structure comparable with a cleaved HOPG, *i.e.* the C(0001) plane. Because of the covalent bonding within atomic double layers, the surface structure of Bi is very stable under the conditions of electrochemical polarisation during many hours in aqueous and non-aqueous electrolytes [1,4,14,25,26,34,51–54].

Bi as a semimetal is characterised by high dielectric constant (ε = 78 or 200, dependent on the crystallographic orientation) and by the low concentration of free charge carriers with the high effective mass, [1,3,4,36,37] similarly to C(0001) electrode.

The crystallographic structure of the Bi(*hkl*) electrode has been thoroughly characterised in the atomic scale by *in situ* AFM and STM methods [1,3,4,4–7,40,50,62]. Its crystallographic structure essentially influences the values of so-called Debye-length-dependent electrochemical roughness R(σ) values, theoretically discussed by Daikhin *et al.* [2], and experimentally analysed by Lust *et al.* [1,46]. It was demonstrated that the Debye-length dependent surface roughness is an effective parameter depending on the electrolyte concentration and on the electrode potential (*E*) applied [1,2,46]. A noticeable influence of *E* and electrolyte concentration on specially and specifically roughened Bi, Cd and Sb single crystal surfaces [1,46,55] was shown experimentally based on the root mean square roughness and effective roughness R(σ) data, calculated from the impedance spectra. It was found that the effective surface roughness and adsorption activity of ions depends on the size (linear-dimension) of the ions forming the EDL. Therefore, for the more detailed analysis of interfacial structure the smaller cations based RTILs (like ethyl-methylimidazolium cation, $EMIm^+$, ethyl-methylpyrimidinium cation, $EMPy^+$, *etc.*) with very high concentration of ions have been tested in this work.

The first aim of this work was to investigate the influence of the electrode potential on the interfacial layer structure at the Bi(111) | $EMImBF_4$, Bi(111) | $BMPyBF_4$ and Bi(111) | $EMImBF_4$ + EMImI mixture phase boundaries [1,4,36,46] as the electrical conductivity and the electrochemical stability regions of these RTILs [17,18,32] are suitable for their application in EDLCs and HSCs. The region of ideal polarisability and potential of zero charge for Bi(111) electrode in three RTILs have been estimated and established based on CV and EIS data, respectively. The specific adsorption of I^- anions, already known from the EIS and CV data [45], was verified by high-resolution *in situ* STM method in the region of potentials characteristic of specific iodide anions adsorption at Bi(111) electrode surface from a mixture of RTILs [45,62].

The second aim was to analyse the dependence of EDL formation / rearrangement kinetics on Bi(111), based on the EIS data, also dependent on *E* applied. It is clear that, if the formation / reorganisation kinetics of EDL is slow at the atomically flat Bi(111) electrode [1,4,53,54], then these RTILs are not attractive as potential electrolytes for the high power-density EDLCs, based on micro-mesoporous electrodes, where mass transfer in the porous structure is very low.

2.2 Cyclic Voltammetry

Cyclic voltammetry is a simple method for electrochemical analysis of electrodes. To collect comprehensive information it is significantly easier and less time-consuming method compared to EIS or *in situ* STM methods. Its instrumental setup is also more user friendly along with interpretation step of the CV data. In this work, the main aim of CV studies was to determine the region of ideal polarisability and the limiting values of *E* and currents, applicable within ideal region of polarisation, before conducting the more time consuming EIS and *in situ* STM measurements. Hence, a brief overview is provided below.

A linear potential sweep is known as a potential applied (*E*) that changes linearly with time, *t*. It is written as:

$$E = \upsilon t \tag{1}$$

Here, υ is the potential sweep rate (mV/s). If the linear potential sweep is applied to an RC circuit (Fig. 1a) [63], the Eq. (2) applies:

$$\upsilon t = iR_s + \frac{q}{C_d} \tag{2}$$

In Eq. (2), *i* is defined as the change of current during a time interval *dt*, *i.e.* $i = dq / dt$, where *q* is charge. R_s is the solution resistance, and C_d is the capacitance of the EDL. Hence, the Eq. (3) can be obtained [63]:

$$\upsilon t = \frac{dq}{dt} R_s + \frac{q}{C_d} \tag{3}$$

At the starting point $t = 0$ and $q = 0$, a following Eq. is obtained (by using Eq. (3)):

$$i = \upsilon C_d \left(1 - e^{\left(\frac{-t}{R_s C_d} \right)} \right) \tag{4}$$

In Eq. (4), R_sC_d component is a time constant and υC_d is a steady-state value of the current. It should be noted that R_sC_d decays exponentially in time. When a triangular wave is applied to an RC circuit (Fig. 1b), *i.e.*, a ramp is applied whose sweep changes from a positive potential to the opposite (negative) potential, then the steady-state current changes from υC_d to $-\upsilon C_d$. C_d does not depend significantly on E applied, thus, C_d can be viewed as a constant. After applying mathematical filtering methods, a cyclic voltammogram, *i.e.* current *vs.* potential (i, E) dependency is obtained [63].

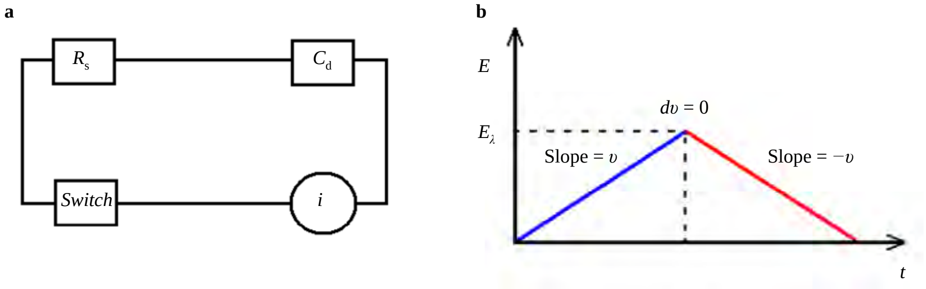

Figure 1. A current step diagram of an RC circuit (a), and a potential-time plot resulting from a cyclic linear potential sweep (triangular wave) to an RC circuit (b) [63]. Here i is a constant current source and E_λ corresponds to a switching potential for CV, respectively.

A typical shape of a voltammogram measured on a clean surface of a metal in a surface inactive electrolyte (in our case on Bi(111) electrode in $EMImBF_4$) is shown in Fig. 3a. A voltammogram demonstrated in Fig. 3b exhibits the additional peaks and higher currents, which are characteristic of the adsorption / oxidation / reduction processes of substances at the interface (iodine / iodide anion reactions).

In the case of aqueous solutions, there is an area of hydrogen evolution at the high negative potentials $\sim E \leq -1.0$ V or $\sim E \leq -1.2$ V *vs.* Ag | AgCl for Bi(111) | 0.5 M Na_2SO_4 + x M H_2SO_4 interface, depending somewhat on whether H_2 is used for the deaeration process of the solutions or not, respectively. In this region of E, the cathodic (reduction) current decreases exponentially. In the case of RTILs, the trace H_2O always exists in a RTIL, however, its concentration in the electrolyte phase is limited. As a result, a breakdown of water molecules rather occurs along with the formation of HF and other intermediates and products. If E is negative enough, a polymerisation process of a RTIL cation mainly over reduction reaction occurs [64].

It is important to note that for the noble metals, the additional peaks of processes can be observed explained mainly by reconstruction of the electrode surface, but for Bi(*hkl*), Sb(*hkl*) and Cd(*hklf*) electrodes, there is no evidences of surface reconstruction because no such peaks exist in this region of E studied [3–7,40,50,62,65,66].

In the positive end of the CVs, the currents grow exponentially and it corresponds to an irreversible oxidation process of the metal surface along with the dissolution of a metal [40,62]. The shape of CVs in this case is comparable either in an aqueous solution or in a RTIL medium. The difference in the positive end of CVs, *i.e.* the currents can change significantly, if electroactive species adsorb−desorb on the surface or an electrochemical reaction occurs [3,5,37,56]. In the case of Bi(111) | EMImBF$_4$ + EMImI interface, the redox reactions of iodine / iodide anions occur at ~$E > -0.2$ V. However, at the same $E = -0.2$ V, the surface of Bi(111) is suspected to slowly oxidise after the protecting iodide anions 2D-layer has been removed in some areas of the electrode surface by applying a positive E (Fig. 3b). Therefore, the additional peaks corresponding to initial oxide formation and dissolution processes are observed in the CV data for a RTIL mixture.

The area of E between the positive and negative exponential current growth areas is called as the region of an ideal polarisability [63]. The electrochemical processes in this region are mostly reversible and only the background currents flow mainly due to the parasitic reactions from trace impurities along with the small leakage currents of an electrode. The probability of charge transfer (faradic) reactions in this region of E is nearly zero [63].

2.3 Electrochemical Impedance Spectroscopy

In this paragraph, only basic concepts of the EIS measurements are briefly explained [67–69]. The detailed analysis of the modelled spectra to the experimental spectra can be found in the chapters VI.2 and VI.3.

Impedance, Z, of the circuit element is defined by its ability to resist the flow of electrical current, I. Resistance, R, is defined by Ohm's law (5) in terms of the ratio between voltage, E, and I. This Formula can only be used for a simple resistor:

$$R = \frac{E}{I} \tag{5}$$

Electrochemical impedance is measured by applying alternating current (ac) to an electrochemical cell and then measuring the current flow through the cell. During EIS measurements a sinusoidal excitation potential is applied. It can be written as:

$$E_t = E_0 \sin(\omega t)\,, \tag{6}$$

where E_t is the value of potential at time t, E_0 is the amplitude of the signal (V), and ω is the radial frequency (radians/s). There is a dependency between ac frequency, f, and ω:

$$\omega = 2\pi f \tag{7}$$

As a result, a sinusoidal ac current signal (I) is collected with the difference of the phase shift (Φ). Therefore, it has different amplitude, I_0:

$$I_t = I_0 \sin(\omega t + \Phi) \tag{8}$$

The expression for Z based on the Ohm's law (5), and Eq.-s (6) and (8) is:

$$Z = \frac{E}{I} = \frac{E_0 \sin(\omega t)}{I_0 \sin(\omega t + \Phi)} = Z_0 \left(\frac{\sin(\omega t)}{\sin(\omega t + \Phi)} \right), \tag{9}$$

where Z_0 is a magnitude of the impedance. Euler's relationship (10) is then used to express Z as a complex function:

$$e^{(j\Phi)} = \cos\Phi + j\sin\Phi , \tag{10}$$

where j is the imaginary unit (j = √-1). The potential at any t is given:

$$E_t = E_0 e^{(j\omega t)} \tag{11}$$

Therefore, the current can be obtained as:

$$I_t = I_0 e^{(j\omega t - \Phi)} \tag{12}$$

Hence, the impedance can be represented as a complex number, $Z(\omega)$:

$$Z(\omega) = \frac{E}{I} = Z_0 e^{(j\Phi)} = Z_0(\cos\Phi + j\sin\Phi) \tag{13}$$

Thus, the expression (13) consists of a real and an imaginary part. When the real part of the impedance is plotted on the *x*-axis and the imaginary part is plotted on the *y*-axis, a typical Nyquist plot is obtained [67–69]. In the Nyquist plot, each point corresponds to the impedance at a certain frequency. In this work, the non-linear least squares data fitting method has been used for an analysis of Nyquist plots [68].

When the impedance is plotted *versus* log frequency on the *x*-axis, and both the magnitude of the impedance (Z_0) (also noted as $|Z|$), and the phase-shift (Φ) on the *y*-axis, a Bode plot is obtained.

Impedance data are commonly analysed by fitting to an equivalent electrical circuit model. Usually a common equivalent electrical circuit consists of the following elements: a resistor, a capacitor, an inductor, a diffusion element (Warburg diffusion-like impedance) connected either in a series or parallel way to form an Electrical Circuit (EC).

The impedance of the resistor has no imaginary part and Z (noted as Z' known as a real part of impedance) is independent of the frequency, therefore:

$$Z(\omega) = Z'(\omega) = R \tag{14}$$

For a capacitor, the impedance Z (noted as Z'' known as an imaginary part of impedance) is calculated using (15):

$$Z(\omega) = Z''(\omega) = \frac{1}{j\omega C} \tag{15}$$

The current through the resistor has a phase shift of 0°. Thus, the impedance for the capacitor element decreases, if the frequency rises. For an ideal capacitor, only an imaginary part of the impedance exists and the current through the capacitor has a phase shift of −90°.

For a Warburg element, the impedance depends on the frequency of ac potential perturbation. At high frequencies, diffusing reactants do not move significantly, hence the Warburg impedance is small. When the frequencies applied are low, then the reactants can move, therefore, increasing the Warburg impedance. Infinite Warburg impedance can be given as:

$$Z_W = \frac{\sigma_D (1 - j)}{\sqrt{\omega}} \tag{16}$$

In Nyquist (Z'', Z') plots, a Warburg element appears as a diagonal line with a slope of 45°, and in Bode plots at lower f it has a phase shift of −45°. The Eq. (16) is used for objects that have a very thick (so-called infinite) diffusion layer. In the Eq. (16), σ_D is a Warburg coefficient.

In this work, an EC named as a modified Frumkin − Melik-Gaikazyan is used for the data modelling. As the thickness of the diffusion layer is finite for a single crystal plane | RTIL interface, so the finite-length Warburg element (W_1) for short circuit conditions at $f \rightarrow 0$ can be applied in the modelling of the data. In this case the Formula (17) can be used:

$$Z_0 = \frac{\sigma_D (1 - j)}{\sqrt{\omega}} \tanh\left(\delta \left(\frac{j\omega}{D} \right)^{1/2} \right) \tag{17}$$

In Eq. (17), δ is the thickness of Nernstian diffusion layer, and D is an average value of the diffusion coefficients of the diffusing species.

2.4 Scanning Probe Microscopy

Electrochemical methods applied usually provide the statistically reproducible information over the surface of the working electrode, that is, general data about an electrode | electrolyte interface, but in many cases they lack the direct structural information of the processes occurring at these interfaces. It is also a complicated task to correlate the crystallographic data (single crystals, poly crystals, coatings, depositions and their structure *etc.*) with the fundamental data of electrochemistry (CVs, EIS spectra *etc.*) without supporting any surface analysis information obtained by using microscopic methods. For this reason, *in situ* STM was chosen as a main surface structure analysis method in this work.

STM was invented by Binning and Rohrer *et al.* in 1982 [70], and a few years later AFM was invented [71]. By now, a wide variety of scanning probe microscopy methods exists, and most of the investigations are conducted either in a liquid or in a vacuum medium. Thus, in many cases the potential and temperature and other physical and chemical parameters can be controlled. Many of these methods are combined nowadays, for example an AFM or STM tip enhanced Raman spectroscopy [72], a scanning high resolution STM at video frequency rate [73] *etc.*

The *in situ* STM method is specially designed for atomically flat surfaces that exhibit electronic conductance at reasonable conditions of electrochemical polarisation. Objects with free *s*- and *p*-electrons or vacant orbitals in their electron shell often have this property, *i.e.*, the atomically flat surfaces of most metals, semimetals, and some non-metals can be visualised by *in situ* STM method.

A sharp tip (etched or cut mainly from Pt- or W-wire) is brought extremely close to the conducting surface (a few nanometers and eventually less), and a potential difference is created between the two interfaces (Fig. 2a). As a result, the wave functions of two interfaces overlap, and an electron tunnelling phenomenon occurs [63]. The current flow through the STM tip can be given as an Eq. (18).

$$i_{tunnel} = (const)Ve^{(-2\beta x)} = \frac{V}{R_{tunnel}} \tag{18}$$

In Eq. (18), i_{tunnel} and x are tunnelling current and the distance between the tip and the sample, respectively. V is a tip-substrate bias (also noted as E_{tip} later in this work), R_{tunnel} is a resistance of a tunnelling gap, and β is a parameter depending on the energy barrier and work function properties of the interface, however, for shortness it is not considered here.

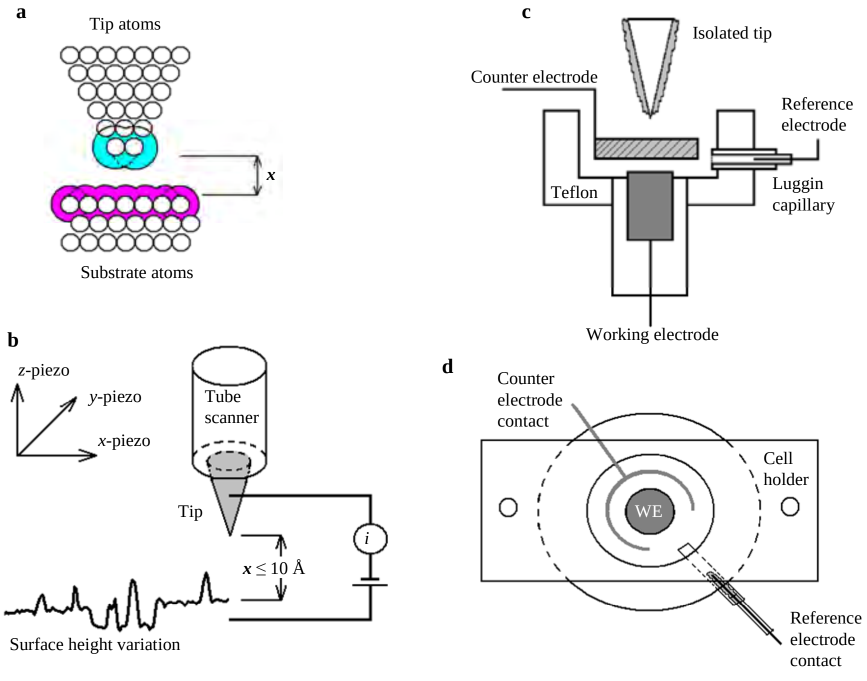

Figure 2. A schematic representation of the electron tunnelling phenomenon between the atoms of the STM tip and the sample (a). The movement of a STM tip over substrate during the scan (b). A schematic representation of the electrochemical cell used in the *in situ* STM measurements: a side view (c) and a view from above (d).

For the *in situ* STM measurements conducted in this work, a constant current mode is used like for the most experiments nowadays. In this mode, the tip in the *z*-direction is moved until tunnelling current flows, and simultaneously, the tip is scanned across the *x*-, and *y*-directions, *i.e.* across the surface of a substrate (Fig. 2b). At the same time the current is kept constant by moving the tip in the *z*-direction by electromechanically varying *x*. The movement of the tip is well controlled by the piezo elements. When a voltage is applied to piezo material, and if system is properly calibrated, its dimensions change precisely enough to maintain a stable operation in the scale of sub-nanometer (Fig. 2b). A detailed description of how the basic STM works has been given in literature [63], and nowadays even an electrochemical STM is widely considered as a standard method. Therefore, only a simplified summary of each method is given in this work.

2.5 *In situ* STM in modern electrochemistry

In the case of *in situ* STM, also known as dynamic or electrochemical STM, the working electrode (WE) is usually mounted at the bottom of the cell (Fig. 2c and 2d). Typical *in situ* STM cell consists of at least two more electrodes: a counter electrode (CE) and a reference electrode (RE). At every time interval, small enough, the scanning tip is held above the WE surface. The potentials of WE (E_{WE}) and the tip (E_{tip}) are then controlled independently with a bipotentiostat. To initiate and manipulate the electro(chemical) reaction(s) and the processes of adsorption–desorption or dissolution–deposition at the WE | substrate interface, a change in the potential of working electrode is usually chosen as a main driving force. Thereafter, to image the structural changes at the surface of a substrate during the changes of E_{WE}, the values of i_{tunnel} and E_{tip} are usually adjusted constantly, along with the image scan rate, v_{scan}, of course.

To be useful for imaging in a liquid medium, the STM tip is insulated with a non-conducting polymer, so that the effective area of the tip in contact with the electrolyte phase is minimal. However, its contact with the substrate relies on a small cluster of atoms, to provide better control over the electron tunnelling process. For the objects that undergo quick oxidation at the presence of dissolved oxygen even at the negative *E* (bismuth, antimony, cadmium, copper *etc.*), the setup for *in situ* STM measurements requires an environmental chamber. In the other cases, water traces in a non-aqueous solvent or in a RTIL can also be problematic as well as the tungsten STM tip can be oxidised or dissolved. During a few hours before the *in situ* STM measurements on a Bi(*hkl*) electrode started, an inert gas (N_2 or Ar) was used to deaerate the environmental chamber.

III EXPERIMENTAL

Molecular Imaging PicoSPM (model MS300) and Agilent Technologies (model 5500) systems were used for *in situ* STM and CV measurements.

STM tips were etched electrochemically from a tungsten wire and insulated with an Apiezon wax [3–8,40,62]. The STM tips and measurement system were calibrated using a freshly cleaved HOPG basal plane C(0001) (SPI).All STM images were recorded in a constant current mode with tunnelling currents varying from 0.1 nA to 3.0 nA.

A home-made hermetic cylindrical three-electrode electrochemical cell from tetrafluoropolyethylene (Teflon) with 0.6 cm^3 volume and a large-area Pt net counter electrode were treated before each experiment with a mixture of concentrated $H_2SO_4 + H_2O_2$ for 30 min at 100 ºC, thereafter rinsed repetitively with MilliQ$^+$ water and dried at 60 ºC [1,3,4,25,26,37].

$BMPyBF_4$ (Fluka Analytical, $H_2O < 100$ ppm), and $EMImBF_4$ (Fluka Analytical, purity ≥ 99.0 %, $H_2O < 100$ ppm) were used as electrolytes (Papers 2 and 3).

The mixed RTIL based electrolyte studied in Paper 3 was prepared (1 h before the measurements) from $EMImBF_4$ and EMImI (Merck KGaA, purity > 99.5 %, $H_2O < 300$ ppm). 1 wt% of EMImI was dissolved in the $EMImBF_4$ in dark conditions by heating the mixture up to 80° C in Ar medium and cooled slowly to 22 ± 1° C [8]. Thereafter, this mixture was additionally dried inside glove box at 60 ± 1° C applying the intensive mixing with dry Ar (purity > 99.9999 %) for 6 h.

An Ag | AgCl wire in the same $BMPyBF_4$ [25,26], $EMImBF_4$ [8,40] or in a mixture of $EMImBF_4$ + EMImI served as a quasi reference electrode [8,40,62]. All potentials are given *versus* the Ag | AgCl reference electrode in the same RTIL medium.

The Ag wire was cleaned in the 0.1 M HCl solution using the cathodic hydrogen evolution process, and thereafter the AgCl coating was deposited onto Ag wire from the fresh 0.1 M HCl solution. The anodic polarisation of about $E \sim 1.5$ V ($i \leq 0.1$ mA) was applied up to 30 s until the continuous white AgCl coating appeared on the Ag wire. Then the Ag | AgCl RE was flushed thoroughly with the MilliQ$^+$ water, dried in the Ar gas flow, immersed into the RTIL and left for the stabilisation overnight under the Ar atmosphere in dark conditions. The reference electrode was connected to the electrochemical cell through a Luggin capillary to avoid contamination of RTIL with Cl^- anions.

The Bi(111) cylinders with the diameter of 3.6 mm were made from the massive single crystal [1,3,4,25,26,36,37,40] grown by using a vertical Czochralsky method [1,40], and pressed into hot Teflon holders. A bottom of the cylinder (*i.e.* the Bi(111) plane) was served as a WE. At least three different electrodes with the same orientation (111) were measured for the statistical collection of the data.

After the cleavage or electrochemical polishing procedure [1,40,62], a mirror-like Bi(111) surface was immediately introduced into the electrochemical cell. Thereafter, the Ar saturated RTIL or RTIL mixture was added and the potential was instantly fixed at $E = -0.8$ V, or in some experiments at $E = -1.2$ V (*vs.* Ag | AgCl in the same RTIL). After a successful preparation procedure the Bi(111) surface is known to be very stable under the cathodic polarisation [1].

After 1 h to 6 h polarisation of the Bi(111) electrode at −0.8 V (*vs.* Ag | AgCl), the stable cathodic current densities (j) lower than -0.01 μA cm^{-2} and -0.6 μA cm^{-2} at the electrode potentials −0.4 V and −1.1 V were measured for $BMPyBF_4$ or $EMImBF_4$ system, respectively. For $EMImBF_4$ + EMImI mixture, the same current densities have been measured at $E = -0.4$ V and $E = -0.8$ V, respectively. All experiments were conducted at 22 ± 1° C.

The narrower region of ideal polarisability for Bi(111) compared to a glassy carbon electrode is mainly caused by higher oxidation ability of the Bi electrode at less negative potentials ($E \geq -0.2$ V), and by acceleration of the hydrogen evolution process ($j < -1.0$ μAcm^{-2}) at more negative potentials ($E \leq -1.2$ V). Electro reduction of the BF_4^- anions starts also at $E \leq -1.2$ V. Residual H_2O molecules participate in BF_4^- electro reduction process, where BF_3 and F^- are the probable intermediates [3,25,26,36,37].

Cathodic polarisation of a Bi(*hkl*) electrode under Ar atmosphere (surface inactive gas) is a prerequisite to maintain an atomically flat non-oxidised and time-stable Bi(111) surface. Hence, the concentrations of O_2 and H_2O in the electrolyte and in the gas phase must be kept as low as possible [3,25,26,37,53,54,74].

Several repetitive experiments were performed in this work to obtain the reproducible *in situ* STM data. All STM images were analysed using Gwyddion [75] and Nanotec Electronica WSXM$^{\text{TM}}$ [76] freeware.

Comparative CV and EIS measurements were performed inside the Mbraun Labmaster$^{\text{TM}}$ glove box using an Autolab PGSTAT 320 with a FRA II impedance analyser.

At least 6 independent measurements were made and the statistically treated series capacitance C_s *vs.* E-curves, were analysed. The parameters calculated from the impedance data using the non-linear least squares fitting method (the high-frequency series resistance, R_s, the mass transfer resistance, R_d, the charge transfer resistance, R_{ct}, the high-frequency capacitance, C_{dl}, and the low-frequency adsorption capacitance, C_{ad}) have been statistically treated after fitting the calculated impedance spectra to the experimental ones [3,16–18,25,26,36,37,53,54,77].

Agreement of the data measured using the *in situ* STM method with the results published by Siinor *et al.* [25,26], obtained inside the MBraun Labmaster glove box (extremely low residual O_2 and H_2O concentrations), was reasonable. Hence, due to the somewhat higher O_2 partial pressure and the residual H_2O in the gas phase in the *in situ* STM electrochemical cell, the cathodic current densities were slightly higher for the *in situ* STM experiments at $E < -1.0$ V.

IV RESULTS AND DISCUSSION

4.1 Analysis of cyclic voltammetry data

To set up frameworks of reproducible current-potential dependencies and to preserve an atomic flatness of a Bi(111) surface for further *in situ* STM or EIS measurements, firstly the CV data were measured. The CV data were obtained within controlled potential regions (*vs.* Ag | AgCl in the same RTIL): $-1.2\text{ V} < E \leq -0.3\text{ V}$ for Bi(111) | $BMPyBF_4$ interface, $-1.2\text{ V} < E \leq 0.0\text{ V}$ for Bi(111) | $EMImBF_4$ interface, and $-0.8\text{ V} < E \leq -0.2\text{ V}$ for Bi(111) | $EMImBF_4$ + EMImI interface, respectively (Fig. 3a, 3b and 3c).

Based on CV data, the Bi(111) | $EMImBF_4$ interface exhibits the widest area of ideal polarisability ($-1.2\text{ V} < E \leq 0.0\text{ V}$). If 1wt% EMImI is mixed with the $EMImBF_4$, the region of ideal polarisability decreases by ~0.4 V (being within the region of $-1.0\text{ V} < E \leq -0.2\text{ V}$). The EDL charging currents initiated from specifically adsorbed species (the I^- ions) cause the increase in the current density at Bi(111) working electrode at $E > -0.4\text{ V}$ (Fig. 3b). For the Bi(111) | $BMPyBF_4$ interface (Fig. 3c), the region of ideal polarisability is somewhat narrower ($-1.2\text{ V} < E \leq -0.3\text{ V}$) than that for the Bi(111) | $EMImBF_4$ interface (Fig. 3a). In general, the regions of ideal polarisability for systems studied in this work are in a good agreement with the data for Bi(111) | Na_2SO_4 + H_2SO_4 interface in aqueous solutions [3–7,25,26,37,78].

Anodic limit of the Bi(111) | RTIL systems is determined by the irreversible oxidation process of Bi(111) surface (where the current density increases exponentially), which occurs at $E \sim -0.1\text{ V}$. A decomposition process of residual water already starts slowly at $E \leq -1.0\text{ V}$, where the cathodic currents increase exponentially (Fig. 3a, 3b and 3c). Thus, mainly slow adsorption and desorption processes of RTIL ions have been established within the mentioned E regions [78]. According to the literature data [79,80], a reduction of $EMIm^+$ cation and its dimer formation both occur only at $E < -2.0\text{ V}$, *i.e.* outside of the potential region studied in this work, where the formed thick dimer (polymer) layer blocks the electrode surface. At $E < -2.0\text{ V}$, further STM probing and / or E cycling is not possible. Other faradic reduction reactions, including the electro reduction (decomposition) of BF_4^- anions, also can occur outside the ideally polarisable E regions applied in this work.

The mixture of $EMImBF_4$ + EMImI is stable between $E = -1.2\text{ V}$ and $E = -0.2\text{ V}$, mainly due to the strong blocking adsorption of iodide ions (from $E = -0.8\text{ V}$ to $E = -0.3\text{ V}$, demonstrated in a detail in chapters VI.4.4.2.3 and VI.4.4.3.2). In general, CVs can be measured at slightly more positive potentials, while the STM or EIS measurements are carried out within the range of potentials demonstrated in Fig. 3.

The $BMPy^+$ cations in $BMPyBF_4$ are also known to be stable from $E = -1.2\text{ V}$ to $E = -0.3\text{ V}$, but the electrochemical stability for this RTIL is somewhat lower compared to $EMIm^+$ cations in $EMImBF_4$, according to data discussed in Refs. [64,78]. In general, if the reduction reaction is involved, the

$BMPyBF_4$ has been proposed to undergo the radical coupling and dimeriation processes, which often results in further chemical reaction(s) and unpredictable electroactive species [78].

4.2 Analysis of electrochemical impedance data

Impedance measurements were conducted for the simultaneous analysis of the adsorption kinetics of the ions. Thus, the complex impedance *Z*, and phase angle *Φ* *vs.* log *f* plots and *Z*'', *Z*' (Nyquist plots) were measured, where *Z*′ and *Z*″ are the real and imaginary parts of the impedance, *Z*, respectively. From the Eq. (13), an Eq. (19) is obtained:

$$Z'' = \frac{-1}{\omega C_s} \tag{19}$$

The series capacitance, C_s, can be calculated at several fixed frequencies, shown in the Fig. 3 [25,26,37].

Based on the analysis of the *i*,*E*-dependencies and corresponding STM data for Au(*hkl*) [14,34,42,81–88], the potential-induced surface reconstruction processes due to the mobility of the Au surface atoms were well established at Au(*hkl*) | electrolyte solution interfaces (aqueous or ionic liquid medium). However, in the present work like in previous studies [1–3,5–7,9,10,12,15,27,28], no Bi(111) surface reconstruction peaks were obtained neither in *i*, *E*-curves (Fig. 3a, 3b and 3c) nor in C_s, *E*-curves (Fig. 3d, 3e and 3f). Therefore, similarly to Bi(111) | $Na_2SO_4 + H_2SO_4$ aqueous electrolyte solution interface [1,3,4,46], no evidences of surface reconstruction effect has been observed based on CV, impedance and also *in situ* STM data (discussed later) for Bi(111) | $EMImBF_4$, Bi(111) | $BMPyBF_4$ or Bi(111) | $EMImBF_4$ + EMImI interfaces.

Data in Fig. 3d show that for Bi(111) | $EMImBF_4$ interface, there is only a slight dependency of series capacitance, C_s on *E*, when *f* varies from 10 Hz to 1000 Hz. For Bi(111) | $BMPyBF_4$ interface there is practically no dependency of C_s on *E*, when *f* varies from 30 Hz to 1000 Hz (Fig. 3f). The biggest growth of the capacitance in both cases takes place at the frequencies $f \leq 20$ Hz, indicating the very slow adsorption process of the ions on the Bi(111) | RTIL interface [14,37,40,84] (Fig. 3d and 3f). Data in Fig. 3e show that from the $EMImBF_4$ + EMImI mixture, the adsorption of I^- anions onto the Bi(111) surface clearly occurs at $f \leq 215$ Hz, if $E \geq -0.6$ V. It should be noted that the surface activity of the organic compounds increases with growth of the metal hydrophobic properties [1,49]. Based on the simple Helmholtz EDL model (as in Eq. (20)):

$$C_s = \frac{\varepsilon\varepsilon_0}{d}, \tag{20}$$

where ε_0 is a dielectric constant of vacuum, ε is the relative dielectric constant of the EDL and *d* is the effective thickness of the EDL region [1,46,49,55], with the increase in the length of the RTIL hydrocarbon chain, the dielectric permittivity (ε) of the EDL decreases and the values of C_s decrease (Fig. 3d).

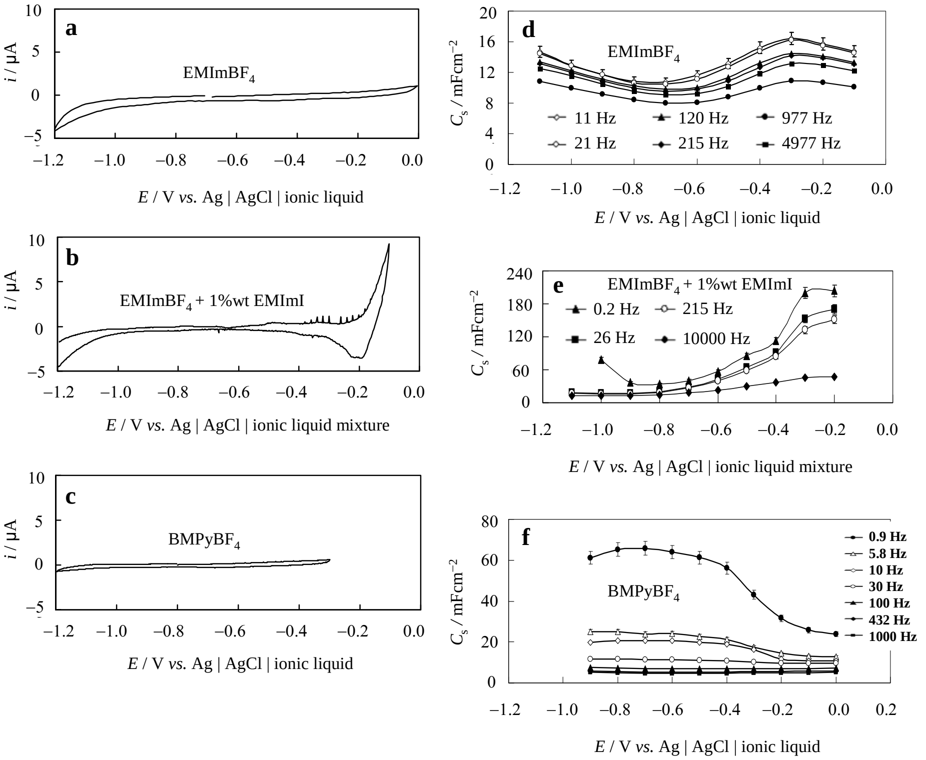

Figure 3. Experimental CV data for a Bi(111) electrode in $EMImBF_4$ (a), $EMImBF_4$ + 1wt% EMImI mixture (b) and $BMPyBF_4$ (c) (CV scanning rate: dE / dt = 10 mV/s), and C_s, E-plots calculated from EIS measurements at different fixed frequencies for Bi(111) electrode in $EMImBF_4$ (d), $EMImBF_4$ + 1wt% EMImI mixture (e) and $BMPyBF_4$ (f). All potentials are given *vs.* Ag | AgCl reference electrode in the same ionic liquid at 22±1°C.

Data in Fig. 3f show that the slow adsorption of $BMPy^+$ cations takes place and the values of C_s increase with the decrease of ac frequency.

Analysis of the electrochemical impedance data based on non-linear square root fitting method has been conducted. It was found that the more adequate fit of calculated spectra with the experimental ones (Fig. 4b) can be obtained by using the modified Frumkin − Melik-Gaikazyan equivalent circuit (Fig. 4b inset) [25,26,37,89,90]. It was established that the finite-length Warburg element (W_1, Warburg diffusion-like impedance) for short circuit conditions at $f \rightarrow 0$ should be used in the EC to have a good fitting. Thereafter, the values of

C_{dl}, C_{ad}, and diffusion resistance (R_D) were calculated (Fig. 4a and 4c) considering the equivalent circuit modelling method [89,90]. R_{el} is the very high-frequency series resistance (mainly equal to the electrolyte series resistance).

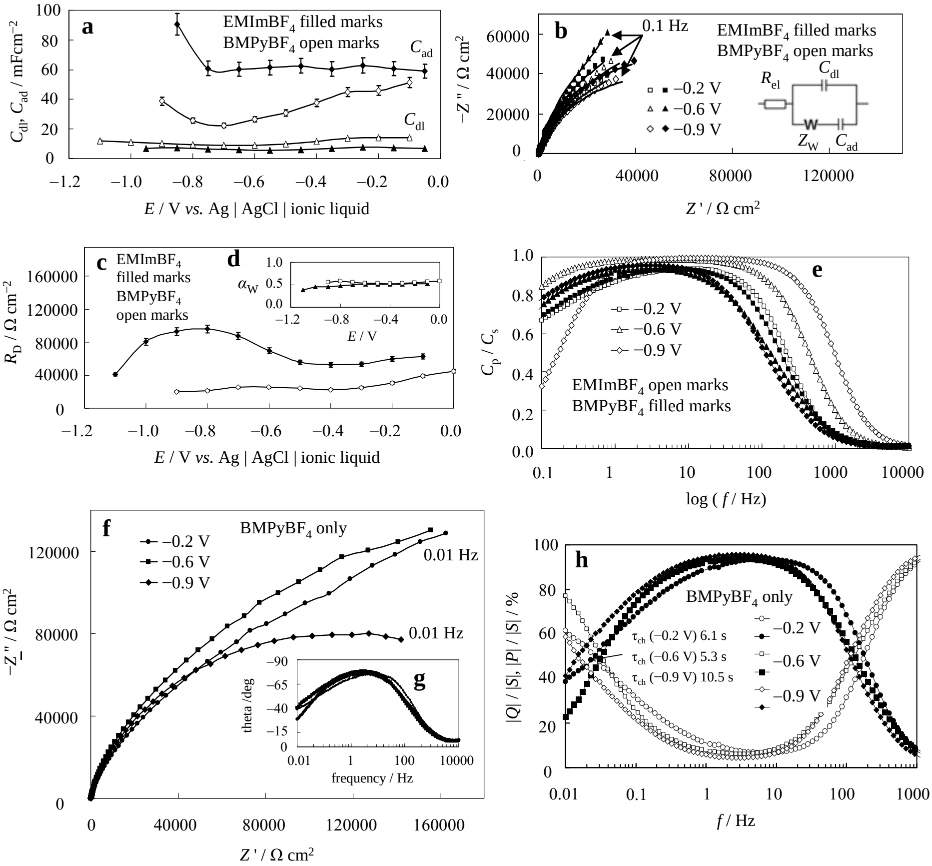

Figure 4. Adsorption capacitance, C_{ad}, E and electrical double layer capacitance C_{dl}, E plots calculated from EIS measurements (a) for a Bi(111) electrode in $EMImBF_4$ and $BMPyBF_4$ (noted in the Figure); impedance complex plane (Z'',Z) plots (b) (dots – exp. data, lines – fitting by modified Frumkin –Melik-Gaikazyan equivalent circuit, at potentials marked in the Figure). Dependencies of C_{dl}, C_{ad} (c) and diffusion resistance R_D (d) on the electrode potential for Bi(111) in $BMPyBF_4$ (open marks) and $EMImBF_4$ (filled marks). Insets in (d): modified Frumkin – Melik-Gaikazyan circuit. Inset in (c): fractional exponent of the Warburg-like diffusion impedance *vs.* electrode potential curves. Dependence of the ratio of parallel capacitance to the series capacitance, C_p/C_s, on log f (e) at different potentials (given in the Figures) for the Bi(111) | $EMImBF_4$ (open marks) and Bi(111) | $BMPyBF_4$ (filled marks) interfaces. Experimental Nyquist (f) and Bode phase angle (inset) plots at fixed E (g) and the normalised real part |P|/|S| and imaginary part |Q|/|S| of the complex power vs. ac frequency plots (h) for Bi(111) electrode in $BMPyBF_4$.

As demonstrated in Fig. 4a, the values of capacitance, C_s, can be divided into 2 components [25,26,37,89–92]. C_{dl} is the fitted (so-called ‘‘true’’) electrical double layer differential capacitance (high-frequency parameter, obtained at $\omega \rightarrow \infty$), and C_{ad} is the adsorption capacitance (low-frequency limiting differential capacitance established at $\omega \rightarrow 0$). According to the theoretical models and results of fitting data [1,46], C_{dl} contains also the thin film capacitance for Bi(111) surface layer, being somewhat higher for a Bi(111) | $EMImBF_4$ interface (Fig. 4a) than that for a Bi(111) | $BMPyBF_4$ interface.

To the first very rough approximation a zero charge potential, $E_{\sigma=0}$, can be estimated from the capacitance data at low / medium frequency region ($f \geq 10$ Hz) for a Bi(111) | RTIL interface (Fig. 4a). Taking into account that the C_{dl} minimum usually for semi metallic Bi(111) corresponds to the $E_{\sigma=0}$ value [1]. Surface charge density (σ) is defined as the charge per surface area (C / cm^{-2}). The σ values can further be correlated with the theoretical modelling results and calculations data. The values of C_{dl} and C_{ad} for Bi(111) | $EMImBF_4$ interface are minimal at $E = -0.7$ V (Fig. 4a), pointing to the zero charge potential $E_{\sigma=0}$ [1,4,25,26] location for this interface.

In the case of Bi(111) | $BMPyBF_4$ or Bi(111) | $EMImBF_4$ interfaces, $E_{\sigma=0}$ corresponds to the so-called true zero charge potential as there is no specific adsorption of the ions (or hydrogen, oxygen, *etc.*) on the Bi(111) surface [4,46]. As a result, there is no shift of the $E_{\sigma=0}$ values (Fig. 3d) due to the adsorption of the RTIL ($EMImBF_4$) components [4,25,26,46]. A small shift of $E_{\sigma=0}$ at $f \leq 0.9$ Hz toward more negative E values can be explained by the partial charge transfer process between the Bi(111) surface and adsorbed BF_4^- anions [1,25,26,37,49,93,94] for Bi(111) | $BMPyBF_4$ interface (Fig. 3f).

Based on the data in Fig. 3e, there is a noticeable increase in the values of C_s at $E \geq -0.3$ V for $EMImBF_4$ + EMImI RTIL mixed system, indicating that I^- anions are surface active on Bi(111). This conclusion is based on a fact that typically for specific adsorption of anions, in the region $E \geq -0.7$ V, there is strong dependence of C_s on $\log f$, established for aqueous and non-aqueous NaF + NaI; KF + KI or $LiClO_4$ + LiI binary electrolyte solutions with constant ionic strength [25,26,36,37].

For both, Bi(111) | $EMImBF_4$ and Bi(111) | $BMPyBF_4$ interfaces again, at $E < -0.7$ V σ has the negative values (the physical adsorption of cations is dominating in the first layers), and at $E > -0.7$ V, σ has positive values (mostly the adsorption of anions dominates) (Fig. 3d, 3f and 4a).

At more negative potentials ($E < -0.8$ V) specific adsorption with the partial charge transfer and faradic processes are possible for both interfaces (Fig. 4a). Based on literature data $EMImBF_4$ has a greater electrochemical stability than $BMPyBF_4$ [78], hence the Bi(111) | $EMImBF_4$ interface is somewhat more stable than Bi(111) | $BMPyBF_4$ interface at $E < E_{\sigma=0}$.

Within the region of more positive potentials, $-0.3\text{ V} < E < 0.0$ V, the electrostatic physical adsorption of the BF_4^- anions is followed by the partial charge transfer process [91,92], sometimes known as a weak specific adsorption. However, in the same E region, the dissolution and irreversible oxidation of bismuth (see the impedance data below in this chapter and the STM data in chapters VI.4.4.2.1 and VI.4.4.2.2) started, and therefore, this region of E has not been studied systematically.

The slope of the Nyquist plots depends on E applied for the Bi(111) | EMImBF$_4$ and Bi(111) | BMPyBF$_4$ interfaces (Fig. 4b). Deviation of the Bi(111) | BMPyBF$_4$ interface from the adsorption step limited system is the highest at $E = -0.6$ V (near the zero charge potential), where there is no preferable adsorption of the BMPy$^+$ cations or the BF$_4^-$ anions (or the BMPy$^+$ BF$_4^-$ ion pairs) into the first ionic layer. The Bi(111) | EMImBF$_4$ interface deviates from the adsorption step limitation at $E = -1.2$ V and at $E = -0.4$ V, where cations and anions form the first layer, respectively.

In general, C_{dl} does not depend noticeably on the potential applied neither for Bi(111) | EMImBF$_4$ nor Bi(111) | BMPyBF$_4$ interface, which agrees with the Frumkin − Melik-Gaikazyan model [89,91,92,95,96] (Fig. 4a). In contrast, the values of C_{ad} quickly increase within the region of E from −0.7 V to −1.0 V, where the adsorption of the EMIm$^+$ or BMPy$^+$ cations into the first layer starts (Fig. 4a). Nevertheless, the rise of the C_{ad} values within the potential region from −0.7 V to −0.3 V indicates the adsorption of BF$_4^-$ anion. The noticeable difference in the values of C_{s}, C_{dl} and C_{ad} indicates that formation of the adsorption layer is a very slow process [89–92,95,96] (Figs. 3 and 4a). Thus, the noticeable increase in the C_{s} values at lower frequencies is mainly caused by the adsorption process (*i.e.* by the increase in C_{ad} for the Bi(111) electrode in a RTIL) (Fig. 4a).

The values R_{D} (results of fitting analysis) (at $f \to 0$) at fixed E are also higher for Bi(111) | EMImBF$_4$ interface than those for Bi(111) | BMPyBF$_4$ interface (Fig. 4c). The higher values of R_{D} show that the mass transfer energy (resistance) is higher for the RTIL with the smaller molar volume characterised by the lower compactness of organic cation based adsorption layer due to the higher thickness and dielectric constant (ε) values for the Bi(111) | EMImBF$_4$ interface compared with Bi(111) | BMPyBF$_4$ interface.

The values of fractional exponent for the Warburg-like diffusion impedance [25,26,37,89,90], α_{W}, are equal or greater than 0.55 for both systems (inset in Fig. 4d). For a Bi(111) | BMPyBF$_4$ interface the values of α_{W} are slightly higher compared to the Bi(111) | EMImBF$_4$ interface. Therefore, the finite-length Warburg element for short circuit conditions at $f \to 0$ can be applied for fitting of calculated data to the experimental impedance spectra.

4.3 Fitting and analysis of Nyquist plots data

The big increase in C_{s} and in the parallel capacitance, C_{p}, calculated from Eq. (21) [37,60,97–102] similarly to C_{s}, takes place only at the very low frequencies (Fig. 4e) ($f \leq 10$ Hz), which could be explained by the slower adsorption layer formation for both RTIL based systems [37,91,92,95].

$$C_p = C_s(1+\tan^2\left(\frac{Z'(\omega)}{Z''(\omega)}\right)) \tag{21}$$

At $\sigma > 0$, the charge of the first adsorbed ionic layer is partially compensated by the second (anions) layer charge and by the following ionic layers [27,28]. Similarly to the adsorption of the organic compounds at the Bi(111) surface [37,98], the very low values of C_{dl} (from 5 μFcm^2 to 6 μFcm^2 at $E \leq -0.7$ V), calculated from the impedance data (Fig. 4a), indicate the very low values of dielectric constant for the Bi(111) | EMImBF$_4$ and Bi(111) | BMPyBF$_4$ interfaces under study [25,26,37].

The values of parallel capacitance were calculated using classical calculation method [1,5,6,46,89,90], and based on the Eq.-s (22) and (23):

$$C_p = \frac{C_s}{1+\tan^2\delta}, \tag{22}$$

$$\text{where } \delta = \arctan\left(\frac{Z'}{Z''}\right) \tag{23}$$

The ratio C_p / C_s (Fig. 4e) in general depends strongly on f, but only slightly on E applied. If $C_p / C_s = 1.0$, the processes at an interface have capacitive behaviour; if $C_p / C_s = 0.5$, the processes are diffusion step limited; and if $C_p / C_s = 0.0$, the faradic processes are determinative for a Bi(111) | RTIL interface [91,92,95].

More detailed analysis of the impedance data (Fig. 4e) shows that the slow adsorption and mass-transfer (diffusion-like) steps are the limiting stages for both RTIL adsorption at the Bi(111) surface: EMIm$^+$ at $E \leq -0.9$ V, BMPy$^+$ at $E \leq -0.7$ V and BF$_4^-$ at $E = -0.2$ V, as the ratio C_p / C_s is lower than unity at $f < 1$ Hz [37,53,54,91,92,95,103]. Similarly to the C_s growth at the very low frequencies (Fig. 3d, 3e and 3f), the formation of the stable adsorption layer structure during from minutes to 1 . . . 2 h after changing E from low negative values (−0.6 V) towards more negative values (to −0.8 V or to −1.0 V) indicates that the adsorption of the RTILs under study on the Bi(111) electrodes is indeed a very slow process, which is established also by the *in situ* STM method (discussed in the chapter VI.4.4.2.).

The EDL formation kinetics and mechanism depend weakly on E applied for Bi(111) | EMImBF$_4$ and for Bi(111) | BMPyBF$_4$ interfaces. Based on the impedance data (Fig. 5), the nearly ideal capacitive behaviour can be seen from the slope values for the log |Z''|, log f plots varying from −1.0 to −0.9 within whole potential and frequency range. At $E = -0.2$ V, the processes of surface oxidation and dissolution start. For Bi(111) | BMPyBF$_4$ interface, a more pronounced deviation of the system from the adsorption step limited mechanism has been observed (the slopes of the log |Z''|, log f-plots nearly −0.6).

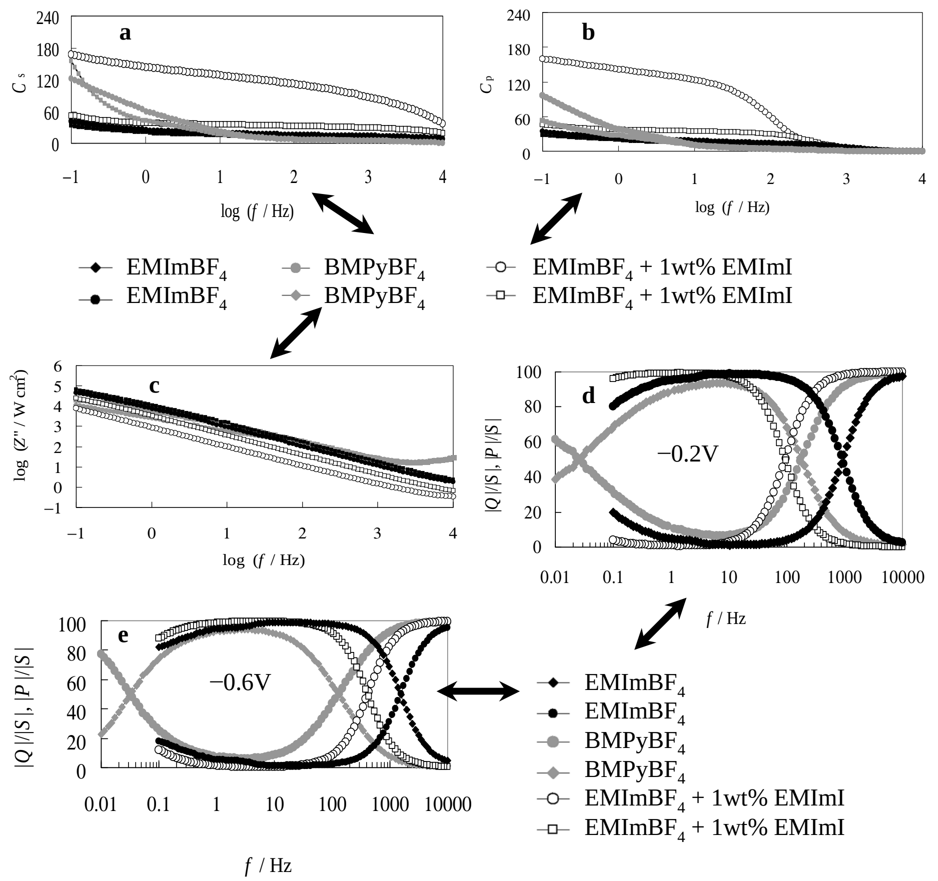

Figure 5. The dependencies of series capacitance (C_s) on log frequency (log *f*) (a), parallel capacitance (C_p) on log *f* (b), log impedance imaginary part (log *Z*'') on log *f* (c), and the normalised real part |*P*| / |*S*| and imaginary part |*Q*| / |*S*| of the complex power vs. ac frequency plots (d) and (e) at different negative potentials given in the Figure.

The same information and conclusions for Bi(111) | BMPyBF$_4$ interface follow from the analysis of the Bode phase angle (θ) *vs.* log *f* -plots (inset in Fig. 4g) [24,25,53,54,89,90,95,96]. The values of phase angle, $\theta \approx -45°$, indicate the very slow mass-transfer (diffusion-like) limited step at $E = -0.2$ V. The values of θ lower than −52° (down to −70°) at $E = -0.9$ V point to the mixed kinetic process(es).

For the more detailed kinetic analysis of a Bi(111) | RTIL interface, the characteristic relaxation frequencies can be used. The values of the characteristic relaxation time constant (τ_{ch}) for a Bi(111) | BMPyBF$_4$ interface have been calculated from the intersection point of the dependencies of normalised real part |*P*| / |*S*| (25) and imaginary part |*Q*| / |*S*| (26) of the complex power (25) on frequency [15–19] (Fig. 4h). The following Eq.-s were used:

$$\tau_{ch} = \frac{1}{2\pi f_{\max}} \tag{24}$$

$$S(\omega) = P(\omega) + jQ(\omega) \tag{25}$$

$$P(\omega) = \omega C''(\omega) \,|\, \Delta U_{rms} \,|^2 \tag{26}$$

$$Q(\omega) = -\omega C'(\omega) \,|\, \Delta U_{rms} \,|^2 \tag{27}$$

$$|\, \Delta U_{rms} \,|^2 = \frac{\Delta U_{\max}}{\sqrt{2}}, \tag{28}$$

where $f_{\max}$ is the maximal frequency and $U_{\max}$ is the maximal amplitude of ac voltage. The shortest characteristic adsorption relaxation time ($\tau_{\mathrm{ch}} = 5$ s) has been calculated at $E = -0.6$ V. At $E = -0.9$ V, the value of τ_{ch} is even longer than 10 s indicating that the reorganisation of $\mathrm{BMPyBF_4}^+$ cations is a very slow process. At positively charged Bi(111) surface the adsorption layer formation, *i.e.*, the orientation of $\mathrm{BF_4}^-$ anions is quicker because $\tau_{\mathrm{ch}} = 6.1$ s, thus, only somewhat slower than that at $E = -0.6$ V. Relaxation time constants for the electrical double layer formation $\tau_{\mathrm{ch}} \geq 10$ s are characteristic of the microporous mesoporous carbon electrodes in the non-aqueous and RTIL + NAS electrolyte solutions [15–21]. Consequently, the τ_{ch} values depend noticeably on *E*, *i.e.*, on the chemical composition and on the structure of cations and anions adsorbed at Bi(111) surface. These data are in a good agreement with the shape of the C_{s}, E -plots and C_{ad}, E -plots (Figs. 3b, 3d, 3f and 4a) measured at different frequencies, and the $C_{\mathrm{p}} / C_{\mathrm{s}}$ *vs.* $\log f$ -plots (Fig. 4f), discussed before. Thus, surprisingly, the very long adsorption times are required for the establishment of the superstructure formation equilibrium at the Bi(111) electrode | $\mathrm{BMPyBF_4}$ interface. This result differs totally from the results for the 2,2-bipyridine and camphor adsorption kinetics at the Bi(111) surface from the aqueous $\mathrm{Na_2SO_4}$ solution, where the adsorption equilibrium has been established already at $\tau_{\mathrm{ch}} \leq 10^{-2}$ s [3].

The desorption, *i.e.* the dissolution of the $\mathrm{BMPyBF_4}$ superstructure is also a very slow process as after the potential step from −1.2 V to −0.8 V, or from −1.0 V to −0.6 V, more than 20 min was required to observe the *in situ* STM atomic resolution images (discussed later in this section). Both, the dissolution and the desorption processes of the $\mathrm{BMPyBF_4}$ complex are limited by the finite-length diffusion-like mass-transfer rate [25,26,37,74]. This effect and very long τ_{ch} can be explained by higher viscosity, lower dielectric permeability ($\varepsilon = 10 \ldots 12$), and stronger van der Waals interactions between the adsorbed BMPy^+ cations as compared to camphor or 2,2-bipyridine adsorbed from the aqueous electrolyte solutions (for example from $5 \cdot 10^{-2}$ M $\mathrm{Na_2SO_4}$ + $5 \cdot 10^{-4}$ M $\mathrm{H_2SO_4}$ solution) [3,53,54].

4.4 Analysis of the in situ STM data

4.4.1 Stability of the Bi(111) | RTIL interface and its main characteristics under cathodic polarisation

Interfacial structure of the cleaved Bi(111) surface in $EMImBF_4$, $BMPyBF_4$ and $EMImBF_4$ + 1wt% EMImI mixture under various cathodic polarisation at room temperature is given in Fig. 6 being in a good agreement with impedance data, discussed earlier in chapters VI.2 and VI.3. Bi(111) | $EMImBF_4$ interface is ideally polarisable within potential region from −1.2 V to −0.2 V, and Bi(111) | $BMPyBF_4$ interface from −1.1 V to −0.4 V (*vs.* Ag | AgCl in the same RTIL). For the Bi(111) | $EMImBF_4$ + 1wt% EMImI interface, the so-called “clean” surface conditions characteristic of Bi(111) | $Na_2SO_4 + H_2O$ interface were obtained only at $E \leq -1.0$ V. At $E > -1.0$ V, due to the iodide adsorption process occurring at $-0.8 \text{ V} \leq E \leq -0.3$ V, specific adsorption formations of I^- anions were found from the Bi(111) | $EMImBF_4$ + EMImI interface (discussed in a detail in chapters VI.4.4.2.3 and VI.4.4.3.2).

For variously prepared Bi(111) | $EMImBF_4$ and Bi(111) | $BMPyBF_4$ interfaces at different conditions, the triangular islands and hollow structures with single- or few-atomic layers in height at the Bi(111) surface have been demonstrated (Figs. 6 and 7). Terraces of a mono- or few-atomic height can be clearly distinguished along with many smaller triangular surface structures (Figs. 6 and 7), characteristic of a clean Bi(111) surface in various electrolytes [3–7,40,62]. These nanostructures at Bi(111) surface are probably created during the cleaving or electrochemical polishing procedure due to the screw dislocation or planar defects throughout the crystal. Typical sharp-edged structures for a clean Bi(111) surface with the height of few-atomic steps are demonstrated also in the surface height profile (Fig. 6d, 6e and 6f). Rare bigger triangular structures were found in most experiments [3–7,40,62]. Main crystallographic areas had an (111) orientation as expected, but at some steps (*i.e.* plane boundaries) and at the edges of terraces, the structures seem to go along [110], [101] and [011] crystallographic directions [104,105]. In addition, some structures with curved boundaries have been observed. An example represented in the right lower corner in Fig. 6a (brown half circle) is probably caused by the surface screw dislocation defects.

Electrochemically polished Bi(111) surface in the same RTIL mediums has comparable surface characteristics (Fig. 7) and the potential stability region is also comparable to that established for its cleaved analogue. For a pure Bi(111) | RTIL interface, atomically flat terraces can be observed even after many hours of potential cycling within $-1.2 \text{ V} \leq E \leq -0.6$ V, and / or when holding the system at fixed E like −1.0 V; −1.2 V *etc.* (Figs. 7–12).

Based on the data collected for Bi(111) electrode in aqueous solutions, electrochemical polishing and low temperature cutting surface preparation techniques have already been proved as valuable tools [1,2,5–8,14,16].

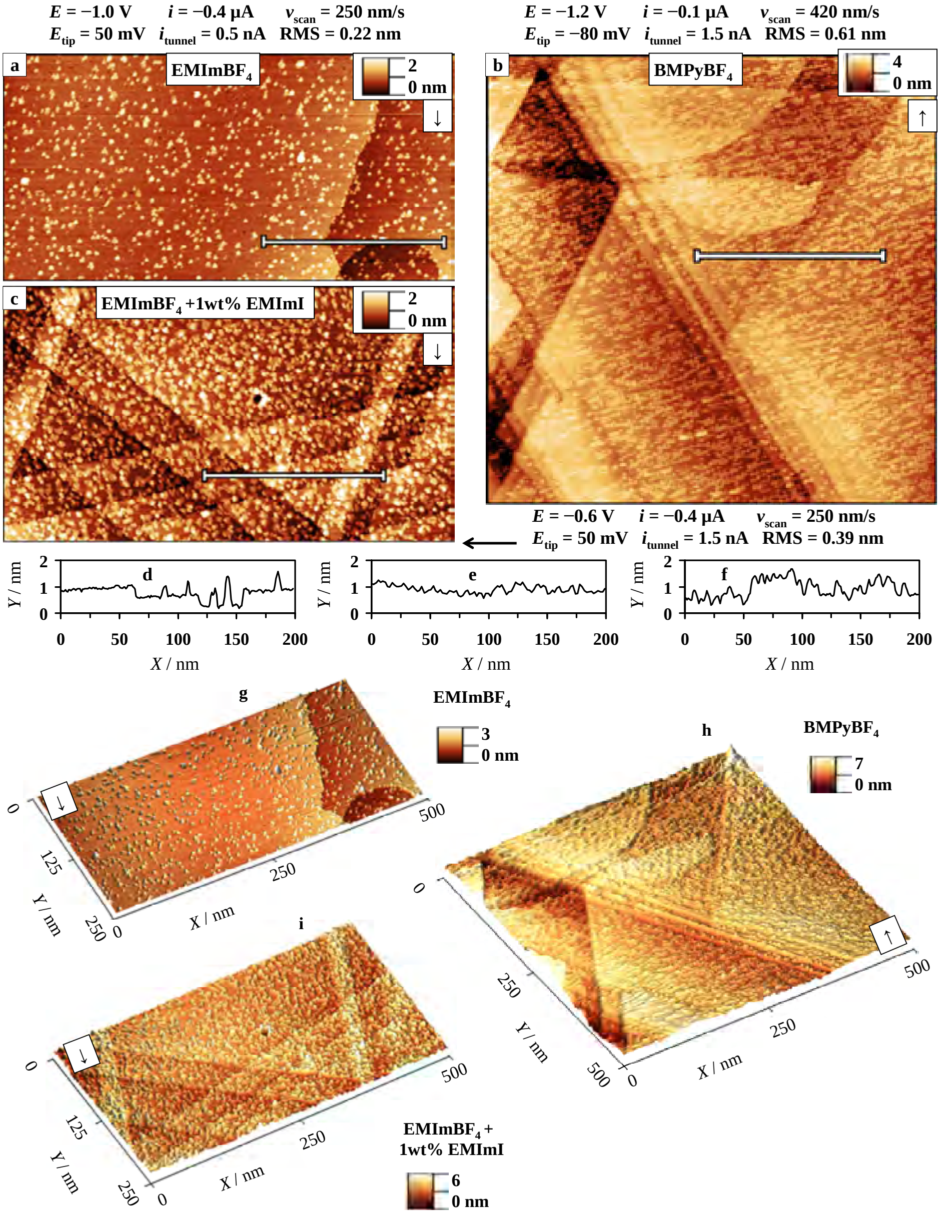

Figure 6. Cleaved Bi(111) electrode at negative electrode potentials (noted in Figure) in $EMImBF_4$ (a), $BMPyBF_4$ (b) and $EMImBF_4$ + 1wt% EMImI mixture (c), and the corresponding surface height profiles (d), (e) and (f). Image scan direction is marked with an arrow on each *in situ* STM image along with other scanning parameters, and the surface height profiles. Image size: 500 x 250 nm^2 for (a) and (c), and 500 x 500 nm^2 for (b). For each interface, corresponding 3D image of the same Bi(111) surface area is demonstrated in (g), (h) and (i), respectively.

However, in the case of RTILs the values of RMS roughness increases if the more extreme positive ($E \geq 0.0$ V) or negative ($E \leq -1.4$ V) potentials were applied. Systematic analysis of the data measured during many experiments for Bi(111) electrode in the $H_2O + Na_2SO_4$ solution shows that the values of RMS roughness [50] are independent of E applied within the region from −1.4 V to −0.5 V (*vs.* Ag | AgCl in sat. KCl aqueous solution) [3,4,46]. Therefore, we can conclude that both preparation methods yield atomically flat surfaces for Bi(111) electrode in the RTILs as well [40,62].

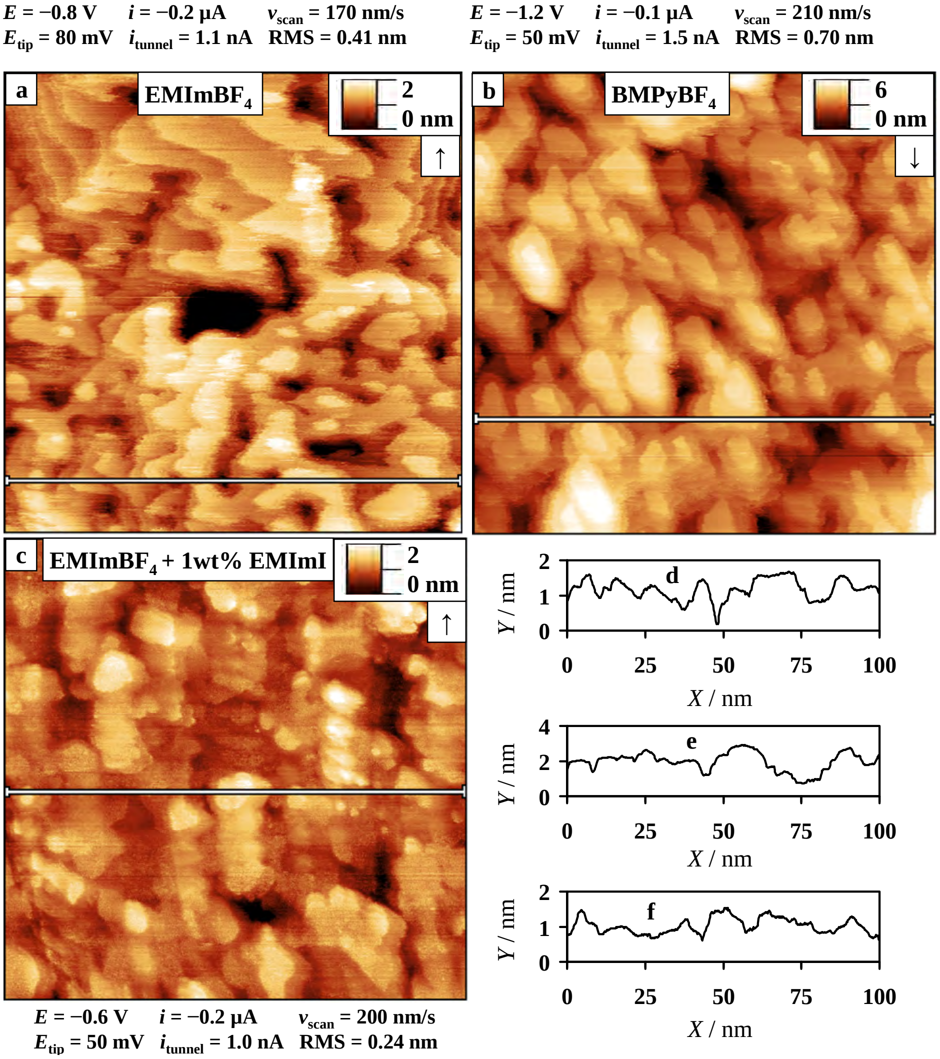

Figure 7. Electrochemically polished Bi(111) electrode structure at negative electrode potentials (noted in Figure) in $EMImBF_4$ (a), $BMPyBF_4$ (b) and $EMImBF_4$ + 1wt% EMImI mixture (c), and the corresponding surface height profiles (d), (e) and (f). Image size: 100 x 100 nm^2.

There is a major difference in the behaviour of the semi metallic Bi(111) in the aqueous solution or RTIL medium compared to the noble metals, for example, to the Au(*hkl*) electrode in the same electrolytes. Due to the high surface diffusion (mobility of the atoms at an Au surface), the reconstruction of Au(111) surface as a result of electrochemical polarisation is repeatedly possible. Therefore, the well known herring bone structure can be obtained for atomically flat Au(111) electrode [106], which is not a case for the Bi(111) surface [3,4,14,46,50,83]).

In the case of Bi(111) | RTIL systems, the triangular structures exposed at the cleaved or electrochemically polished surface are indeed very stable. Based on *in situ* STM experiments in this work, the surface reconstruction processes do not occur even at the otherwise active main crystal defect areas under the conditions of electrode potential cycling the potential from −1.2 V to −0.2 V. However, it is also demonstrated that at the extreme anodic potentials, the oxidation, dissolution and etching processes are irreversible at the Bi(111) | RTIL interface [4,14,46,50,83] like in aqueous solutions, and measurements at $E \geq -0.2$ V should be avoided, if the goal is to maintain an atomically flat electrode surface. In other words, to sustain a possibility for further studies of adsorption processes at the Bi(111) surface, processes at these less negative potentials have not been studied systematically in this work ($E \geq -0.4$ V for BMPyBF$_4$, $E \geq 0.0$ V for EMImBF$_4$, $E \geq -0.2$ V for EMImBF$_4$ + 1wt% EMImI mixture).

4.4.2 The Bi(111) | RTIL interface under the changing conditions of electrochemical polarisation

4.4.2.1 Bi(111) | EMImBF4 interface

For the Bi(111) | EMImBF$_4$ interface, a STM image at const. $E = -0.8$ V is demonstrated in Fig. 6a. The image was obtained after the first potential cycle ($-1.2\text{ V} < E \leq -0.4$ V applying within 0.2 V steps moderation, and total polarisation time, t_{pol}, was 6 h). It was found that the surface structure in this RTIL was the same after this potential cycle as at the beginning of the *in situ* STM experiments. A very low value of RMS roughness has been calculated for a Bi(111) surface (RMS = 0.22 nm) (Fig. 6a). The corresponding surface height profiles measured, and the RMS roughness values calculated were nearly independent of E applied during the first potential cycle (Figs. 8 and 9). A formation of the small white dots with curved profiles at the end of some surface steps (defect structures) could be explained by very slow electrodeposition (redeposition) of the bismuth nanoclusters onto the Bi(111) surface at ~$E \leq -1.0$ V.

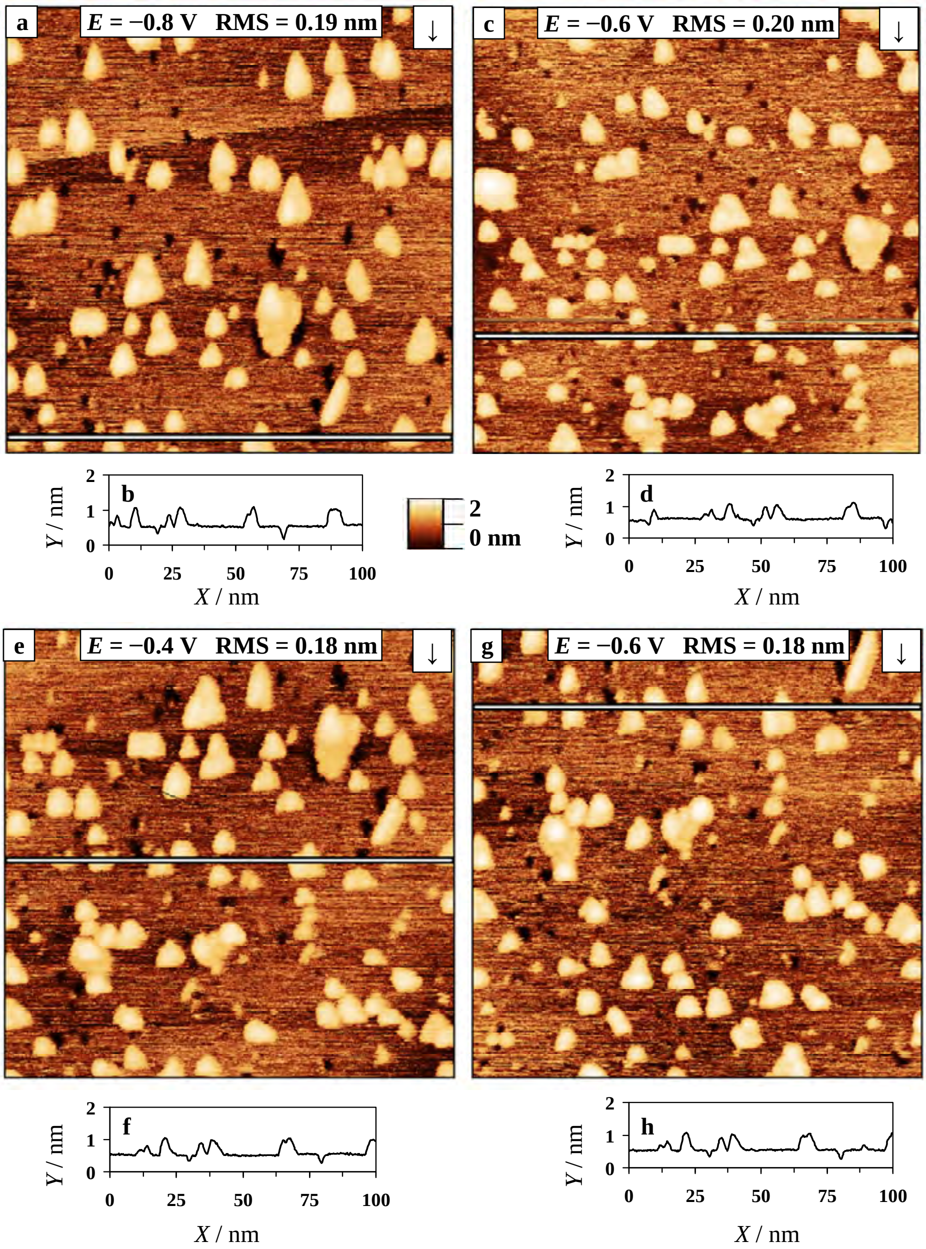

Figure 8. A series of *in situ* STM images of a cleaved Bi(111) electrode in EMImBF$_4$ at negative potentials (noted in Figure) during the first potential sweep: (a), (c), (e), (g), and the corresponding surface height profiles: (b), (d), (f), (h). The scanning parameters were kept constant during the imaging process: $E_{\mathrm{tip}} = 50$ mV, $i_{\mathrm{tunnel}} = 1.0$ nA and $v_{\mathrm{scan}} = 270$ nm/s. Image size: 100 x 100 nm^2.

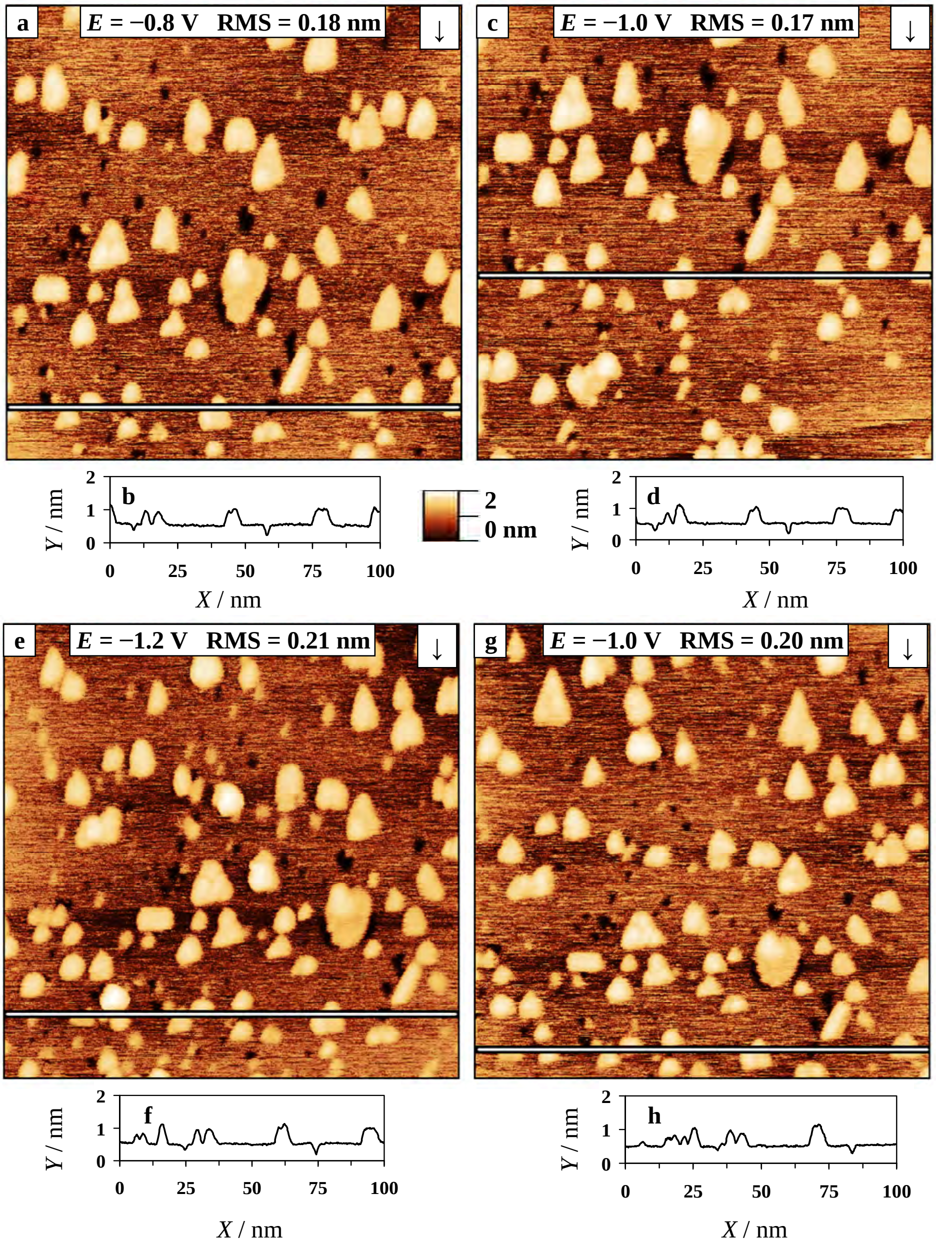

Figure 9. A series of *in situ* STM images of a cleaved Bi(111) electrode in EMImBF$_4$ at negative potentials (noted in Figure) during the first potential sweep: (a), (c), (e), (g), and the corresponding surface height profiles: (b), (d), (f), (h). The scanning parameters were kept constant during the imaging process: $E_{\mathrm{tip}} = 50$ mV, $i_{\mathrm{tunnel}} = 1.0$ nA and $v_{\mathrm{scan}} = 270$ nm/s. Image size: 100 x 100 nm^2.

After the second potential cycle ($-1.2\ \mathrm{V} \le E \le -0.2\ \mathrm{V}$, $t_{\mathrm{pol}} = 25$ h), and a following polarisation at $E = -0.8$ V for 15 h ($t_{\mathrm{pol}} = 40$ h), the value of RMS increases slightly (up to 0.35 nm) (Fig. 10a). Thus, it can be stated that after 40 h of electrochemical studies, the surface structure, roughness parameters and the surface height profiles changed only very slightly (Fig. 10a, 10c and 10d, expressed as slightly increased RMS value). It demonstrates the high stability of Bi(111) | $\mathrm{EMImBF_4}$ interface over time, similarly for a Bi(111) electrode in $\mathrm{BMPyBF_4}$ or $\mathrm{EMImBF_4}$ + 1wt% EMImI mixture (Figs. 6–13) [40,56,62], like for aqueous solutions [3–7].

Thereafter, the third potential cycle from $E = -1.2$ V to $E = 0.0$ V, ($t_{\mathrm{pol}} = 59$ h), ending at the region of oxidation of Bi(111) surface, was measured and again const. $E = -0.8$ V was applied. Obviously, application of the anodic potential, $E = 0.0$ V, for Bi(111) | $\mathrm{EMImBF_4}$ interface increased the values of RMS roughness up to 0.49 nm (Fig. 10b and 10f). As a result, the higher round-shaped surface structures have been formed and observed in Fig. 10b. The height of an average structure measured from surface height profile also has increased significantly, indicating that the surface roughening occurs, which is caused by the oxide formation / reduction and dissolution / redeposition (at $E = -0.8$ V) of the Bi(111) surface (Fig. 10d). The widest few-atomic level terraces with the constant height, *i.e.* the triangular structures throughout the image (shown with black arrows) are still distinguishable, thus, even after polarisation of Bi(111) during 60 h within very wide potential region and applying 3 potential cycles (Fig. 10b and 10f). However, as it is demonstrated later, after the polarisation of Bi(111) at $E = 0.0$ V, it was not possible to obtain the atomic resolution signal no more, which is explained by the anisotropic dissolution and deposition of Bi nanoclusters at Bi(111) surface.

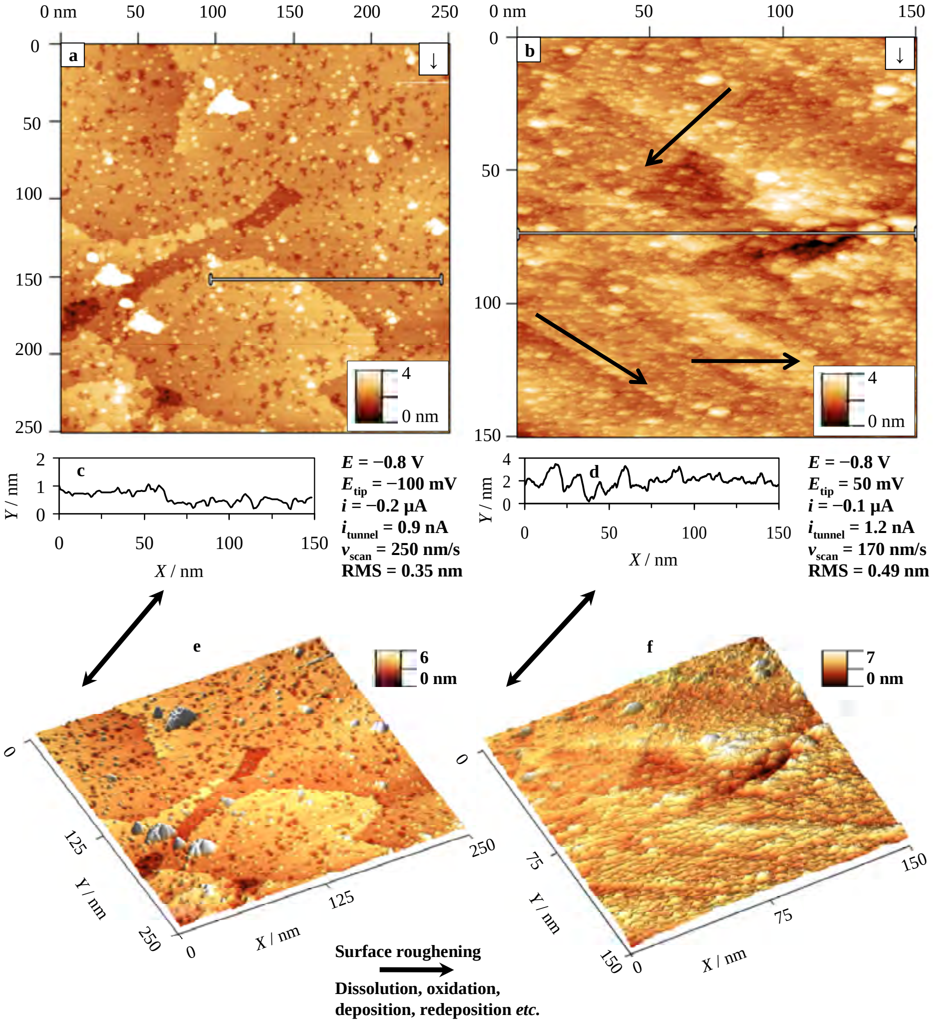

Figure 10. Cleaved Bi(111) electrode in EMImBF$_4$ at negative potential (noted in Figure) after $t_{\mathrm{pol}} = 40$ h (a), and after $t_{\mathrm{pol}} = 60$ h (b), and the corresponding surface height profiles (c) and (d), respectively. Corresponding 3D images of the same Bi(111) surface areas are demonstrated in (e) and (f), respectively.

4.4.2.2 Bi(111) | BMPyBF$_4$ interface

Influence of potential cycling in 0.2 V steps from −1.2 V to −0.6 V and back to −1.2 V for the Bi(111) | BMPyBF$_4$ interface is illustrated in Fig. 11. Data in Fig. 11a–11c show that with the change of E from −1.2 V to −0.8 V, the height and the density of the adsorbed formations, *i.e.* the multilayered adsorption formations and their surroundings, decreases. Therefore, the long-range surface structuring and thickness of the interfacial multilayer, as well as the kinetics of formation of the adsorption multilayer superstructure noticeably depends on E applied. Based on data in Fig. 11, the multilayer formation effect (*i.e.* the non-homogeneous multilayered clusters of the adsorbed compound at Bi(111)) has been observed similarly for Au(*hkl*), glassy carbon and other carbon electrodes [103,107–110], being visible for Bi(111) as the white dots in Fig. 11. The calculated value of RMS roughness for the Bi(111) interface also increases slightly, if the E has more negative values (−1.0 V or −1.2 V).

Data presented in Fig. 11d show that at $E = -0.6$ V there are no white dots at the Bi(111) surface at all. Thus, there are no multilayered formations of adsorbate at the Bi(111) surface at these conditions. However, the appearance of superstructures has been created by potential cycling back to its initial negative value; from −0.6 V to −1.0 V or −1.2 V (Fig. 11d–11f), respectively. The potential cycles for this RTIL were conducted mainly only in the range stated, but the time scale of experimental studies was still up to tens of hours similarly to the Bi(111) | EMImBF$_4$ interface.

In Fig. 12, the time dependency of the BMPyBF$_4$ superstructures can be seen. During polarisation of the Bi(111) | BMPyBF$_4$ interface at $E = -1.2$ V for some hours, the slow formation (adsorption) of the BMPyBF$_4$ superstructure / clusters occurred. The densification of the adsorption layer at the Bi(111) electrode and the increase of RMS roughness for Bi(111) | BMPyBF$_4$ interface took place whilst the first minutes and hours of polarisation at $E = -1.2$ V (Fig. 12a, 12d and 12g). Some superstructures were very high if compared to other superstructures measured immediately after the potential step up to $E = -1.2$ V (Fig. 12). The average height of the superstructures varied from 0.5 nm to 8.0 nm, and the values of RMS roughness from 0.11 nm to 1.14 nm. Therefore, the longer polarisation of the Bi(111) | BMPyBF$_4$ interface at $E = -1.2$ V initiates the formation of bigger adsorption superstructures at Bi(111) surface (Fig. 12a–12f). The very slow processes of adsorption / superstructure formation in RTIL medium was observed for the polycrystalline Au and Au(*hkl*) electrodes as well [34,35]. Moreover, the formation of such multilayered superstructures at the Bi(111) surface (Figs. 11 and 12) is in a good agreement with theoretical calculations, *i.e.* modelling of the multilayer formation at different electrode | RTIL interfaces [28–30,38,91,99, 102,108–113].

The Bi(111) electrode surface in the BMPyBF$_4$ medium was entirely covered by the thin and rather compact, but non-homogeneous RTIL layer (Figs. 11 and 12). Surprisingly, the superstructures were formed even at the multistep terraces (Fig. 12g and 12h). This is a highly interesting result as there is no adsorption of small organic molecules like camphor and 2,2'-, or 4,4'-bipyridine at the defect rich surface areas of Bi(111) electrode studied by *in situ* STM method [3].

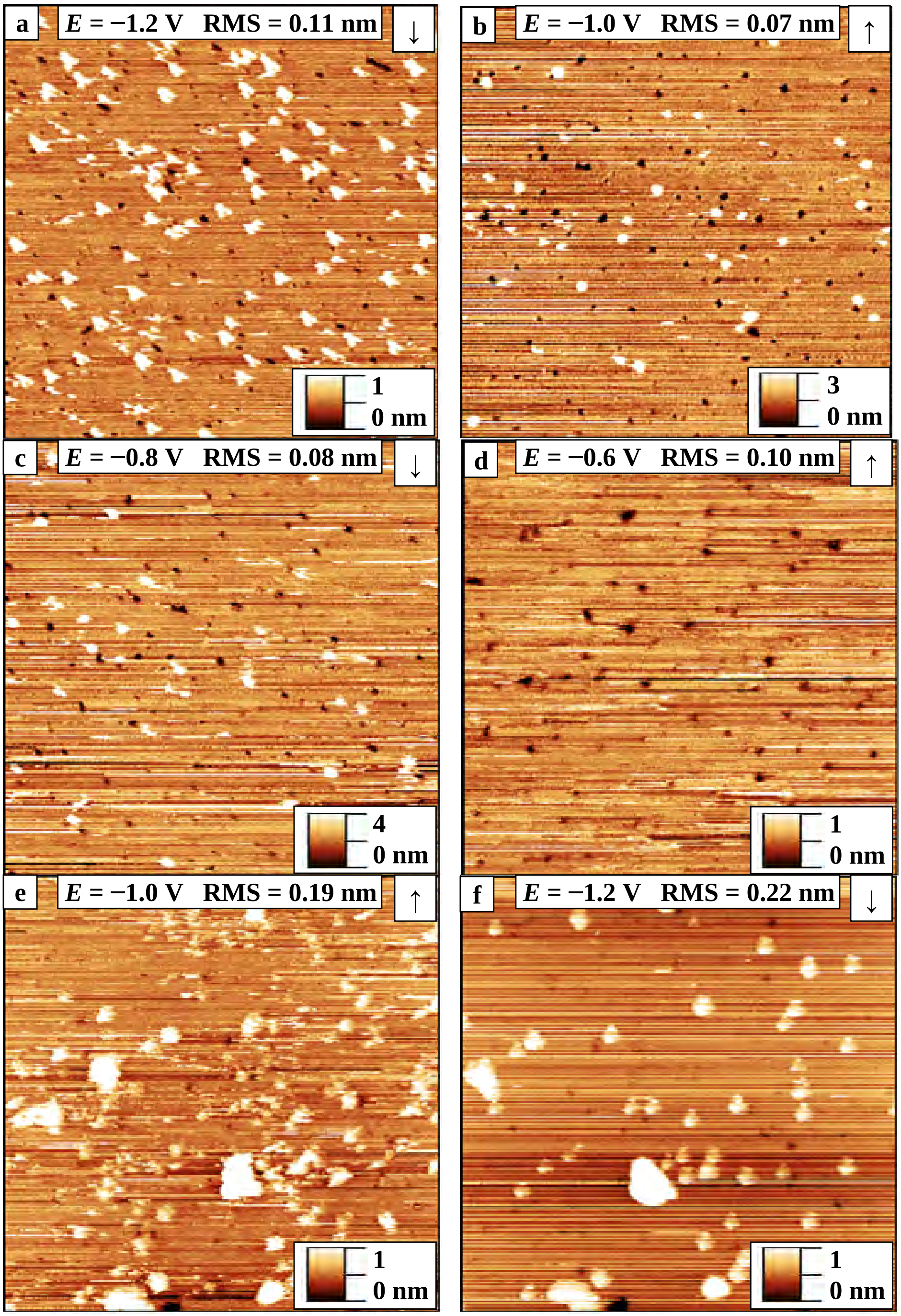

Figure 11. A series of *in situ* STM images of a cleaved Bi(111) electrode in $BMPyBF_4$ at negative potential (noted in Figure) during the first potential sweep: (a) - (f). The scanning parameters were kept constant during the imaging process: $E_{tip} = 50$ mV, $i_{tunnel} = 1.0$ nA and $v_{scan} = 210$ nm/s. Image size: 100 x 100 nm^2.

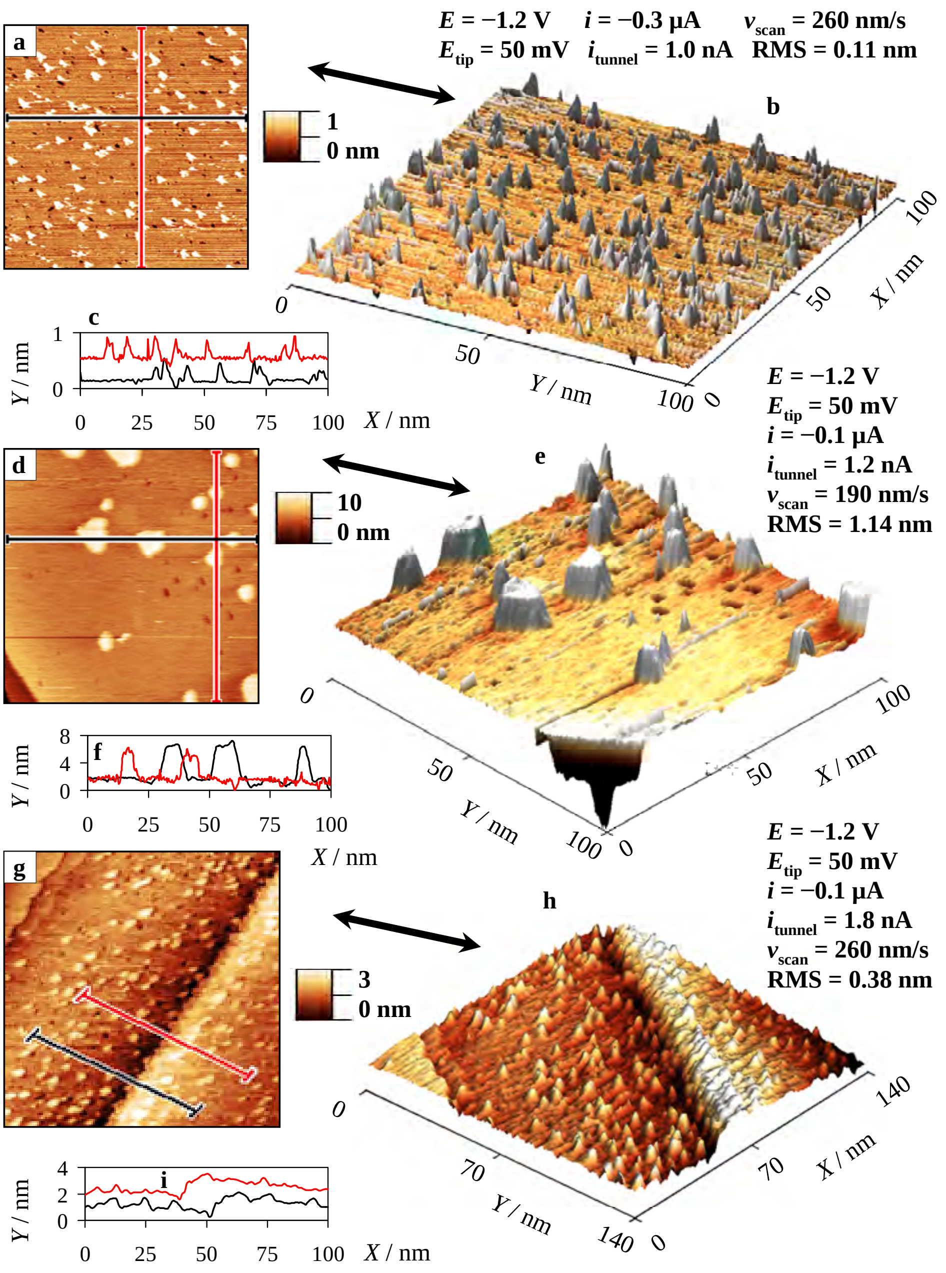

Figure 12. *In situ* STM topographic images for the cleaved Bi(111) electrode in BMPyBF$_4$ (a), (d) and (g) with corresponding 3D images of the same surface area (b), (e) and (h), and with surface height profiles (c), (f) and (i). The images were measured after 2 min (a) - (c), after 1 h (d) – (f), and after 2 h of polarisation time (g) – (i), respectively.

The thicker multilayer structure (Figs. 11 and 12) at the cleaved mono- and multi-atomic steps (exposed at the Bi(111) surface) can also be explained by the existence of the more active Bi(001) or $(01\overline{1})$ planes on the terraced areas, increasing the Gibbs energy of the ions adsorption, which is in a good agreement with our data for the adsorption of inorganic and organic molecules and ions [4,37,49,50,53,54,74,111,115]).

Polarisation times longer than 2 h were not found to influence the values of RMS roughness significantly for this interface. For that reason, we can assume that the thickness of the multilayer seems to be stable in a longer time scale. For the Bi(111) | $BMPyBF_4$ interface at $E = -0.3$ V, where the adsorption process of the BF_4^- anions and STM tip etching started, the surface structures with the height up to tens of nanometers were found. Simultaneously, the irreversible dissolution and oxidation processes of Bi(111) surface already started at $E = -0.3$ V that can probable cause an increase in the values of RMS roughness. However, slow reversible deposition of Bi(111) nano clusters (at $E = -1.2$ V) and dissolution ($E = -0.4$ V) processes of bismuth surface seem to occur in the negative and positive end of the potentials applied during the potential cycling. Therefore, some of the white dots are probably deposited bismuth nano clusters similarly to the Bi(111) | $EMImBF_4$ interface. The surface areas of Bi(111) where the depositions have been formed are small enough, and the calculated values of RMS roughness do not increase significantly.

In addition, for a Bi(111) | $BMPyBF_4$ interface at $E = -0.6$ V, the density of the black triangles observed in Fig. 11d is somewhat higher compared to other potentials applied. Also, a new type of surface roughness defects (the small pit holes) has been developed. Both of these effects could be explained by the specific STM tip etching mechanism [14] in this electrochemically more active RTIL compared to $EMImBF_4$ [116].

More intensive tip etching of the Bi(111) surface occurred in $BMPyBF_4$ at $E \geq -0.4$ V (Fig. 13). The irreversible etching pattern was observed as the non-uniform triangles all over the previously atomically flat Bi(111) surface (Fig. 13c). The *in situ* STM image was measured for exactly the same surface region and the potential was changed by 0.2 V in the positive direction. The etching process did not occur outside the area scanned (200 x 200 nm^2). As a proof, an image of 400 x 400 nm^2 was measured and it can be seen in Fig. 14. The unscanned surface of Bi(111) electrode at $E = -0.6$ V remained flat like in Fig. 13a. The etching process likely occurred when the Bi(111) electrode current densities were positive (over 0.1 $\mu A\ cm^{-2}$). In contrast, the STM tip etching process for Bi(111) | $EMImBF_4$ or Bi(111) | $EMImBF_4$ + 1wt% EMImI interface was not encountered within the range of potentials applied in this work. Due to potential change back to $E = -1.2$ V, the deposition of bismuth has already initiated. In other words, the white dots and islands can be seen and they are stabilised (Fig. 14 compared to Figs. 11a, 11e and 13a, respectively). The shape of a scan is rhombic due to the thermal drift effects of the STM tube scanner (Fig. 14).

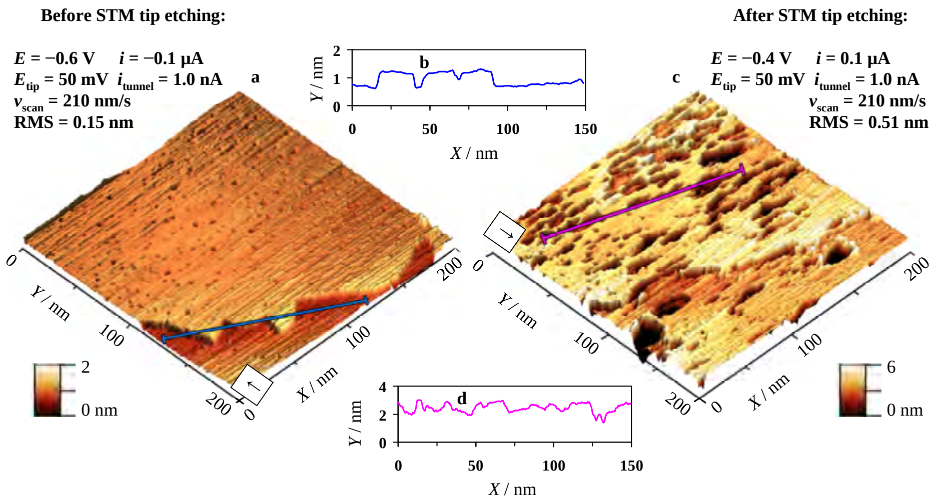

Figure 13. Topographic *in situ* STM 3D images of a cleaved Bi(111) electrode in BMPyBF$_4$ at negative electrode potentials (noted in Figure). Before the etching (a) and after the etching with STM tip (c), and the corresponding surface height profiles (b) and (d), respectively.

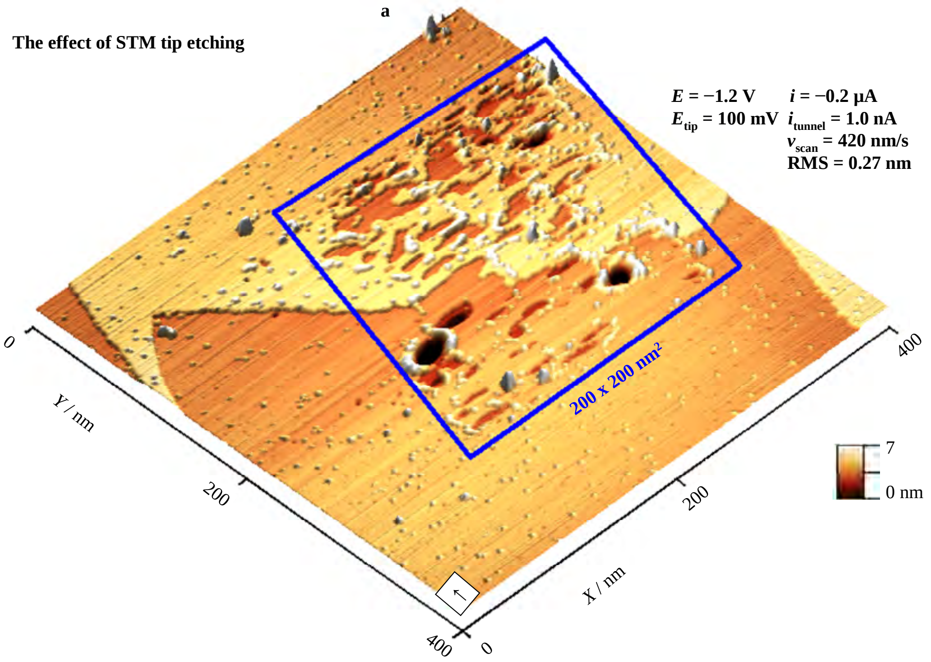

Figure 14. Topographic *in situ* STM 3D image of a cleaved Bi(111) electrode in BMPyBF$_4$ at $E = -1.2$ V (a) after the STM tip etching. The etched area of previous image scanned is marked with a blue rhomb.

4.4.2.3 Bi(111) | EMImBF$_4$ + 1wt% EMImI interface

It was complicated to obtain such atomically flat *in situ* STM images for the Bi(111) | EMImBF$_4$ + 1wt% EMImI interface within the wide negative potential region compared to Bi(111) | BMPyBF$_4$ or Bi(111) | EMImBF$_4$ interface. Only in the case of high negative potentials ($E < -1.0$ V), the Bi(111) surface has the same RMS roughness characteristics as established for pure Bi(111) | RTIL based systems. In addition, a higher level of noise during STM scanning was observed. While E was shifted toward positive direction (by applying 0.2 V and later 0.1 V steps), the *in situ* STM images for Bi(111) surface became blurrier (at $E = -0.8$ V, and especially at $E = -0.6$ V). Polarisation times in tens of minutes up to a few hours were tested at first, but no clear superstructure formation at the Bi(111) surface was observed. In general, the values of RMS roughness calculated for Bi(111) | EMImBF4 + EMImI interface are comparable to those for pure Bi(111) | EMImBF$_4$ or Bi(111) | BMPyBF$_4$ interfaces. Interestingly, the main changes take place after polarisation of Bi(111) at $E = -0.3$ V during a longer period of time (15 h). The adsorbed structures had probably been stabilised, and therefore, it was possible to obtain *in situ* STM images without any noises during *in situ* STM scanning at fixed $E = -0.4$ V. The whole Bi(111) surface was covered with the layers of homogeneous superstructure (Fig. 7c). The “so-called” true superstructure seems to be comparable to iodide anions adsorption on Cu(*hkl*) electrodes established for aqueous solution [117], having higher ordering, if compared to the superstructures obtained for the Bi(111) | BMPyBF$_4$ interface.

The characteristic structures of Bi(111) surface were still visible through the adsorbed 2D-layers (Fig. 7c). However, in some areas the adsorption process of I^- anions occurred actively (Fig. 15a). This assumption was made as the STM tip tunnelling currents were largely fluctuated locally in the case of some areas, for example within the areas marked with the blue circles in Fig. 15a. The result was a periodical pattern with a constant distance between the adsorbed species, which is also demonstrated on the unfiltered surface height profile, given in Fig. 15b, respectively. Fig. 15 clearly demonstrates that the I^- ion adsorption process in the first layers had been completed, but it continued in the next layer(s). However, the RMS roughness values remained similar compared to the clean and atomically flat Bi(111) electrode surface in the RTIL medium (0.22 nm for both Figs. 6a and 15).

While the potential was shifted back to $E = -0.8$ V and $E = -1.0$ V, the *in situ* STM images were observed to become blurry again. In the course of holding E at -1.0 V, the superstructures disappeared slowly and a clean Bi(111) surface was observed. Obviously, the 2D-superstrctures slowly formed once again, if the E was shifted back from $E = -1.0$ V to $E = -0.6$ V or to $E = -0.3$ V.

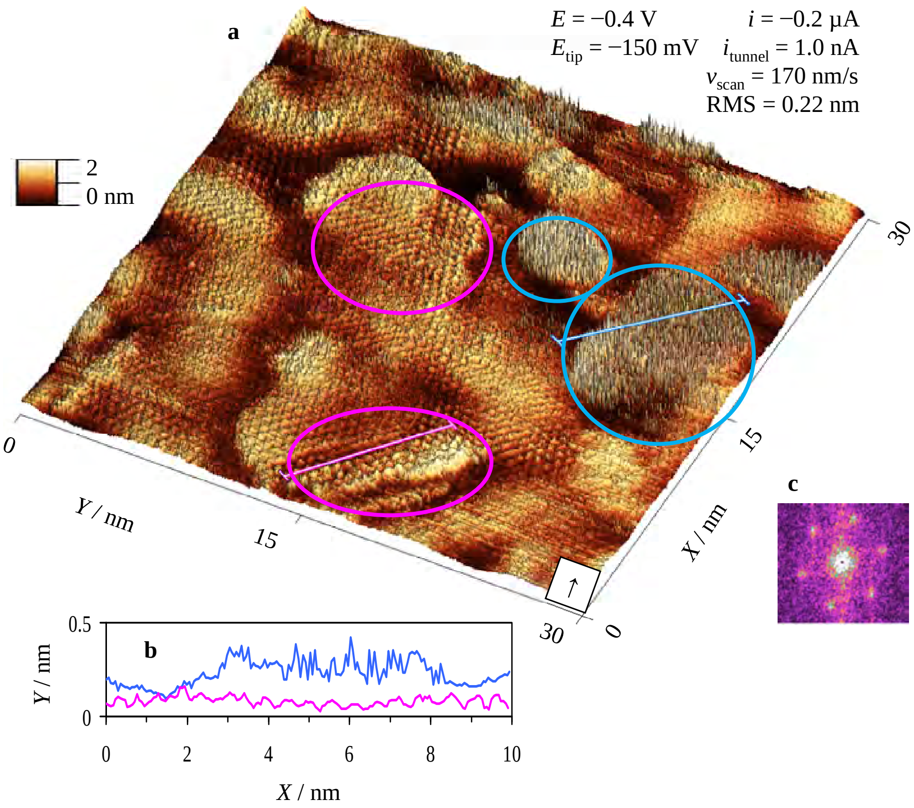

Figure 15. *In situ* STM data for Bi(111) | $EMImBF_4$ + 1wt% EMImI interface at −0.4 V (*vs.* Ag | AgCl in same RTIL mixture). The signal fluctuation during *in situ* STM imaging due to in real time ion adsorption process is marked with blue circles, while the areas of the ions already strongly adsorbed, and therefore, stabilised in a higher-ordered layer are marked with pink circles. Corresponding FTT image with the periodical signal of the adsorbed ions is given in (c).

It should be pointed out that the changes at the Bi(111) | RTIL interfaces, initiated by electrode potential changes and estimated by the *in situ* STM method, were significantly slower than the changes connected with the adsorption of organic compounds at Bi(111) surface from aqueous solutions. Only some seconds were needed to create a 2D-layer superstructure in a real time for 2,2'- or 4,4'-bipyridine or camphor from $Na_2SO_4 + H_2SO_4$ aqueous solutions onto Bi(111) surface. But, for Bi(111) | $EMImBF_4$ + 1wt% EMImI interface, the time constant was observed to be in several minutes up to hours. The values of τ_{ch} for the $EMImBF_4$ on Bi(111) electrode are similar, but slightly lower than the values for $BMPyBF_4$ estimated by the in situ STM method. As stated before, the $EMIm^+$ cations have greater mobility in $EMImBF_4$ compared to $BMPy^+$ cations mobility in $BMPyBF_4$. Also, the viscosity is lower and dielectric permeability is slightly higher for $EMImBF_4$, still causing several minutes up to hours to obtain stable *in situ* STM images at the potentials studied in this work. Hence, we can state that in addition to the conclusions made by the impedance measurements for all RTIL systems, the very slow adsorption kinetics of ions (specifically adsorbed I^{-}) and EDL formation has been observed using the *in situ* STM method as well.

4.4.3 High-resolution *in situ* STM data for Bi(111) | RTIL interface

4.4.3.1 Atomic resolution data

STM tip scanning rate, v_{scan}, is defined as a movement of tip over Bi(111) surface (in nm/s) during the scanning process. When the v_{scan} is smaller, the tip has more time to be in contact with the surface, and therefore, greater impact (interplay) between the tip and the surface occurs. Therefore, the lower v_{scan} were usually preferred for atomic signal imaging applicable for smaller surface areas (~100 nm/s), while greater v_{scan} (~400 nm/s) was found to be optimal for scanning of the larger surface areas.

STM tip potential, E_{tip}, is defined as a difference of tip potential in mV with respect to E_{ref} (*vs.* Ag | AgCl in the same RTIL) (Eq. (18) in ch. IV.4.). E_{tip} also defines the movement direction of electrons from tip to the surface or *vice versa*. In this work, the positive tip potential (so-called tip bias) determines the electron flow from the Bi(111) surface to the STM tip, and thus, corresponds to the negative working electrode potential with respect to the positively charged tip apex. The local influence of a STM tip is weaker at $E_{\mathrm{tip}} > |\,200\ \mathrm{mV}\,|$, if compared to $E_{\mathrm{tip}} > |\,20\ \mathrm{mV}\,|$, based on the Eq. (18) [63]. For this reason, the smaller values of E_{tip} are usually preferred during Bi(111) atomic resolution signal imaging in this work.

The tunnelling current, i_{tunnel}, is defined as a magnitude of current flow between the STM tip and the surface. For images of atomic level resolution, i_{tunnel} usually varies from 1 nA to 10 nA. The greater value of i_{tunnel} corresponds to stronger impact between the tip and surface, and this is sometimes preferred if the background currents for a system are relatively high (if faradic reactions take place at an interface).

For the Bi(111) | EMImBF$_4$ interface, high-resolution *in situ* STM images at $E = -1.2$ V and -0.8 V were obtained after the first and second potential cycle (6 h and 28 h Fig. 16b and 16c, respectively). Corresponding FFT filtered images have been calculated and the surface profiles have been measured (Fig. 16e and 16f). Comparison of the data given in Fig. 16 demonstrates that there are only minor differences in these atomic resolution level images. Due to the thermal drift and significant oxidation / reduction processes at $E = -0.1$ V (at some more active stepped surface areas), the data measured after setting E back to $E = -0.8$ V, are slightly distorted (Fig. 16c).

For the EMImBF$_4$ + 1wt% EMImI mixture [56,62], the clean Bi(111) surface along with the characteristic atomic resolution was achieved only in the negative end of potentials, *i.e.* at $E \leq -1.0$ V.

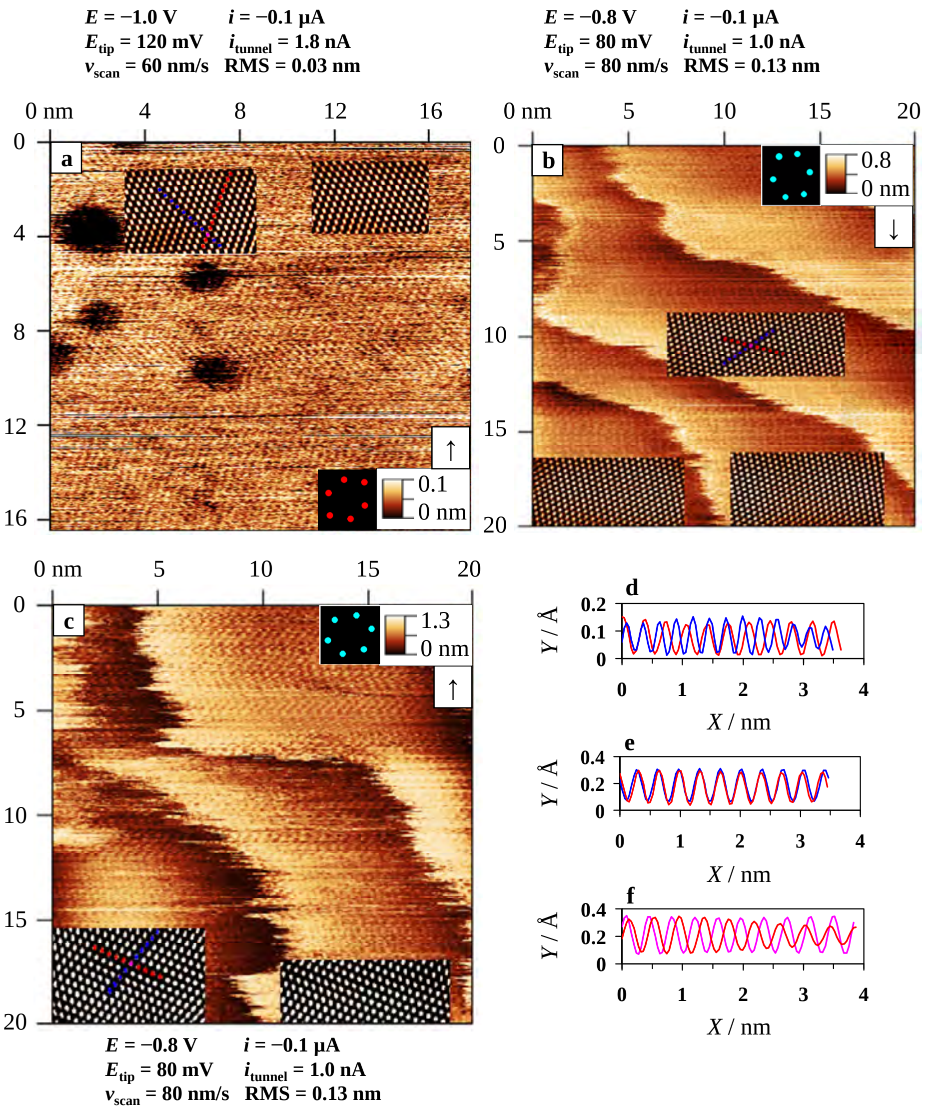

Figure 16. High-resolution *in situ* STM images for a cleaved Bi(111) electrode in EMImBF$_4$ (a), and for an electrochemically polished Bi(111) electrode after 6 h (b) and after 28 h (c) at negative potentials (noted in the Figure), and the corresponding surface height profiles (d), (e) and (f). A fast Fourier filtered periodical atomic signal image is shown in the right upper corner of each image.

For Bi(111) | BMPyBF$_4$ interface, the atomic resolution level images were also regularly observed and one example at $E = -1.2$ V is demonstrated in Fig. 17. After the fast FTT filtering and even at the raw (unfiltered) image, the characteristic rhombohedral structure for the Bi(111) surface has been obtained

(Fig. 17a and 17b). It should be pointed out that the atomic signal was detected at multiple levels of surface height simultaneously in several experiments for Bi(111) | EMImBF$_4$ or Bi(111) | BMPyBF$_4$ interface as demonstrated in Figs. 16 and 17.

Distances between the electron density localisation points were measured being 3.5 ± 0.2 Å, that correspond to the individual atoms at the clean Bi(111) surface layer. This value is in a good agreement with the data obtained for Bi(111) surface in aqueous electrolytes [3–7,40,62,104,105]. Of course, the atomic resolution data for all interfaces under study was independent of E, E_{tip}, v_{scan}, i_{tunnel} applied and experimental, *i.e.* polarisation time.

Blurred areas observed for the Bi(111) electrode at some step edges of mono-atomic height are similar to Au(111) or Ag(111) electrodes, observed in aqueous electrolytes, and systematically analysed by Kolb *et al.* [81,118]. The electron densities seem to oscillate rapidly along the edges of steps for Bi(111) surface most probably because the surrounding ions of RTIL interfere with the STM tip during scanning process. As stated before, there is no potential induced surface reconstruction process at the surface of Bi(111) electrode. Hence, the surface structure remains nearly unchanged within the whole region of ideal polarisability.

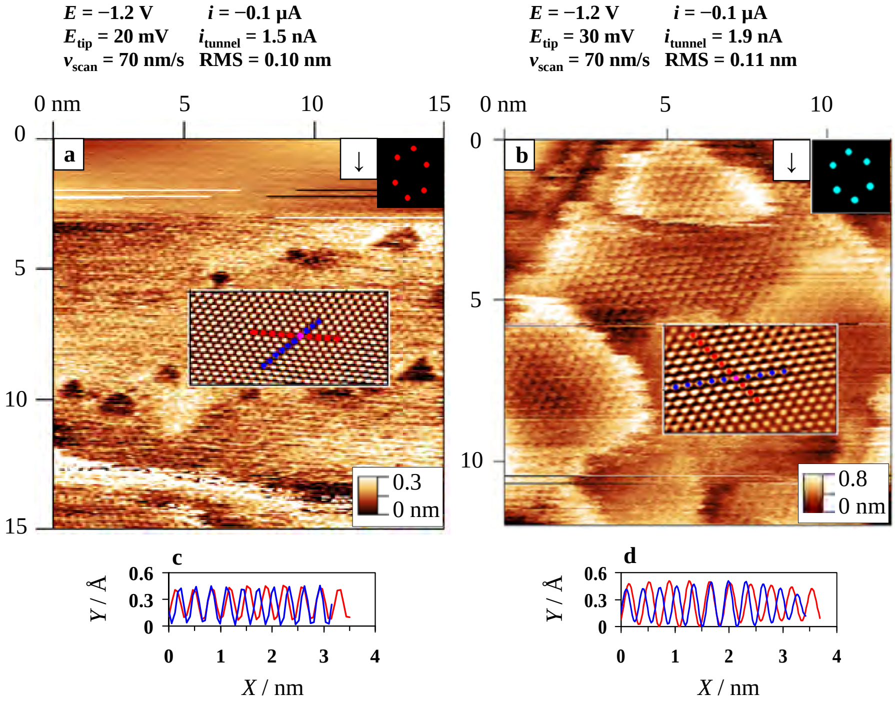

Figure 17. High-resolution *in situ* STM images for a cleaved (a), and electrochemically polished (b) Bi(111) electrodes in BMPyBF$_4$, and the corresponding surface height profiles (c) and (d).

4.4.3.2 Ionic resolution data

For the Bi(111) | EMImBF$_4$ interface, many combinations of *in situ* STM scanning parameters have been used, but differently from EMImBF$_4$ + 1wt% EMImI mixture, no superstructure formation has been observed [56,62]. Nevertheless, well-expressed superstructures have been reported at electrified Au(*hkl*) | imidazolium cation based ionic liquid interfaces by several groups: Mao *et al.* [42,82], Pajkossy *et al.* [86] and Endres *et al.* [119,120]. In contrast, the EIS measurements at Bi(111) also strongly refer to the ongoing adsorption-desorption processes of the ions at Bi(111) surface at various potentials for all Bi(111) | RTIL interfaces under study. It is probably due to the greater degree of mobility of smaller and less strongly adsorbing electrolyte ions in the EDL region (locally probed by STM tip). The weak physical adsorption of cations (EMIm$^+$) and anions (BF$_4^-$) at Bi(111) from this RTIL probably prevents the *in situ* STM images to be resolved on the high resolution level at room temperatures.

For the Bi(111) | BMPyBF$_4$ interface, interactions between the RTIL and Bi(111) surface seem to be stronger compared to those for Bi(111) | EMImBF$_4$ interface. Therefore, a different type of superstructure was observed for Bi(111) | BMPyBF$_4$ interface. Still, the ionic level resolution of *in situ* STM images was not reached, but only randomly located multilayered structures at slightly higher magnifications were obtained. Interestingly, these structures were also stable under a wide range of *in situ* STM scanning parameters (described further in chapter VI.4.4.4), and electrode polarisation applied. The formation of superstructures in this RTIL is in a good agreement with the data collected applying the EIS measurements (Figs. 3-5).

Based on *in situ* STM and EIS data for a EMImBF$_4$ + 1wt% EMImI mixture, much stronger electrochemical co-adsorption process of I$^-$ and BF$_4^-$ anions occurs compared to a pure Bi(111) | EMImBF$_4$ system [56,62]. At $E > -0.8$ V, the iodide anion adsorption process starts, and therefore, 2D-superstructures can be visualised by the *in situ* STM method. Thus, the region of potentials, $-0.8\text{ V} \leq E \leq -0.3$ V, can be confirmed as a potential region of iodide anion adsorption from an EMImBF$_4$ + 1wt% EMImI system at Bi(111) (Figs. 7c, 15, 18 and 19). Based on the *in situ* STM images obtained, the strongest adsorption occurs at $\sim E = -0.3$ V (Fig. 19a). The desorption process of iodide anions occurs at $E \leq -0.8$ V (Figs. 18a and 19c), and consequently, clean Bi(111) surface can be observed again at $E \leq -1.0$ V.

In general, the adsorption-desorption processes of iodide anions at Bi(111) surface seem to be reversible as it was possible to visualise the 2D-superstructures during the next potential cycles. At $E \geq -0.2$ V, as noted before, the Bi(111) surface starts to oxidise irreversibly in this mixture of RTILs, and as a result a quick surface roughening occurs (Fig. 19b and 19c), while almost all signals characteristic of superstructures are lost (Fig. 19c).

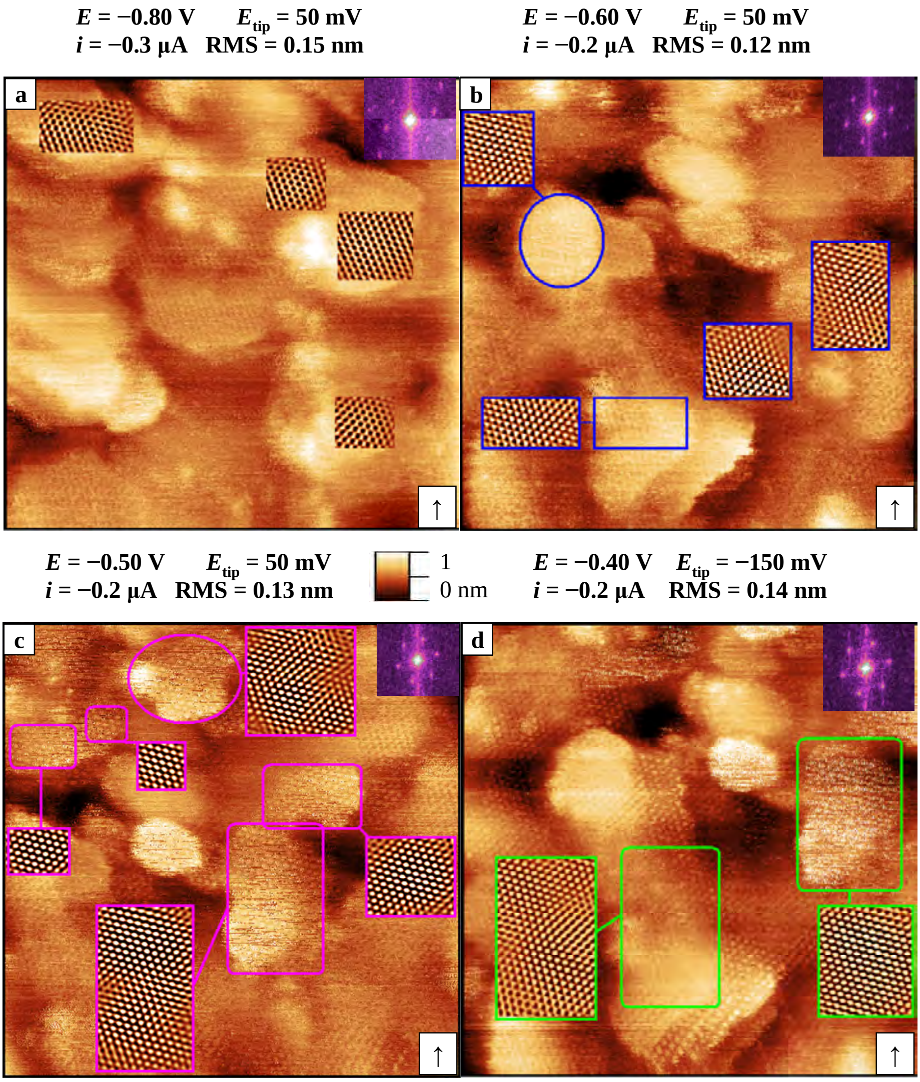

Figure 18. A series of *in situ* STM images of an electrochemically polished Bi(111) electrode in a mixture of $EMImBF_4$ + 1wt% EMImI at negative potentials (noted in Figure). Image size: 30 x 30 nm^2. I_{tunnel} = 1.0 nA and v_{scan} = 170 nm/s were kept constant during the imaging process.

It should be noted that at the beginning of *in situ* STM measurements, the 2D-superstructures were not clearly detected, as the adsorption processes from RTIL are known to be very slow (Fig. 18a). The adsorbed 2D-superstructures appeared after holding the Bi(111) electrode at constant *E* = −0.3 V for 15 h. The 2D-superstructure formed was stable within the potential cycling from −0.8 V to −0.3 V (Figs. 18 and 19).

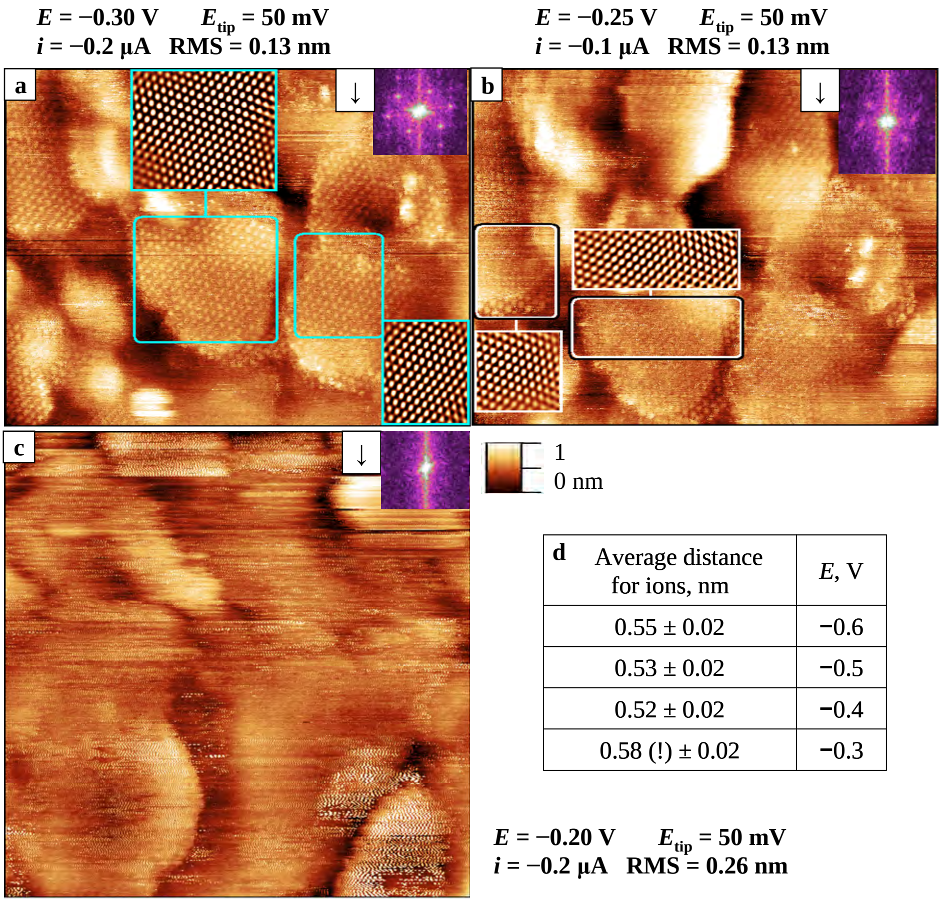

d Average distance for ions, nm	*E*, V
0.55 ± 0.02	−0.6
0.53 ± 0.02	−0.5
0.52 ± 0.02	−0.4
0.58 (!) ± 0.02	−0.3

Figure 19. A series of *in situ* STM images of an electrochemically polished Bi(111) electrode in a mixture of EMImBF$_4$ + 1wt% EMImI at negative potentials (given in Figure). Image size: 30 x 23 nm^2 for (a) and (b), and 30 x 30 nm^2 for (c). I_{tunnel} = 1.0 nA and v_{scan} = 170 nm/s were kept constant during the imaging process. The average distances of the adsorbed ions measured based on Figs. 18 and 19 are given in a table (d), respectively.

In this region of potentials studied (Figs. 15, 18 and 19), the values of RMS roughness also do not depend on *E* applied. After potential steps within the specified *E* region, stable *in situ* STM images can be measured after minutes of holding of Bi(111) at a constant *E*. Interestingly, it was also found that during a series of *in situ* STM measurement cycles the signal for adsorbed 2D-superstructure became stronger after the long lasting polarisation cycling from −0.8 V to −0.3 V (Figs. 18 and 19).

The series of FTT images corresponding to the *in situ* STM images are also demonstrated in Figs. 18 and 19. Areas with the brighter contrast in FTT image, *i.e.*, the peaks in a hexagonal pattern correspond to the periodic signal of the adsorbed species on the (111)-type of surface. Logically, the higher stability of the interfacial structure is confirmed by a lesser amount of signal fluctuation during *in situ* STM imaging process (Figs. 15, 18 and 19). In addition, the atomic resolution signal for a clean Bi(111) surface was not observed under these *in situ* STM scanning conditions or corresponding FTT images (Figs. 18 and 19). It should be noted that the periodical atomic signal in these FTT images would have also 6 peaks in an order of a (111) position, but their distances must be different by a factor of $\sim(0.53 / 0.35)^{-1} \approx 1.5^{-1}$. The factor of 1.5 is the average difference in the distances between the Bi(111) atoms (~0.35 nm) and the adsorbed I^{-} anions (~0.53 nm) at the Bi(111) surface (Figs. 15–19). The $()^{-1}$ parameter is because of FTT images use an inverted scale. In other words, there should be 6 + 6 = 12 separated peaks in FTT image, each in a form of a hexagonal placement structure. In theory, when the adsorbed 2D-layer is a monolayer (adsorbed weakly), the atomic resolution of a substrate could be seen at least partially on these images at some potentials applied. Therefore, the structure of this adsorption layer formed on Bi(111) is not a monolayer, but a multilayer.

Based on the data collected, the distances measured between the electron density localisation points are noticeably longer (by a factor of ~1.5 times) for Bi(111) | $EMImBF_4$ + EMImI interface (Figs. 18 and 19) compared to the Bi(111) | $EMImBF_4$, Bi(111) | $BMPyBF_4$, and Bi(111) | Na_2SO_4 aqueous solution interfaces [40]. Further analysis of *in situ* STM data shows that a small variation in the average distances between the adsorbed iodide ions, has been observed (5.2 ± 0.2 Å), if E changes from −0.8 V to −0.3 V. The variation in the average distances for iodide anions positions at the Bi(111) surface calculated could be caused by an increasing interaction energy between the specifically adsorbed I^{-} anions and Bi(111) surface atoms (Figs. 18 and 19). It should be also noted that in Paper 3, the average distance of the adsorbed iodide anions at Bi(111) from RTIL mixture measured was 4.8 ± 0.2 Å, but after the further studies within wider I^{-} adsorption region the distance of 5.2 ± 0.2 Å has been found to be more overwhelming and more characteristic.

In situ STM results (Figs. 15, 18 and 19) are in a very good agreement with the impedance results (Figs. 3–5), indicating that the specific adsorption of I^{-} anions and coadsorption of $EMIm^{+}$ cations at Bi(111) surface (ion pair formation) occurs. However, the adsorption-desorption processes of iodide anions seem to be reversible and the formed 2D-superstructure probably protects the Bi(111) surface from a quick irreversible oxidation at $E \leq -0.3$ V [1,4,15,56]. Otherwise it would have not been possible to maintain the flat Bi(111) surface over such a wide range of potentials from $E = -1.2$ V to $E = -0.3$ V.

4.4.4 Influence of the *in situ* STM scanning parameters on the Bi(111) | RTIL interfacial structure

For the most positive electrode and tip potentials (E and E_{tip}) applied during the *in situ* STM experiments conducted in this work, there is also a possibility that an electrochemical process is activated by potentials applied, including (H_3O^+) reduction and oxidation of the (electro)chemically stable tungsten STM tips. In theory, the STM tip can work as a forth electrode in the three-electrode cell, if the currents and or potentials are higher than the critical values. However, the electrochemical limits for STM tip operation possibilities are also affected by the electrolyte composition used. As a result, the STM tip can dissolve or oxidise according to its thermodynamic characteristics, given in *Pourbaix* diagrams for aqueous solutions. Due to the presence of small amounts of H_2O in RTIL the same Pourbaix diagrams can be useful for the *in situ* STM experiment in this work. Therefore, the sharpness of a tip can degrade and as a result of the oxidation and dissolution of tungsten tip *in situ* STM images may appear blurrier at positive potentials applied. At low Bi(111) negative potentials, the negative polarisation of a STM tip is preferred. Thus, control over the sharpness of a STM tip was carefully maintained during the *in situ* STM experiments.

In addition to the main driving force during *in situ* STM experiments, the electrode potential, in some cases there were more correlations of parameters. Unfortunately, clear explanations could not be given for every situation. For example, the detection of the adsorption layer superstructure of RTIL on the Bi(111) surface is somewhat dependent on the values of E_{tip} and i_{tunnel} applied (Fig. 20), which can be explained by the semi metallic nature of the Bi(111) electrode [1,3,4,46,50,121,122].

Interestingly, for the Bi(111) | $BMPyBF_4$ interface, $E_{\text{tip}} \leq -80$ mV (and) $E_{\text{tip}} \geq 45$ mV seemed to be favourable for detecting the superstructures at Bi(111) surface (Figs. 20 and 21). However, when E_{tip} had been changed from −80 mV to −60 mV, the value of RMS roughness decreased nearly by half (from 0.69 nm to 0.46 nm). Comparable influence of E_{tip} effect was observed when it was changed from −60 mV to 45 mV (Fig. 21a and 21b).

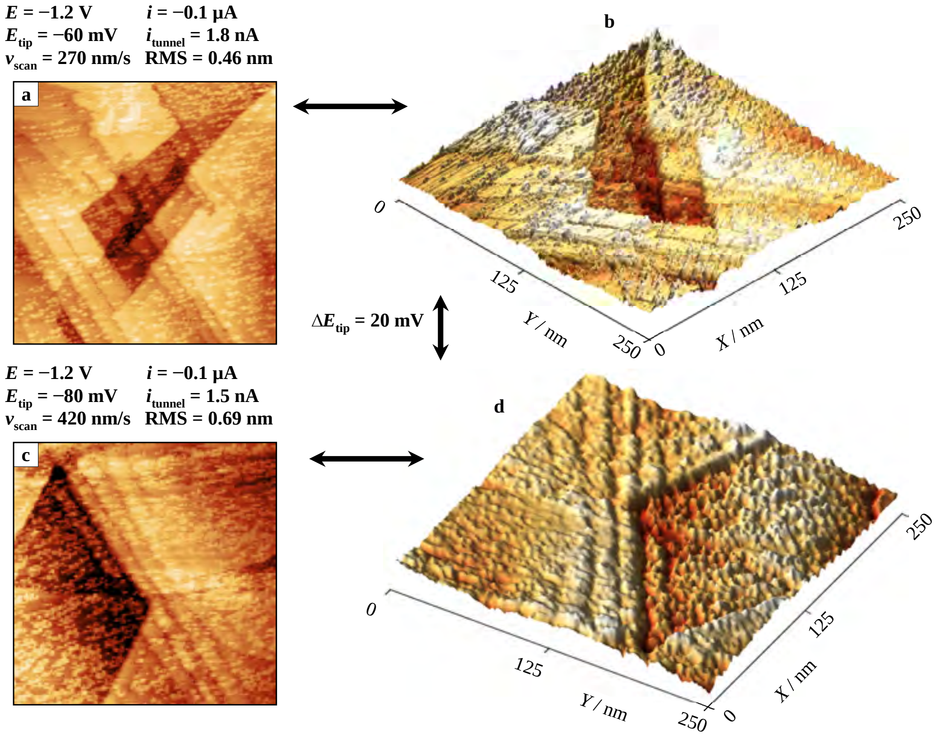

Figure 20. *In situ* STM topographic images (a) and (c), and corresponding 3D images (c) and (d) for a cleaved Bi(111) in $BMPyBF_4$ after 1 h of the cathodic polarisation at $E = -1.2$ V in the case of E_{tip} of −60 mV (a), (b) and −80 mV (c) and (d), respectively.

The most heterogeneous superstructure, *i.e.* complicated adsorption layer, was observed at $E_{tip} = -80$ mV (Fig. 20c and 20d), while the least amount of adsorbed surface structures, not characteristic of Bi(111) surface, were estimated at $E_{tip} \geq -20$ mV or $E_{tip} \leq 20$ mV. Also, the atomic resolution data for Bi(111) was observed at the strongest tip-sample interaction conditions (Fig. 17). The amount of superstructures for Bi(111) | $BMPyBF_4$ interface also depend somewhat on the potential scanning rate (v_{scan}). Thinner superstructures were likely observed, if v_{scan} was higher ($v_{scan} > 400$ nm/s) (Fig. 20), compared to its values sufficient for a regime of atomic resolution imaging ($v_{scan} < 100$ nm/s) (Fig. 17).

However, in the case of Bi(111) | $EMImBF_4$ and Bi(111) | $EMImBF_4$ + 1wt% EMImI interfaces, such dependence on E_{tip} applied, was not clearly observed. Based on the results of *in situ* STM method, an assumption can be made that the adsorption interactions for the system containing the I^- anions are essentially stronger. Therefore, more energy is needed to change the surface structures compared to Bi(111) | $BMPyBF_4$ interface.

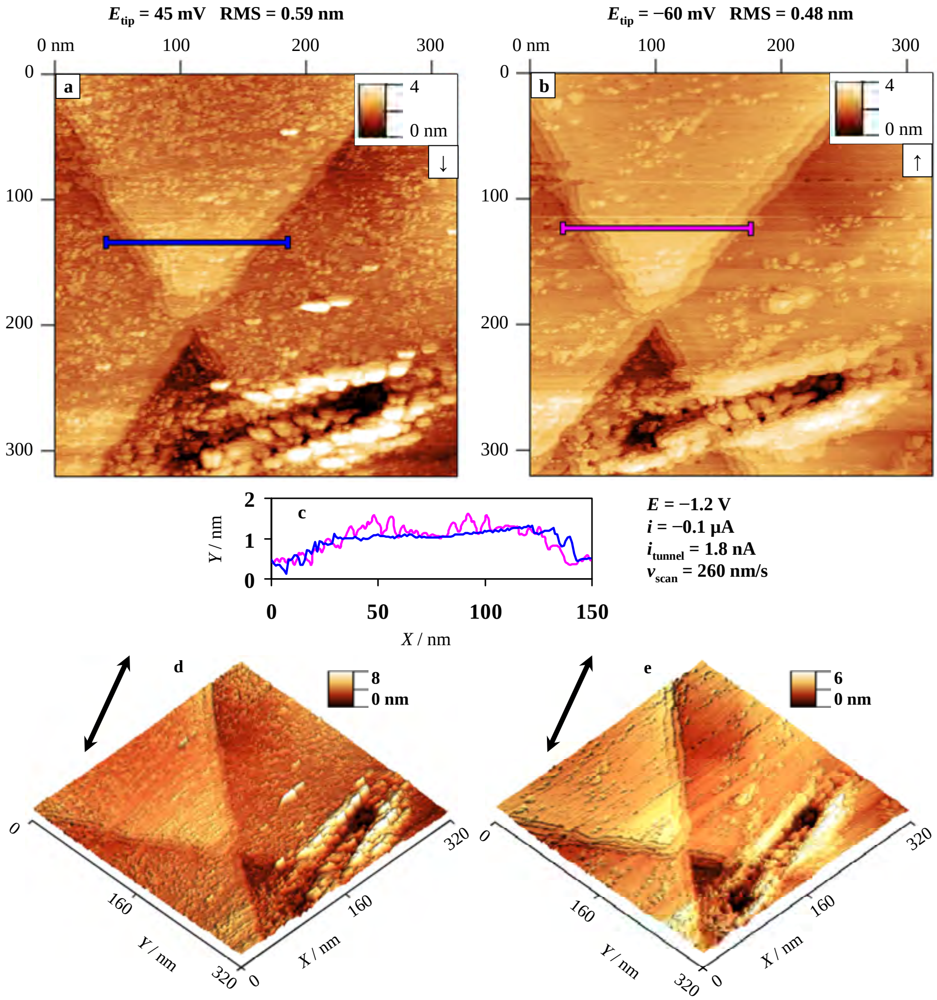

Figure 21. Topographic *in situ* STM images of a cleaved Bi(111) electrode in BMPyBF$_4$ at −1.2 V (a) and (b), the surface height profiles (c) corresponding to the lines marked in (a) and (b), 3D images (d) and (e), respectively. The effect of E_{tip} fixed at −60 mV and 45 mV is demonstrated in Figure, respectively.

It should also be noted that during the *in situ* STM experiments, significantly wider ranges of scanning parameters including E_{tip} (from −200 mV to 200 mV), i_{tunnel} ($0.1\ \text{nA} < i_{\text{tunnel}} < 10.0\ \text{nA}$), and v_{scan} ($30\ \text{nm/s} < v_{\text{scan}} < 1000\ \text{nm/s}$) were applied and the results obtained were analysed carefully. As there was no clear correlation and a good reproducibility of results (along with a reasonable interpretation of data) obtained at the higher values of E_{tip}, i_{tunnel}, and v_{scan}, only the reproducible phenomena have been demonstrated and discussed within this work.

4.4.5 Comparative fitting of Bi(111) | RTIL interface and solid oxide fuel cell materials by applying selective grain analysis method

The surface structure and topography of solid oxide fuel cell (SOFC) cathodes, anodes and electrolytes has been studied by non-contact AFM method. The discussion of method and exact composition of cathodes analysed is given in Paper 1 [123], and for shortness it is not discussed here.

Based on the data collected, the surface height profiles, RMS roughness and grain distributions (GD) have been calculated (Fig. 22). A specially designed network is drawn on the surface as a result of GD modelling (Fig. 22b).

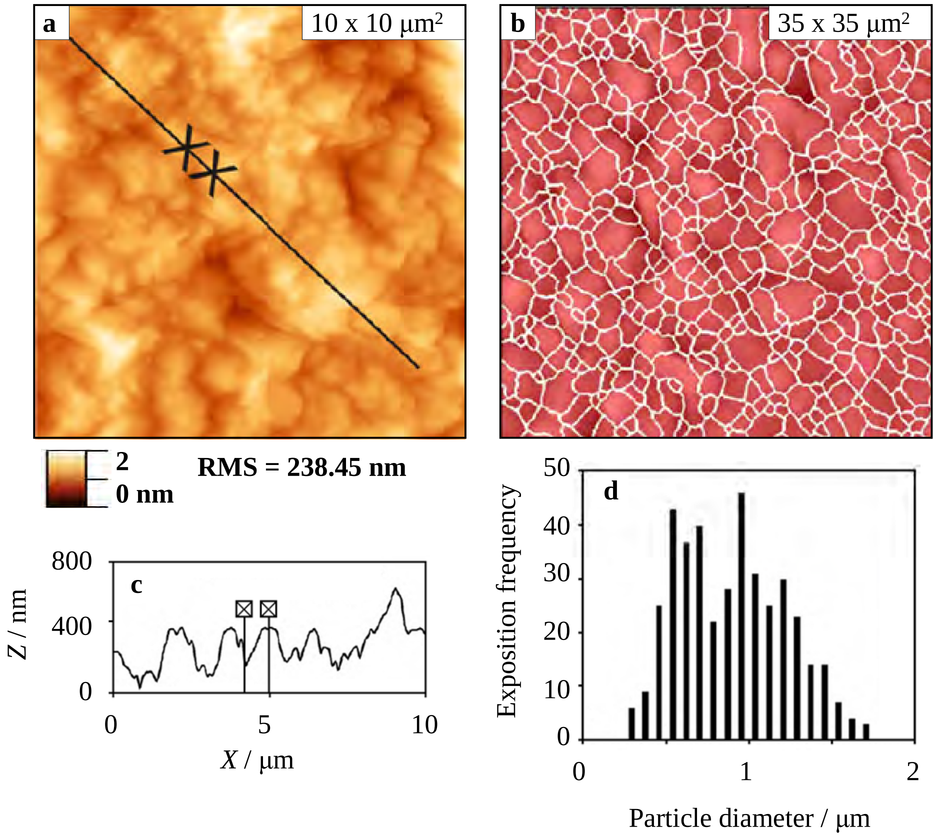

Figure 22. Topographic AFM image for a $La_{1-x}Sr_xCoO_{3-y}$ (LSCO) cathode, which was prepared from corresponding nanopowders by using a nitrate solution thermal combustion method at $T_{sint} = 1373$ K (a). A model net was drawn by using Gwyddion software (b), selected surface height profile (c), and a distribution function of an average particle size were calculated (d).

In the case of SOFC electrodes, the average grain size is dependent on the chemical composition used, as well as on sintering temperature of the materials (T_{sint}) applied. While T_{sint} is increased during the material finishing (sintering) procedure, the particles on the surface grow bigger and interfacial grains (phase boundaries) are formed. However, if T_{sint} is not high enough, the average grain size remains more similar to those for raw powders used for a preparation step of the cathode materials. Therefore, T_{sint} and its duration can adequately be correlated with surface roughness parameters and grain sizes for SOFC electrodes.

Based on data collected and analysed in Paper 1 [123], the average grain size was estimated being from 0.5 μm to 1.3 μm for a typical $\mathrm{Pr_{1-x}Sc_xCoO_{3-y}}$ or $\mathrm{Gd_{1-x}Sr_xCoO_{3-y}}$ cathode after sintering at 1373 K (Fig. 22d), respectively. It should be also noted that the AFM data correlate well with the data obtained with Scanning Electron Microscopy method, and thus, a convolution of an AFM tip was not a problem here.

For modelling a Bi(111) | RTIL interface the GD calculations at least in two fundamentally different cases can also be applied. The surface roughening of the Bi(111) electrode achieved by irreversible anodic dissolution has been quantified in Fig. 23. The specifically adsorbed anions have been estimated and data are given in Fig. 24.

In Fig. 23, *in situ* STM image of a cleaved Bi(111) electrode in $\mathrm{EMImBF_4}$ is visualised before and after anodic dissolution steps, respectively. In the case of Bi(111) electrode before dissolution (Fig. 23a), the amount of depositions and holes on the Bi(111) surface is significantly lower, if compared to the surface characteristics after the anodic dissolution steps. The difference is visualised in the average particle diameter (being 1.5 ± 0.5 nm and increasing) and overall distribution histograms along with the number of events (frequency counts) (Fig. 23b, 23d and 23f). The GD fitting data established are in a good agreement with the values of RMS calculated and discussed in chapter VI.4.4.2.1, Figs. 8–10. Note that the inverted colour scales are used for visualisation effect in Fig. 23a and 23c. The GD calculations use the opposite net filters instead. At $E = -0.2$ V, the amount of white small depositions increases (Fig. 23c and 23d). In addition, anisotropic dissolution of Bi(111) surface occurs in the areas demonstrated with the darker contrast (in Fig. 23c).

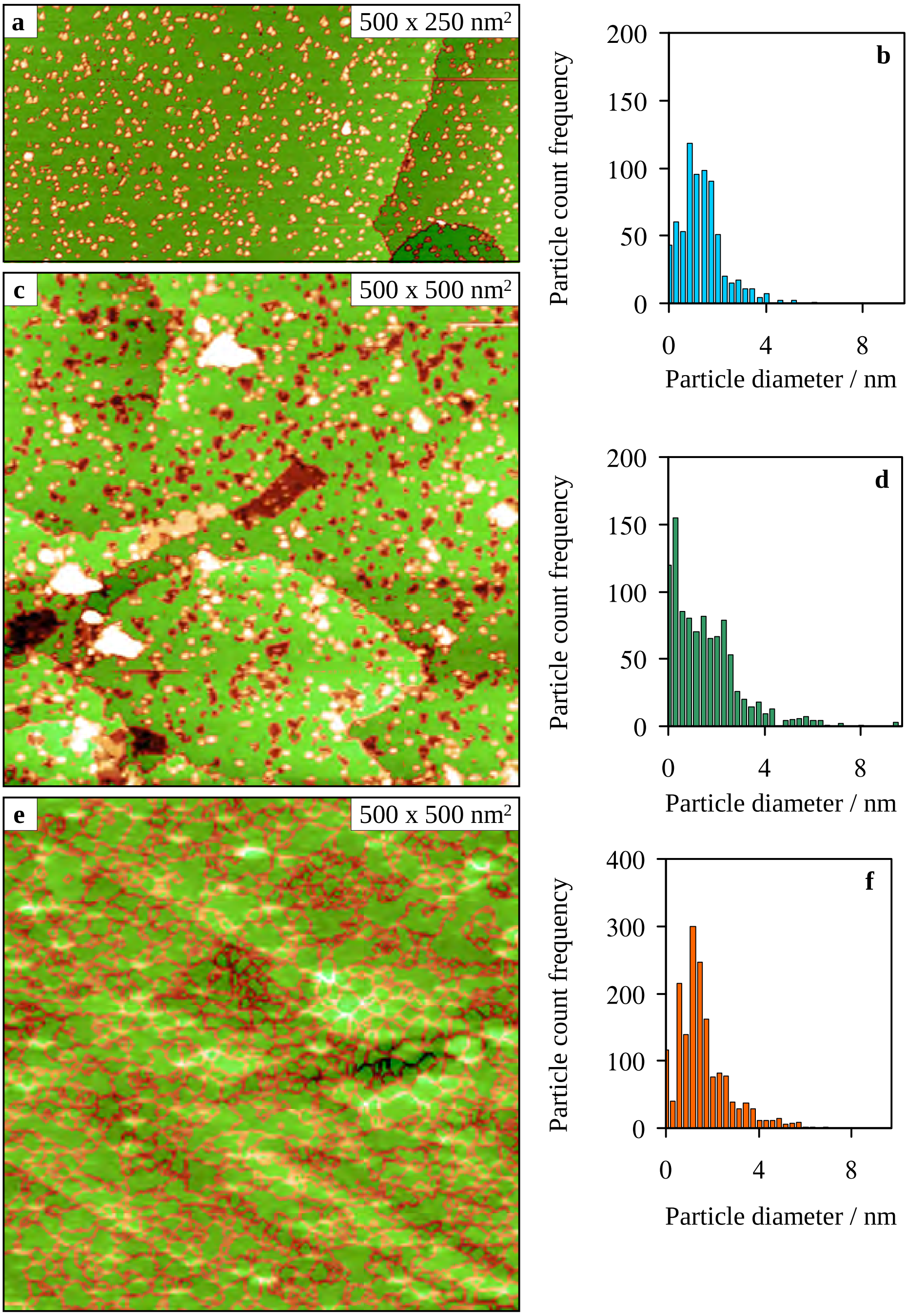

Figure 23. The modelled *situ* STM images (a), (c) and (e) and corresponding particle size distribution plots (b), (d) and (f) for Bi(111) | EMImBF$_4$ interface at negative potential: before dissolution step at $E = -1.0$ V (a), after a slight dissolution step up to $E = -0.2$ V (c), and after a long lasting anodic dissolution step up to $E = 0.0$ V (e).

At $E = 0.0$ V, the non specific roughness of entire surface Bi(111) electrode quickly increased and many more particles were modelled with the GD calculations method (Fig. 23e and 23f).

The adsorption of iodide anions at a Bi(111) | EMImBF$_4$ + EMImI interface has been visualised in Fig. 24b, and the corresponding fitting net has been drawn in Fig. 24a. The iodide anions can be estimated and well correlated with the data collected from Fourier filtered *in situ* STM topographic images. The average effective size of adsorbed iodide anions is 0.45 ± 0.05 nm. The count frequency of the adsorbed ions at Bi(111) | RTIL interface can further be correlated with the Gibbs adsorption and surface coverage values, but for shortness is not discussed in this work.

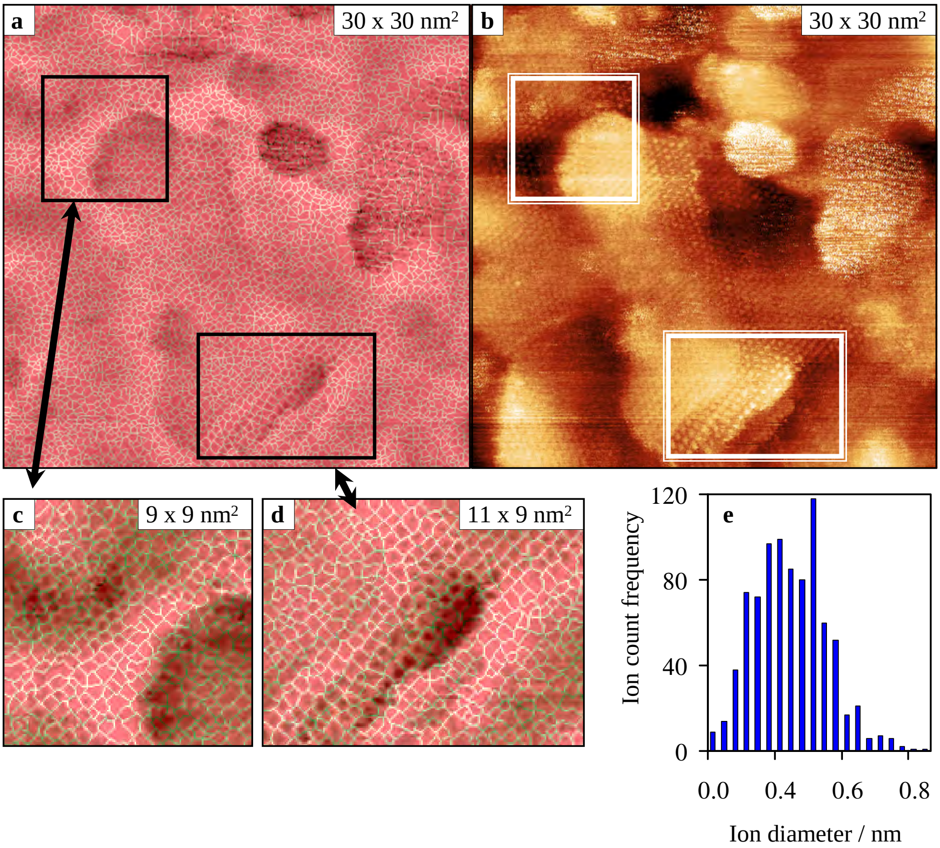

Figure 24. *In situ* STM image for Bi(111) | EMImBF$_4$ + 1wt% EMImI interface under negative electrode potential (b), the modelled image of adsorbed iodide anion at Bi(111) surface (a), (c) and (d), and ion count frequency *vs.* ion diameter distribution plot (e), respectively.

V SUMMARY

The interfacial structure of Bi(111) electrode in 1-ethyl-3-methylimidazolium tetrafluoroborate ($EMImBF_4$), 1-butyl-4-methylpyridinium tetrafluoroborate ($BMPyBF_4$) and in a mixture of EMImBF4 + 1wt% 1-ethyl-3methylimidazolium iodide (EMImI) has been analysed using *in situ* scanning tunnelling microscopy (STM), cyclic voltammetry (CV) and electrochemical impedance spectroscopy (EIS) methods. Influence of electrode potential (*E*) and *in situ* STM scanning conditions on the structure of Bi(111) | ionic liquid interface has been demonstrated.

The regions of ideal polarisability for each interface have been established by CV method and compared to the *in situ* STM and EIS data. The Bi(111) | $EMImBF_4$, Bi(111) | $BMPyBF_4$ and Bi(111) | $EMImBF_4$ + EMImI interfaces are ideally polarisable from −1.2 V to 0.0 V, from −1.2 V to −0.3 V, and from −1.0 V to 0.0 V (*vs.* Ag | AgCl reference electrode in the same ionic liquid), respectively.

Slow electrical double layer (EDL) formation kinetics limited by the finite-length mass transfer and adsorption steps of $EMImBF_4$ and $BMPyBF_4$ onto the Bi(111) surface has been analysed by EIS method. The higher series capacitance, double layer capacitance and adsorption capacitance values, calculated for the Bi(111) | $EMImBF_4$ interface using non-linear least squares fitting of impedance data, compared to Bi(111) | $BMPyBF_4$ interface have been explained by the lower molar volume, higher dielectric constant and lower thickness of EDL formed.

All three interfaces studied under *in situ* measurement conditions were stable under negative potential conditions (up to $E = -1.2$ V) for many hours like in aqueous solutions. The values of root mean square (RMS) roughness calculated for the interfaces under study are comparable to the Bi(111) | aqueous solution interface. At more positive potentials applied ($E > -0.4$ V), the anisotropic dissolution of Bi(111) surface and redeposition of Bi clusters were found to occur at Bi(111) | $EMImBF_4$ and Bi(111) | $BMPyBF_4$ interfaces, causing the increase in the corresponding RMS values up to a few times.

No adsorption superstructures were found on the Bi(111) | $EMImBF_4$ interface during potential cycling within all potential regions studied by the *in situ* STM method. An atomic resolution was achieved for all three interfaces at the potentials more negative than −1.0 V. The average distance 3.5 ± 0.2 Å between the electron density localisation points (the atoms) for a clean Bi(111) plane

has been established. For Bi(111) | $EMImBF_4$ + EMImI interface at $-0.8\text{ V} \le E \le -0.3\text{ V}$, the average distance between specifically adsorbed I^- anions was 5.2 ± 0.2 Å. The distances obtained are in a good agreement with literature data. The adsorption–desorption processes of iodide anions seem to be reversible and the formed 2D-superstructure probably protects the Bi(111) surface from a quick irreversible oxidation at $E \le -0.3$ V. The 2D-superstructures have been established with the *in situ* STM method at

Bi(111) | $BMPyBF_4$ interface at $-1.2\ V \leq E \leq -0.8\ V$, and for Bi(111) | $EMImBF_4$ + EMImI interface at $-0.8\ V \leq E \leq -0.3\ V$, which is in a good agreement with the EIS data.

Based on CV, EIS and mainly on *in situ* STM data, it was established, that the electrical field (electrode potential) induced surface processes, being well known for Au(*hkl*) electrodes, do not occur on Bi(111) electrodes.

Grain analysis method has been applied for the Bi(111) | ionic liquid interfaces and for the modelling of the solid oxide fuel cell electrodes. The anisotropic and universal dissolution and deposition of bismuth from $EMImBF_4$, and specific adsorption of iodide anions from $EMImBF_4$ + EMImI mixture onto Bi(111) surface, as a result of potential cycling, have been modelled and discussed. The corresponding particle sizes and their distributions, depending on the anodic dissolution conditions of the Bi(111) electrode surface, have been calculated.

REFERENCES

[1] E. Lust, in:, A.J. Bard, M. Stratmann, E. Gileadi, M. Urbakh (Eds.), Encycl. Electrochem. Thermodyn. Electrified Interfaces, Wiley VCH (2002) 188–225.

[2] L.I. Daikhin, A.A. Kornyshev, M. Urbakh, Phys. Rev. E 53 (1996) 6192–6199.

[3] S. Kallip, H. Kasuk, V. Grozovski, P. Möller, E. Lust, Electrochim. Acta 53 (2008) 4035–4045.

[4] S. Kallip, E. Lust, Electrochem. Commun. 7 (2005) 863–867.

[5] V. Grozovski, V. Ivaništšev, H. Kasuk, T. Romann, E. Lust, Electrochim. Acta 120 (2014) 86–95.

[6] V. Grozovski, H. Kasuk, S. Kallip, E. Lust, J. Electroanal. Chem. 712 (2014) 103−112.

[7] V. Grozovski, S. Kallip, E. Lust, Surf. Sci. 613 (2013) 108–113.

[8] L. Siinor, J. Poom, C. Siimenson, K. Lust, E. Lust, J. Electroanal. Chem. 719 (2014) 133–137.

[9] E. Härk, K. Lust, A. Jänes, E. Lust, J. Solid State Electrochem. 13 (2009) 745–754.

[10] E.P. K. Lust, 36 (2000) 1257–1262.

[11] M. Armand, F. Endres, D.R. MacFarlane, H. Ohno, B. Scrosati, Nat. Mater. 8 (2009) 621–629.

[12] S. Baldelli, J. Phys. Chem. B 109 (2005) 13049–13051.

[13] M.V. Fedorov, A.A. Kornyshev, Electrochim. Acta 53 (2008) 6835–6740.

[14] M. Drüschler, N. Borisenko, J. Wallauer, C. Winter, B. Huber, F. Endres, B. Roling, Phys. Chem. Chem. Phys. 14 (2012) 5090–5099.

[15] H. Kurig, A. Jänes, E. Lust, J. Electrochem. Soc. 157 (2010) A272–A279.

[16] H. Kurig, M. Vestli, A. Jaenes, E. Lust, Electrochem. Solid State Lett. 14 (2011) A120–A122.

[17] R. Palm, H. Kurig, K. Tõnurist, A. Jänes, E. Lust, Electrochem. Commun. 22 (2012) 203–206.

[18] H. Kurig, M. Vestli, K. Tõnurist, A. Jänes, E. Lust, J. Electrochem. Soc. 159 (2012) A944–A951.

[19] R. Palm, H. Kurig, K. Tõnurist, A. Jaenes, E. Lust, Electrochim. Acta 85 (2012) 139–144.

[20] A. Jänes, E. Lust, Electrochem. Commun. 7 (2005) 510–514.

[21] M. Arulepp, J. Leis, M. Lätt, F. Miller, K. Rumma, E. Lust, A.F. Burke, J. Power Sources 162 (2006) 1460–1466.

[22] K. Fic, G. Lota, M. Meller, E. Frackowiak, Energy Environ. Sci. 5 (2012) 5842−5850.

[23] Q. Gao, L. Demarconnay, E. Raymundo-Piñero, F. Béguin, Energy Environ. Sci. 5 (2012) 9611–9617.

[24] J. Eskusson, A. Jänes, A. Kikas, L. Matisen, E. Lust, J. Power Sources 196 (2011) 4109–4116.

[25] L. Siinor, K. Lust, E. Lust, J. Electrochem. Soc. 157 (2010) F83–F87.

[26] L. Siinor, K. Lust, E. Lust, Electrochem. Commun. 12 (2010) 1058–1061.

[27] A.A. Kornyshev, J. Phys. Chem. B 111 (2007) 5545–5557.

[28] M.Z. Bazant, B.D. Storey, A.A. Kornyshev, Phys. Rev. Lett. 106 (2011) 046102−4.

[29] Y. Lauw, M.D. Horne, T. Rodopoulos, A. Nelson, F.A.M. Leermakers, J. Phys. Chem. B 114 (2010) 11149–11154.

[30] D. Jiang, D. Meng, J. Wu, Chem. Phys. Lett. 504 (2011) 153–158.
[31] D. Henderson, S. Lamperski, J. Chem. Eng. Data 56 (2011) 1204–1208.
[32] M. Biso, M. Mastragostino, M. Montanino, S. Passerini, F. Soavi, Electrochim. Acta 53 (2008) 7967–7971.
[33] M. Trulsson, J. Algotsson, J. Forsman, C.E. Woodward, J. Phys. Chem. Lett. 1 (2010) 1191–1195.
[34] M. Gnahm, T. Pajkossy, D.M. Kolb, Electrochim. Acta 55 (2010) 6212–6217.
[35] M. Schweizer, M. Manolova, D.M. Kolb, Surf. Sci. 602 (2008) 3303–3307.
[36] K. Lust, E. Lust, J. Electroanal. Chem. 552 (2003) 129–139.
[37] L. Siinor, C. Siimenson, V. Ivaništšev, K. Lust, E. Lust, J. Electroanal. Chem. 668 (2012) 30–36.
[38] R. Costa, C.M. Pereira, F. Silva, Phys. Chem. Chem. Phys. 12 (2010) 11125−11132.
[39] V. Lockett, R. Sedev, J. Ralston, M. Horne, T. Rodopoulos, J. Phys. Chem. C 112 (2008) 7486–7495.
[40] E. Anderson, V. Grozovski, L. Siinor, C. Siimenson, V. Ivaništšev, K. Lust, S. Kallip, E. Lust, J. Electroanal. Chem. 709 (2013) 46–56.
[41] Y.-Z. Su, Y.-C. Fu, J.-W. Yan, Z.-B. Chen, B.-W. Mao, Angew. Chem. Int. Ed. 48 (2009) 5148–5151.
[42] Y.-Z. Su, J.-W. Yan, M.-G. Li, Z.-X. Xie, B.-W. Mao, Z.-Q. Tian, Z. Phys. Chem.-Int. J. Res. 226 (2012) 979–994.
[43] X. Zhang, Y.-X. Zhong, J.-W. Yan, Y.-Z. Su, M. Zhang, B.-W. Mao, Chem. Commun. 48 (2012) 582–584.
[44] Y.Z. Su, Y.C. Fu, Y.M. Wei, J.W. Yan, B.W. Mao, Chem. Phys. Chem. 11 (2010) 2764–2778.
[45] T. Tooming, T. Thomberg, L. Siinor, K. Tõnurist, A. Jänes, E. Lust, J. Electrochem. Soc. 161 (2014) A222–A227.
[46] S. Trasatti, E. Lust, in:, White, R.E., Bockris, J.O'M., Conway, B.E. (Eds.), Mod. Asp. Electrochem., Kluwer Academic / Plenum Publishers, New York (1999) 1−193.
[47] V.D. Jović, R. Parsons, B.M. Jovic, J. Electroanal. Chem. 339 (1992) 327–337.
[48] T. Pajkossy, T. Wandlowski, D.M. Kolb, J. Electroanal. Chem. 414 (1996) 209−220.
[49] E. Lust, A. Jänes, K. Lust, R. Pullerits, J. Electroanal. Chem. 431 (1997) 183–201.
[50] E. Lust, S. Kallip, P. Möller, A. Jänes, V. Sammelselg, P. Miidla, M. Väärtnõu, K. Lust, J. Electrochem. Soc. 150 (2003) E175–E184.
[51] D.M. Kolb, R. Ullmann, J.C. Ziegler, Electrochim. Acta 43 (1998) 2751–2760.
[52] T. Wandlowski, in: A.J. Bard, M. Stratmann (Eds.), Encycl. Electrochem., Wiley VCH, Weinheim (2002) 383–471.
[53] H. Kasuk, G. Nurk, K. Lust, E. Lust, J. Electroanal. Chem. 550–551 (2003) 13–31.
[54] H. Kasuk, G. Nurk, K. Lust, E. Lust, J. Electroanal. Chem. 580 (2005) 128–134.
[55] E. Lust, A. Jänes, V. Sammelselg, P. Miidla, K. Lust, Electrochim. Acta 44 (1998) 373–383.
[56] L. Siinor, C. Siimenson, K. Lust, E. Lust, Electrochem. Commun. 35 (2013) 5–7.
[57] A.A. Kornyshev, I. Vilfan, Electrochim. Acta 40 (1995) 109–127.
[58] K. Kirchner, T. Kirchner, V. Ivaništšev, M.V. Fedorov, Electrochim. Acta 110 (2013) 762–771.
[59] J. Kruusma, L. Nei, J.L. Hardcastle, R.G. Compton, E. Lust, H. Keis, Electroanalysis 16 (2004) 399–403.

[60] J. Kruusma, C.E. Banks, L. Nei, R.G. Compton, Anal. Chim. Acta 510 (2004) 85−90.

[61] J. Wang, Anal. Chem. 54 (1982) 221–223.

[62] E. Anderson, V. Grozovski, L. Siinor, C. Siimenson, E. Lust, Electrochem. Commun. 46 (2014) 18–21.

[63] A.J. Bard, L.R. Faulkner, Electrochemical Methods: Fundamentals and Applications, 2nd Edition, Wiley (2001).

[64] A. Noda, M. Watanabe, Electrochim. Acta 45 (2000) 1265–1270.

[65] S. Kallip, P. Laukkanen, A. Jänes, V. Sammelselg, J. Väyrynen, P. Miidla, E. Lust, Surf. Sci. 532–535 (2003) 1121–1126.

[66] P. Pikma, V. Grozovski, H. Kasuk, E. Lust, Surf. Sci. 628 (2014) 86–91.

[67] P. Agarwal, M.E. Orazem, L.H. García-Rubio, J. Electrochem. Soc. 139 (1992) 1917–1927.

[68] B.A. Boukamp, Solid State Ionics 20 (1986) 31–44.

[69] V.F. Lvovich, Impedance Spectroscopy: Applications to Electrochemical and Dielectric Phenomena, Wiley (2012).

[70] G. Binnig and H. Rohrer, Helv. Phys. Acta 55 (1982) 726−735.

[71] G. Binnig, C. F. Quate, and Ch. Gerber, Phys. Rev. Lett. 56 (1986) 930–933.

[72] P. Hermann, A. Hermelink, V. Lausch, G. Holland, L. Möller, N. Bannert, D. Naumann, Analyst 136 (2011) 1148–1152.

[73] G. Schitter, M.J. Rost, Mater. Today 11, Supplement (2008) 40–48.

[74] V. Ivaništšev, R.R. Nazmutdinov, E. Lust, Surf. Sci. 604 (2010) 1919–1927.

[75] D. Nečas, P. Klapetek, Cent. Eur. J. Phys. 10 (2012) 181–188.

[76] I. Horcas, R. Fernández, J.M. Gómez-Rodríguez, J. Colchero, J. Gómez-Herrero, A.M. Baro, Rev. Sci. Instrum. 78 (2007) 013705.

[77] J. Zhang, A.C. Welinder, Q. Chi, J. Ulstrup, Phys. Chem. Chem. Phys. 13 (2011) 5526–5545.

[78] G.H. Lane, Electrochim. Acta 83 (2012) 513–528.

[79] T. Romann, O. Oll, P. Pikma, E. Lust, Electrochem. Commun. 23 (2012) 118–121.

[80] T. Romann, O. Oll, P. Pikma, H. Tamme, E. Lust, Electrochim. Acta 125 (2014) 183–190.

[81] D.M. Kolb, Surf. Sci. 500 (2002) 722–740.

[82] Y. Su, J. Yan, M. Li, M. Zhang, B. Mao, J. Phys. Chem. C 117 (2013) 205–212.

[83] L.G. Lin, Y. Wang, J.W. Yan, Y.Z. Yuan, J. Xiang, B.W. Mao, Electrochem. Commun. 5 (2003) 995–999.

[84] Y.-Z. Su, Y.-C. Fu, J.-W. Yan, Z.-B. Chen, B.-W. Mao, Angew. Chem. 121 (2009) 5250–5253.

[85] F. Endres, N. Borisenko, S.Z.E. Abedin, R. Hayes, R. Atkin, Faraday Discuss. 154 (2012) 221–233.

[86] C. Müller, S. Vesztergom, T. Pajkossy, T. Jacob, J. Electroanal. Chem. 737 (2015) 218–225.

[87] H. Li, F. Endres, R. Atkin, Phys. Chem. Chem. Phys. 15 (2013) 14624–14633.

[88] M. Gnahm, C. Müller, R. Répánszki, T. Pajkossy, D.M. Kolb, Phys. Chem. Chem. Phys. 13 (2011) 11627–11633.

[89] E. Barsoukov, J.R. Macdonald, Impedance Spectroscopy: Theory, Experiment, and Applications, Wiley, John & Sons, Incorporated (2005).

[90] M.E. Orazem, N. Pébère, B. Tribollet, J. Electrochem. Soc. 153 (2006) B129.

[91] R. Parsons, Trans. Faraday Soc. 51 (1955) 1518–1529.

[92] R. de Levie, J. Electrochem. Soc. 118 (1971) 185C–192C.
[93] L. Falciola, P.R. Mussini, S. Trasatti, L.M. Doubova, J. Electroanal. Chem. 593 (2006) 185–193.
[94] E. Lust, A. Jänes, K. Lust, J. Electroanal. Chem. 449 (1998) 153–163.
[95] A.N. Frumkin, V.I. Melik-Gaikazyan, Dokl. Akad. Nauk. SSSR 77 (1951) 855.
[96] B.B. Damaskin, O.A. Petrii, V.V. Batrakov, Adsorption of Organic Compounds on Electrodes, Plenum Press, New York (1971).
[97] J. Wang, J. Electroanal. Chem. Interfacial Electrochem. 140 (1982) 141–146.
[98] H. Sun, B. Qiao, D. Zhang, C. Liu, J. Phys. Chem. A 114 (2010) 3990–3996.
[99] D. Bedrov, O. Borodin, Z. Li, G.D. Smith, J. Phys. Chem. B 114 (2010) 4984−4997.
[100] S. Amokrane, V. Russier, J.P. Badiali, Surf. Sci. 210 (1989) 251–270.
[101] T. Jacobsen, K. West, Electrochim. Acta 40 (1995) 255–262.
[102] J. Kłos, S. Lamperski, J. Phys. Chem. C 114 (2010) 13329–13333.
[103] I. Bandrés, D.F. Montaño, I. Gascón, P. Cea, C. Lafuente, Electrochim. Acta 55 (2010) 2252–2257.
[104] W.B. Pearson, The Crystal Chemistry and Physics of Metals and Alloys, Wiley-Interscience (1972).
[105] A. Kelli, G.W. Growes, in:, Crystallogr. Cryst. Defects, Longman, London (1970) 129.
[106] B. Uhl, F. Buchner, D. Alwast, N. Wagner, R.J. Behm, Beilstein J. Nanotechnol. 4 (2013) 903–918.
[107] S.A. Kislenko, I.S. Samoylov, R.H. Amirov, Phys. Chem. Chem. Phys. 11 (2009) 5584–5590.
[108] G. Feng, J. Huang, B.G. Sumpter, V. Meunier, R. Qiao, Phys. Chem. Chem. Phys. 13 (2011) 14723–14734.
[109] J. Vatamanu, O. Borodin, G.D. Smith, J. Am. Chem. Soc. 132 (2010) 14825−14833.
[110] H. Tokuda, S. Tsuzuki, M.A.B.H. Susan, K. Hayamizu, M. Watanabe, J. Phys. Chem. B 110 (2006) 19593–19600.
[111] D.A. Turton, J. Hunger, A. Stoppa, G. Hefter, A. Thoman, M. Walther, R. Buchner, K. Wynne, J. Am. Chem. Soc. 131 (2009) 11140–11146.
[112] A.P. Abbott, Eur. J. Chem. Phys. Phys. Chem. 6 (2005) 2502–2505.
[113] H. Weingärtner, P. Sasisanker, C. Daguenet, P.J. Dyson, I. Krossing, J.M. Slattery, T. Schubert, J. Phys. Chem. B 111 (2007) 4775–4780.
[114] V. Lockett, M. Horne, R. Sedev, T. Rodopoulos, J. Ralston, Phys. Chem. Chem. Phys. 12 (2010) 12499–12512.
[115] G. Nurk, H. Kasuk, K. Lust, A. Jänes, E. Lust, J. Electroanal. Chem. 553 (2003) 1−19.
[116] X. Hu, C. Chen, S. Tang, W. Wang, J. Yan, B. Mao, Sci. Bull. 60 (2015) 877–883.
[117] B. Obliers, P. Broekmann, K. Wandelt, J. Electroanal. Chem. 554–555 (2003) 183–189.
[118] M. Dietterle, T. Will, D.M. Kolb, Surf. Sci. 327 (1995) L495–L500.
[119] R. Atkin, S.Z. El Abedin, R. Hayes, L.H.S. Gasparotto, N. Borisenko, F. Endres, J. Phys. Chem. C 113 (2009) 13266–13272.
[120] N. Borisenko, S.Z. El Abedin, F. Endres, Chem. Phys. Chem. 13 (2012) 1736−1742.
[121] K. Laes, H. Kasuk, G. Nurk, M. Väärtnõu, K. Lust, A. Jänes, E. Lust, J. Electroanal. Chem. 569 (2004) 241–256.

[122] M.A. Vorotyntsev, A.A. Kornyshev, Elektrokhim. 20 (1984) 3–47.
[123 E. Lust, R. Küngas, I. Kivi, H. Kurig, P. Möller, E. Anderson, K. Lust, K. Tamm, A. Samussenko, G. Nurk, Electrochim. Acta 55 (2010) 7669–7678.

SUMMARY IN ESTONIAN

Bi(111) elektroodi ja ioonse vedeliku vahelise piirpinna struktuuri uuringud *in situ* skaneeriva tunnelmikroskoopia meetodil

Käeslevas töös uuriti Bi(111) elektroodi ja 1-etüül-3-metüülimidazolium-tetrafluoroboraadi ($EMImBF_4$), 1-butüül-4-metüülpüridinium-tetrafluoroboraadi ($BMPyBF_4$) ja $EMImBF_4$ + 1-etüül-3-metüülimidazolium-iodiidi vahelisi piirpindasid, kasutades selleks *in situ* skaneeriva tunnelmikroskoopia (STM), tsüklilise voltamperomeetria (CV) ja elektrokeemilise impedantsi (EIS) meetodeid. Uuriti elektroodi potentsiaali ja *in situ* STM skaneerimisparameetrite mõju Bi(111) elektroodi ja ioonse vedeliku vahelisele piirpinna struktuurile.

CV meetodil mõõdeti ideaalse polariseeritavuse alad ja neid tulemusi analüüsiti ning võrreldi *in situ* STM ja EIS mõõtmistest saadud tulemustega. Bi(111) | $EMImBF_4$, Bi(111) | $BMPyBF_4$ ja Bi(111) | $EMImBF_4$ + EMImI piirpinnad on ideaalselt polariseeritavad vastavalt potentsiaalide vahemikus: $-1.2\ V \leq E \leq 0.0\ V$, $-1.2\ V \leq E \leq -0.3\ V$ ja $-1.0\ V \leq E \leq 0.0\ V$ (Ag | AgCl võrdluselektroodi suhtes samas ioonses vedelikus).

EIS mõõtmistulemuste analüüsist selgus, et Bi(111) | $EMImBF_4$ ning Bi(111) | $BMPyBF_4$ piirpindade korral limiteerivad vastavate elektriliste kaksikkihtide (EKK) moodustumise kiirust Bi(111) elektroodil peamiselt aeglase massiülekande ja adsorptsiooni staadiumid.

EIS andmed modelleeriti erinevate ekvivalentskeemide abil (rakendades vähimruutude meetodit). Leiti, et järjestik-, EKK - ja adsorptsioonilise mahtuvuse väärtused on suuremad Bi(111) | $EMImBF_4$ piirpinna korral, võrreldes Bi(111) | $BMPyBF_4$ piirpinnaga. Saadud tulemustest järeldatakse, et Bi(111) | $EMImBF_4$ piirpinnal on vastava ioonse vedeliku molaarruumala väiksem, dielektriline konstant kõrgem ja moodustunud EKK viskoossus on madalam kui Bi(111) | $BMPyBF_4$ piirpinna korral.

Mõõdetud tulemuste analüüsi käigus leiti, et kõik kolm uuritud piirpinda on negatiivse potentsiaali tingimustes (kuni $E = -1.2$ V) ajaliselt väga stabiilsed paljude tundide jooksul sarnaselt Bi(111) elektroodi stabiilsusega vesilahustes negatiivsetel potentsiaalidel. Bi(111) elektroodi korral arvutatud ruutkeskmistatud (RMS) taredused ioonse vedeliku keskkonnas on võrreldavad vastavate RMS karedustega vesilahustes.

Leiti, et sarnaselt vesilahustele kasvab ioonse vedeliku keskkonnas RMS karedus kordades, kui rakendada positiivsemaid potentsiaale ($E > -0.4$ V), mis põhjustavad sileda Bi(111) pinna anisotroopset lahustumist ja vismuti klastrite sadenemist üle kogu Bi(111) | $EMImBF_4$ ja Bi(111) | $BMPyBF_4$ piirpinna.

In situ STM meetodil leiti potentsiaali tsükleerimise käigus Bi(111) pinnalt nii $BMPyBF_4$ kui ka $EMImBF_4$ + EMImI segu korral 2D-superstruktuurid. Bi(111) | $EMImBF_4$ piirpinnal superstruktuure ei täheldatud. Kõigi kolme piirpinna korral saavutati atomaarne lahutus *in situ* STM meetodil ja aatomite vahekauguseks puhtal Bi(111) tahul mõõdeti 3.5 ± 0.2 Å.

Bi(111) | $EMImBF_4$ + EMImI piirpinna korral mõõdeti adsorbeerunud jodiidi anioonide vaheliseks kauguseks 5.2 ± 0.2 Å (potentsiaalide vahemikus −0.8 V kuni−0.3 V). Saadud tulemused on heas kooskõlas kirjandusest leitavate andmetega. *In situ* STM meetodil demonstreeritud 2D-superstruktuurid on heas kooskõlas andmetega, mis saadi EIS meetodiga; vastavalt Bi(111) | $BMPyBF_4$ piirpinnal (alates −1.2 V kuni −0.8 V) ja Bi(111) | $EMImBF_4$ + EMImI segu piirpinnal (alates $E = -1.2$ V kuni $E = -0.3$ V).

Tuginedes CV, EIS ja STM andmetele leiti, et erinevalt Au(*hkl*) elektroodist ei toimu Bi(111) elektroodil elektrilise välja muutuse poolt indutseeritud pinna rekonstrueerimise protsesse.

Bi(111) | ioonne vedelik piirpinna kirjeldamiseks kasutati terade suuruse modelleerimise meetodit. Kirjeldati vismuti pinna anisotroopse lahustumise ja tagasisademenmise protsesse. Lisaks modelleeriti Bi(111) | $EMImBF_4$ + EMImI segust adsorbeerunud jodiidioonide paiknemist Bi(111) elektroodil. Arvutati osakeste keskmised suurused ja nende suuruste jaotused. Terade suuruste modelleerimise meetodit rakendati ka tahkeoksiidse kütuseelemendi elektroodide pinnastruktuuri kirjeldamiseks.

AKNOWLEDGEMENTS

This study was supported by the Estonian target research project: IUT14013I, ESF Grant no. 8786, the Estonian Centre of Excellence in Science Project TK117T "High-Technology Materials for Sustainable Development", the Estonian Energy Technology Program project: SLOKT10209T, the Materials Technology project SLOKT12180T, and by the graduate school “Functional materials and technologies” receiving funding from the European Social Fund under the project 1.2.0401.09-0079 in Estonia.

I would like to express my thankfulness to my supervisor Professor Enn Lust for persistent assistance and thorough scientific guidance during these years of collaboration.

I would like to thank all my colleagues, especially Vitali Grozovski, for a fruitful cooperation in the measurements.

I would like to thank my parents and friends for the supportive environment.

CURRICULUM VITAE

Name: Erik Anderson
Date of birth: 20. August 1985
Citizenship: Estonian
Address: Kaunase St. 47-29, 50706, Tartumaa, Tartu, Estonia
Telephone: +372 5289850
E-mail: erik.anderson@ut.ee

Current position: University of Tartu, Institute of Chemistry, Chemist (0.5) and PhD student

Education:

2010–2015	University of Tartu, Institute of Chemistry, PhD student
2008–2010	University of Tartu – Master's degree in chemistry
2004–2008	University of Tartu – Bachelor degree in chemistry
1994–2004	Tartu Kivilinna Gymnaasium – basic and secondary education

Language skills:

Estonian	native language
English	very good in speech and writing
German	average in speech and writing

Professional career:

2007–...	University of Tartu, Institute of Chemistry, Chemist

Research and development work

Main field of research:
Natural sciences and engineering, Chemistry and chemical technology, Electrochemistry, Solid oxide fuel cell, Processes at liquid | solid interface, Ionic liquid, Metal single crystals, Scanning probe microscopy, Scanning electron microscopy.

A list of publications:

1. Lust, E.; Kivi, I.; Küngas, R.; Tamm, K.; Möller, P.; Samussenko, A.; Anderson, E.; Kurig, H.; Nurk, G. (2009). Medium temperature solid oxide fuel cells based on the micro-meso-macro-porous cathodes and anodes. ECS Transactions, 25(2), 325–333.

2. Lust, E.; Küngas, R.; Kivi, I.; Kurig, H.; Möller, P.; Anderson, E.; Lust, K.; Tamm, K.; Samusshenko, A.; Nurk, G. (2010). Electrochemical and gas phase parameters of cathodes for intermediate temperature solid oxide fuel cells. Electrochimica Acta, 55(26), 7669–7678.

3. Kivi, Indrek; Anderson, Erik; Möller, Priit; Nurk, Gunnar; Lust, Enn (2012). Influence of Microstructural Parameters of LSC Cathodes on the Oxygen Reduction Reaction Parameters. Journal of the Electrochemical Society, 159(11), F743–F750.

4. Tamm, K.; Kivi, I.; Anderson, E.; Trikkel, A.; Möller, P.; Nurk, G.; Lust, E. (2012). Influence of Graphite Pore Forming Agents on the Structural and Electrochemical Properties of Porous Ni-CGO Anode. Journal of the Electrochemical Society, 159(12), F849–F857.

5. Vestli, M.; Maide, M.; Anderson, E.; Nurk, G.; Lust, E. (2013). Preparation of $Ce_{0.9}Sm_{0.1-x}Tb_{xO2-\delta}$ Films by Using Ultrasonic Spray Pyrolysis.

6. Anderson, E.; Grozovski, V.; Siinor, L.; Siimenson, C.; Ivaništšev, V.; Lust, K.; Kallip, S.; Lust, E. (2013). Influence of the electrode potential and *in situ* STM scanning conditions on the phase boundary structure of the single crystal Bi(111) | 1-butyl-4-methylpyridinium tetrafluoroborate interface. Journal of Electroanalytical Chemistry, 709, 45–56.

7. Anderson, E.; Grozovski, V.; Siinor, L., Siimenson, C.; Lust, E. (2014). *In situ* STM studies of Bi(111) | 1-ethyl-3-methylimidazolium tetrafluoroborate + 1-ethyl-3-methylimidazolium iodide interface. Electrochemistry Communications, 46, 18–21.

Participation in international conferences:

Anderson, E.; Grozovski, V.; Siinor, L.; Siimenson, C.; Ivaništšev, V.; Lust, K.; Kallip, S.; Lust, E. (2013). Influence of electrode potential and *in situ* STM scanning conditions on the phase boundary structure of single crystal Bi(111) | 1-butyl-4-methylpyridinium tetrafluoroborate interface. 223rd ECS Meeting, Toronto, 1–16 May (oral presentation).

A list of projects:

1. The molecular structure and formation cinetics of 2D compact layers on various single crystal metal and carbon electrodes.
2. Processes at modified phase boundaries and development of novel electrochemical power sources and supercapacitors.
3. Efficient production of fuels from biomass.
4. Development of materials and single cells for solid oxide and polymer electrolyte fuel cells, high temperature electrolyzers and supercapacitors.
5. Interfacial faradic charge transfer and adsorption processes at the room temperature ionic liquid electrode interface.
6. Development of 3D structural anodes and cathodes for solid oxide electrolysis and fuel cells.
7. Development of bilayered cathode on ceria based electrolyte for intermediate temperature solid oxide fuel cell.

8. Synthesis, characterisation and application of activated rare-earth compounds in synthetic fuel synthesis reactors and other high-tech devices.
9. Functional Micro/Mesoporous Nanomaterials for Novel Energy Conversion and Storage Systems.

Research grants and scholarships:

01.01.2010–31.08.2015	Grand stipend

III. Teaching work

Information regarding the teaching work carried out at universities:

LOKT.0.2	Electrochemical Methods for Quantitative Analysis, (3 EAP 2009/2010 ja 2010/2011 I semester, lecture 2 academic hours)
LOKT.0.2	Materials Technology (5 EAP, 2011/2012 ja 2012/2013, lecture and practical work, 4 academic hours)

Supervision:

Piret Pikma	Piret Pikma, Master's Degree, 2011, (sup) Enn Lust, Erik Anderson, The characterization of electric double-layer capacitor electrodes applying atomic force microscopy method, University of Tartu, Faculty of Science and Technology, Institute of Chemistry, Tartu University.

ELULOOKIRJELDUS

Nimi: Erik Anderson
Sünniaeg: 20. august 1985
Kodakondsus: Eesti
Aadress: Kaunas pst. 47-29, 50706, Tartumaa, Tartu linn, Eesti
Telefon: +372 5289850
E-post: erik.anderson@ut.ee

Praegune töökoht: Tartu Ülikool, Keemia Instituut, keemik (0.5) ja doktorant

Haridus:

2010–2015	Tartu Ülikool – Doktoriõpe keemias
2008–2010	Tartu Ülikool – Magistrikraad keemias
2004–2008	Tartu Ülikool – Bakalaureusekraad keemias
1994–2004	Tartu Kivilinna Gümnaasium – põhi- ja keskharidus

Keelteoskus:

Eesti keel	emakeel
Inglise keel	väga hea kõnes ja kirjas
Saksa keel	rahuldav kõnes ja kirjas

Teenistuskäik:

2007–...	Tartu Ülikool, Keemia Instituut; keemik

II. Teaduslik ja arendustegevus

Peamised uurimisvaldkonnad:
Loodusteadused ja tehnika, keemia ja keemiatehnika, elektrokeemia, tahkeoksiidne kütuseelement, protsessid vedelik – tahkis piirpinnal, ioonne vedelik, metallide monokristallid, teravikmikroskoopia, skaneeriv elektronmikroskoopia.

Publikatsioonide loetelu:

1. Lust, E.; Kivi, I.; Küngas, R.; Tamm, K.; Möller, P.; Samussenko, A.; Anderson, E.; Kurig, H.; Nurk, G. (2009). Medium temperature solid oxide fuel cells based on the micro-meso-macro-porous cathodes and anodes. ECS Transactions, 25(2), 325–333.

2. Lust, E.; Küngas, R.; Kivi, I.; Kurig, H.; Möller, P.; Anderson, E.; Lust, K.; Tamm, K.; Samusshenko, A.; Nurk, G. (2010). Electrochemical and gas phase parameters of cathodes for intermediate temperature solid oxide fuel cells. Electrochimica Acta, 55(26), 7669–7678.

3. Kivi, Indrek; Anderson, Erik; Möller, Priit; Nurk, Gunnar; Lust, Enn (2012). Influence of Microstructural Parameters of LSC Cathodes on the Oxygen

Reduction Reaction Parameters. Journal of the Electrochemical Society, 159(11), F743–F750.

4. Tamm, K.; Kivi, I.; Anderson, E.; Trikkel, A.; Möller, P.; Nurk, G.; Lust, E. (2012). Influence of Graphite Pore Forming Agents on the Structural and Electrochemical Properties of Porous Ni-CGO Anode. Journal of the Electrochemical Society, 159(12), F849–F857.

5. Vestli, M.; Maide, M.; Anderson, E.; Nurk, G.; Lust, E. (2013). Preparation of $Ce_{0.9}Sm_{0.1-x}Tb_{xO2-\delta}$ Films by Using Ultrasonic Spray Pyrolysis.

6. Anderson, E.; Grozovski, V.; Siinor, L.; Siimenson, C.; Ivaništšev, V.; Lust, K.; Kallip, S.; Lust, E. (2013). Influence of the electrode potential and *in situ* STM scanning conditions on the phase boundary structure of the single crystal Bi(111) | 1-butyl-4-methylpyridinium tetrafluoroborate interface. Journal of Electroanalytical Chemistry, 709, 45–56.

7. Anderson, E.; Grozovski, V.; Siinor, L., Siimenson, C.; Lust, E. (2014). *In situ* STM studies of Bi(111) | 1-ethyl-3-methylimidazolium tetrafluoroborate + 1-ethyl-3-methylimidazolium iodide interface. Electrochemistry Communications, 46, 18–21.

Rahvusvahelistel konverentsidel osalemine:
Anderson, E.; Grozovski, V.; Siinor, L.; Siimenson, C.; Ivaništšev, V.; Lust, K.; Kallip, S.; Lust, E. (2013). Influence of electrode potential and *in situ* STM scanning conditions on the phase boundary structure of single crystal Bi(111) | 1-butyl-4-methylpyridinium tetrafluoroborate interface. 223rd ECS Meeting, Toronto, 12.-16 May (suuline ettekanne).

Projektide loetelu:
1. Kahedimensionaalsete adsorptsioonikihtide struktuur ja moodustumise kineetika erinevatel monokristallilistel metall ja süsinik elektroodidel.
2. Protsessid modifitseeritud piirpindadel ja faasides ning nende rakendused uuetüübilistes energia allikates ning superkondensaatorites.
3. Kütuse efektiivne tootmine biomassist.
4. Tahkeoksiidsete ja madaltemperatuursete kütuseelementide, elektrolüüserite ja superkondensaatorite materjalide ja ühiskrakkude väljatöötamine ja testimine.
5. Faradi laenguülekande ja adsorptsiooni protsessid ioonne vedelik | elektrood piirpinnal.
6. Tahkeoksiidsete elektrolüüserite ja kütuseelementide 3D struktuursete anoodide ja katoodide arendamine.
7. Katoodi vahekihi valmistamine tseeriumil baseeruvale elektrolüüdile keskmistel temperatuuridel töötavas tahkeoksiidkütuseelemendis.

8. Haruldaste muldmetallide ühendite süntees, karakteriseerimine ja kasutamine sünteetilise kütuse sünteesireaktorites ja teistes kõrgtehnoloogilistes seadmetes.
9. Funktsionaalsed mikro/mesopoorsed materjalid kõrgefektiivsete energia muundamise ja salvestamise süsteemides.

Saadud uurimistoetused ja stipendiumid:

01.01.2010–31.08.2015	Grandistipendium

III. Õppetöö

Andmed kõrgkoolis tehtud auditoorse õppetöö kohta:

LOKT.0.2	Elektrokeemilised mõõte- ja analüüsimeetodid, (3 EAP 2009/2010 ja 2010/2011 sügissemestrid, loeng 2 akadeemilist tundi)
LOKT.0.2	Materjalide tehnoloogia (5 EAP, 2011/2012 ja 2012/2013, loeng ja praktikum, 4 akadeemilist tundi)

Juhendamine:

Piret Pikma	Piret Pikma, magistrikraad, 2011, (juh) Enn Lust, Erik Anderson, Elektrilise kaksikkihi kondensaatori elektroodide iseloomustamine aatomjõu mikroskoopia meetodil, Tartu Ülikool, Loodus- ja tehnoloogiateaduskond, Tartu Ülikooli Keemia Instituut.

DISSERTATIONES CHIMICAE UNIVERSITATIS TARTUENSIS

1. **Toomas Tamm.** Quantum-chemical simulation of solvent effects. Tartu, 1993, 110 p.
2. **Peeter Burk.** Theoretical study of gas-phase acid-base equilibria. Tartu, 1994, 96 p.
3. **Victor Lobanov.** Quantitative structure-property relationships in large descriptor spaces. Tartu, 1995, 135 p.
4. **Vahur Mäemets.** The ^{17}O and ^{1}H nuclear magnetic resonance study of H_2O in individual solvents and its charged clusters in aqueous solutions of electrolytes. Tartu, 1997, 140 p.
5. **Andrus Metsala.** Microcanonical rate constant in nonequilibrium distribution of vibrational energy and in restricted intramolecular vibrational energy redistribution on the basis of slater's theory of unimolecular reactions. Tartu, 1997, 150 p.
6. **Uko Maran.** Quantum-mechanical study of potential energy surfaces in different environments. Tartu, 1997, 137 p.
7. **Alar Jänes.** Adsorption of organic compounds on antimony, bismuth and cadmium electrodes. Tartu, 1998, 219 p.
8. **Kaido Tammeveski.** Oxygen electroreduction on thin platinum films and the electrochemical detection of superoxide anion. Tartu, 1998, 139 p.
9. **Ivo Leito.** Studies of Brønsted acid-base equilibria in water and non-aqueous media. Tartu, 1998, 101 p.
10. **Jaan Leis.** Conformational dynamics and equilibria in amides. Tartu, 1998, 131 p.
11. **Toonika Rinken.** The modelling of amperometric biosensors based on oxidoreductases. Tartu, 2000, 108 p.
12. **Dmitri Panov.** Partially solvated Grignard reagents. Tartu, 2000, 64 p.
13. **Kaja Orupõld.** Treatment and analysis of phenolic wastewater with microorganisms. Tartu, 2000, 123 p.
14. **Jüri Ivask.** Ion Chromatographic determination of major anions and cations in polar ice core. Tartu, 2000, 85 p.
15. **Lauri Vares.** Stereoselective Synthesis of Tetrahydrofuran and Tetrahydropyran Derivatives by Use of Asymmetric Horner-Wadsworth-Emmons and Ring Closure Reactions. Tartu, 2000, 184 p.
16. **Martin Lepiku.** Kinetic aspects of dopamine D_2 receptor interactions with specific ligands. Tartu, 2000, 81 p.
17. **Katrin Sak.** Some aspects of ligand specificity of P2Y receptors. Tartu, 2000, 106 p.
18. **Vello Pällin.** The role of solvation in the formation of iotsitch complexes. Tartu, 2001, 95 p.
19. **Katrin Kollist.** Interactions between polycyclic aromatic compounds and humic substances. Tartu, 2001, 93 p.

20. **Ivar Koppel.** Quantum chemical study of acidity of strong and superstrong Brønsted acids. Tartu, 2001, 104 p.
21. **Viljar Pihl.** The study of the substituent and solvent effects on the acidity of OH and CH acids. Tartu, 2001, 132 p.
22. **Natalia Palm.** Specification of the minimum, sufficient and significant set of descriptors for general description of solvent effects. Tartu, 2001, 134 p.
23. **Sulev Sild.** QSPR/QSAR approaches for complex molecular systems. Tartu, 2001, 134 p.
24. **Ruslan Petrukhin.** Industrial applications of the quantitative structure-property relationships. Tartu, 2001, 162 p.
25. **Boris V. Rogovoy.** Synthesis of (benzotriazolyl)carboximidamides and their application in relations with *N*- and *S*-nucleophyles. Tartu, 2002, 84 p.
26. **Koit Herodes.** Solvent effects on UV-vis absorption spectra of some solvatochromic substances in binary solvent mixtures: the preferential solvation model. Tartu, 2002, 102 p.
27. **Anti Perkson.** Synthesis and characterisation of nanostructured carbon. Tartu, 2002, 152 p.
28. **Ivari Kaljurand.** Self-consistent acidity scales of neutral and cationic Brønsted acids in acetonitrile and tetrahydrofuran. Tartu, 2003, 108 p.
29. **Karmen Lust.** Adsorption of anions on bismuth single crystal electrodes. Tartu, 2003, 128 p.
30. **Mare Piirsalu.** Substituent, temperature and solvent effects on the alkaline hydrolysis of substituted phenyl and alkyl esters of benzoic acid. Tartu, 2003, 156 p.
31. **Meeri Sassian.** Reactions of partially solvated Grignard reagents. Tartu, 2003, 78 p.
32. **Tarmo Tamm.** Quantum chemical modelling of polypyrrole. Tartu, 2003. 100 p.
33. **Erik Teinemaa.** The environmental fate of the particulate matter and organic pollutants from an oil shale power plant. Tartu, 2003. 102 p.
34. **Jaana Tammiku-Taul.** Quantum chemical study of the properties of Grignard reagents. Tartu, 2003. 120 p.
35. **Andre Lomaka.** Biomedical applications of predictive computational chemistry. Tartu, 2003. 132 p.
36. **Kostyantyn Kirichenko.** Benzotriazole – Mediated Carbon–Carbon Bond Formation. Tartu, 2003. 132 p.
37. **Gunnar Nurk.** Adsorption kinetics of some organic compounds on bismuth single crystal electrodes. Tartu, 2003, 170 p.
38. **Mati Arulepp.** Electrochemical characteristics of porous carbon materials and electrical double layer capacitors. Tartu, 2003, 196 p.
39. **Dan Cornel Fara.** QSPR modeling of complexation and distribution of organic compounds. Tartu, 2004, 126 p.
40. **Riina Mahlapuu.** Signalling of galanin and amyloid precursor protein through adenylate cyclase. Tartu, 2004, 124 p.

41. **Mihkel Kerikmäe.** Some luminescent materials for dosimetric applications and physical research. Tartu, 2004, 143 p.
42. **Jaanus Kruusma.** Determination of some important trace metal ions in human blood. Tartu, 2004, 115 p.
43. **Urmas Johanson.** Investigations of the electrochemical properties of polypyrrole modified electrodes. Tartu, 2004, 91 p.
44. **Kaido Sillar.** Computational study of the acid sites in zeolite ZSM-5. Tartu, 2004, 80 p.
45. **Aldo Oras.** Kinetic aspects of dATPαS interaction with $P2Y_1$ receptor. Tartu, 2004, 75 p.
46. **Erik Mölder.** Measurement of the oxygen mass transfer through the air-water interface. Tartu, 2005, 73 p.
47. **Thomas Thomberg.** The kinetics of electroreduction of peroxodisulfate anion on cadmium (0001) single crystal electrode. Tartu, 2005, 95 p.
48. **Olavi Loog.** Aspects of condensations of carbonyl compounds and their imine analogues. Tartu, 2005, 83 p.
49. **Siim Salmar.** Effect of ultrasound on ester hydrolysis in aqueous ethanol. Tartu, 2006, 73 p.
50. **Ain Uustare.** Modulation of signal transduction of heptahelical receptors by other receptors and G proteins. Tartu, 2006, 121 p.
51. **Sergei Yurchenko.** Determination of some carcinogenic contaminants in food. Tartu, 2006, 143 p.
52. **Kaido Tämm.** QSPR modeling of some properties of organic compounds. Tartu, 2006, 67 p.
53. **Olga Tšubrik.** New methods in the synthesis of multisubstituted hydrazines. Tartu. 2006, 183 p.
54. **Lilli Sooväli.** Spectrophotometric measurements and their uncertainty in chemical analysis and dissociation constant measurements. Tartu, 2006, 125 p.
55. **Eve Koort.** Uncertainty estimation of potentiometrically measured ph and pK_a values. Tartu, 2006, 139 p.
56. **Sergei Kopanchuk.** Regulation of ligand binding to melanocortin receptor subtypes. Tartu, 2006, 119 p.
57. **Silvar Kallip.** Surface structure of some bismuth and antimony single crystal electrodes. Tartu, 2006, 107 p.
58. **Kristjan Saal.** Surface silanization and its application in biomolecule coupling. Tartu, 2006, 77 p.
59. **Tanel Tätte.** High viscosity $Sn(OBu)_4$ oligomeric concentrates and their applications in technology. Tartu, 2006, 91 p.
60. **Dimitar Atanasov Dobchev**. Robust QSAR methods for the prediction of properties from molecular structure. Tartu, 2006, 118 p.
61. **Hannes Hagu**. Impact of ultrasound on hydrophobic interactions in solutions. Tartu, 2007, 81 p.
62. **Rutha Jäger.** Electroreduction of peroxodisulfate anion on bismuth electrodes. Tartu, 2007, 142 p.

63. **Kaido Viht.** Immobilizable bisubstrate-analogue inhibitors of basophilic protein kinases: development and application in biosensors. Tartu, 2007, 88 p.
64. **Eva-Ingrid Rõõm.** Acid-base equilibria in nonpolar media. Tartu, 2007, 156 p.
65. **Sven Tamp.** DFT study of the cesium cation containing complexes relevant to the cesium cation binding by the humic acids. Tartu, 2007, 102 p.
66. **Jaak Nerut.** Electroreduction of hexacyanoferrate(III) anion on Cadmium (0001) single crystal electrode. Tartu, 2007, 180 p.
67. **Lauri Jalukse.** Measurement uncertainty estimation in amperometric dissolved oxygen concentration measurement. Tartu, 2007, 112 p.
68. **Aime Lust.** Charge state of dopants and ordered clusters formation in CaF_2:Mn and CaF_2:Eu luminophors. Tartu, 2007, 100 p.
69. **Iiris Kahn**. Quantitative Structure-Activity Relationships of environmentally relevant properties. Tartu, 2007, 98 p.
70. **Mari Reinik.** Nitrates, nitrites, N-nitrosamines and polycyclic aromatic hydrocarbons in food: analytical methods, occurrence and dietary intake. Tartu, 2007, 172 p.
71. **Heili Kasuk.** Thermodynamic parameters and adsorption kinetics of organic compounds forming the compact adsorption layer at Bi single crystal electrodes. Tartu, 2007, 212 p.
72. **Erki Enkvist.** Synthesis of adenosine-peptide conjugates for biological applications. Tartu, 2007, 114 p.
73. **Svetoslav Hristov Slavov**. Biomedical applications of the QSAR approach. Tartu, 2007, 146 p.
74. **Eneli Härk.** Electroreduction of complex cations on electrochemically polished Bi(*hkl*) single crystal electrodes. Tartu, 2008, 158 p.
75. **Priit Möller.** Electrochemical characteristics of some cathodes for medium temperature solid oxide fuel cells, synthesized by solid state reaction technique. Tartu, 2008, 90 p.
76. **Signe Viggor.** Impact of biochemical parameters of genetically different pseudomonads at the degradation of phenolic compounds. Tartu, 2008, 122 p.
77. **Ave Sarapuu.** Electrochemical reduction of oxygen on quinone-modified carbon electrodes and on thin films of platinum and gold. Tartu, 2008, 134 p.
78. **Agnes Kütt.** Studies of acid-base equilibria in non-aqueous media. Tartu, 2008, 198 p.
79. **Rouvim Kadis.** Evaluation of measurement uncertainty in analytical chemistry: related concepts and some points of misinterpretation. Tartu, 2008, 118 p.
80. **Valter Reedo.** Elaboration of IVB group metal oxide structures and their possible applications. Tartu, 2008, 98 p.
81. **Aleksei Kuznetsov.** Allosteric effects in reactions catalyzed by the cAMP-dependent protein kinase catalytic subunit. Tartu, 2009, 133 p.

82. **Aleksei Bredihhin.** Use of mono- and polyanions in the synthesis of multisubstituted hydrazine derivatives. Tartu, 2009, 105 p.
83. **Anu Ploom.** Quantitative structure-reactivity analysis in organosilicon chemistry. Tartu, 2009, 99 p.
84. **Argo Vonk.** Determination of adenosine A_{2A}- and dopamine D_1 receptor-specific modulation of adenylate cyclase activity in rat striatum. Tartu, 2009, 129 p.
85. **Indrek Kivi.** Synthesis and electrochemical characterization of porous cathode materials for intermediate temperature solid oxide fuel cells. Tartu, 2009, 177 p.
86. **Jaanus Eskusson.** Synthesis and characterisation of diamond-like carbon thin films prepared by pulsed laser deposition method. Tartu, 2009, 117 p.
87. **Marko Lätt.** Carbide derived microporous carbon and electrical double layer capacitors. Tartu, 2009, 107 p.
88. **Vladimir Stepanov.** Slow conformational changes in dopamine transporter interaction with its ligands. Tartu, 2009, 103 p.
89. **Aleksander Trummal.** Computational Study of Structural and Solvent Effects on Acidities of Some Brønsted Acids. Tartu, 2009, 103 p.
90. **Eerold Vellemäe.** Applications of mischmetal in organic synthesis. Tartu, 2009, 93 p.
91. **Sven Parkel.** Ligand binding to 5-HT_{1A} receptors and its regulation by Mg^{2+} and Mn^{2+}. Tartu, 2010, 99 p.
92. **Signe Vahur.** Expanding the possibilities of ATR-FT-IR spectroscopy in determination of inorganic pigments. Tartu, 2010, 184 p.
93. **Tavo Romann**. Preparation and surface modification of bismuth thin film, porous, and microelectrodes. Tartu, 2010, 155 p.
94. **Nadežda Aleksejeva.** Electrocatalytic reduction of oxygen on carbon nanotube-based nanocomposite materials. Tartu, 2010, 147 p.
95. **Marko Kullapere.** Electrochemical properties of glassy carbon, nickel and gold electrodes modified with aryl groups. Tartu, 2010, 233 p.
96. **Liis Siinor.** Adsorption kinetics of ions at Bi single crystal planes from aqueous electrolyte solutions and room-temperature ionic liquids. Tartu, 2010, 101 p.
97. **Angela Vaasa.** Development of fluorescence-based kinetic and binding assays for characterization of protein kinases and their inhibitors. Tartu 2010, 101 p.
98. **Indrek Tulp.** Multivariate analysis of chemical and biological properties. Tartu 2010, 105 p.
99. **Aare Selberg.** Evaluation of environmental quality in Northern Estonia by the analysis of leachate. Tartu 2010, 117 p.
100. **Darja Lavõgina.** Development of protein kinase inhibitors based on adenosine analogue-oligoarginine conjugates. Tartu 2010, 248 p.
101. **Laura Herm.** Biochemistry of dopamine D_2 receptors and its association with motivated behaviour. Tartu 2010, 156 p.

102. **Terje Raudsepp.** Influence of dopant anions on the electrochemical properties of polypyrrole films. Tartu 2010, 112 p.
103. **Margus Marandi.** Electroformation of Polypyrrole Films: *In-situ* AFM and STM Study. Tartu 2011, 116 p.
104. **Kairi Kivirand.** Diamine oxidase-based biosensors: construction and working principles. Tartu, 2011, 140 p.
105. **Anneli Kruve.** Matrix effects in liquid-chromatography electrospray mass-spectrometry. Tartu, 2011, 156 p.
106. **Gary Urb.** Assessment of environmental impact of oil shale fly ash from PF and CFB combustion. Tartu, 2011, 108 p.
107. **Nikita Oskolkov.** A novel strategy for peptide-mediated cellular delivery and induction of endosomal escape. Tartu, 2011, 106 p.
108. **Dana Martin.** The QSPR/QSAR approach for the prediction of properties of fullerene derivatives. Tartu, 2011, 98 p.
109. **Säde Viirlaid.** Novel glutathione analogues and their antioxidant activity. Tartu, 2011, 106 p.
110. **Ülis Sõukand.** Simultaneous adsorption of Cd^{2+}, Ni^{2+}, and Pb^{2+} on peat. Tartu, 2011, 124 p.
111. ***Lauri Lipping.*** *The acidity of strong and superstrong Brønsted acids, an outreach for the "limits of growth": a quantum chemical study. Tartu, 2011, 124 p.*
112. **Heisi Kurig.** Electrical double-layer capacitors based on ionic liquids as electrolytes. Tartu, 2011, 146 p.
113. **Marje Kasari.** Bisubstrate luminescent probes, optical sensors and affinity adsorbents for measurement of active protein kinases in biological samples. Tartu, 2012, 126 p.
114. **Kalev Takkis.** Virtual screening of chemical databases for bioactive molecules. Tartu, 2012, 122 p.
115. **Ksenija Kisseljova**. Synthesis of aza-β^3-amino acid containing peptides and kinetic study of their phosphorylation by protein kinase A. Tartu, 2012, 104 p.
116. **Riin Rebane.** Advanced method development strategy for derivatization LC/ESI/MS. Tartu, 2012, 184 p.
117. **Vladislav Ivaništšev.** Double layer structure and adsorption kinetics of ions at metal electrodes in room temperature ionic liquids. Tartu, 2012, 128 p.
118. **Irja Helm.** High accuracy gravimetric Winkler method for determination of dissolved oxygen. Tartu, 2012, 139 p.
119. **Karin Kipper.** Fluoroalcohols as Components of LC-ESI-MS Eluents: Usage and Applications. Tartu, 2012, 164 p.
120. **Arno Ratas.** Energy storage and transfer in dosimetric luminescent materials. Tartu, 2012, 163 p.
121. **Reet Reinart-Okugbeni**. Assay systems for characterisation of subtype-selective binding and functional activity of ligands on dopamine receptors. Tartu, 2012, 159 p.

122. **Lauri Sikk.** Computational study of the Sonogashira cross-coupling reaction. Tartu, 2012, 81 p.
123. **Karita Raudkivi.** Neurochemical studies on inter-individual differences in affect-related behaviour of the laboratory rat. Tartu, 2012, 161 p.
124. **Indrek Saar.** Design of GalR2 subtype specific ligands: their role in depression-like behavior and feeding regulation. Tartu, 2013, 126 p.
125. **Ann Laheäär.** Electrochemical characterization of alkali metal salt based non-aqueous electrolytes for supercapacitors. Tartu, 2013, 127 p.
126. **Kerli Tõnurist.** Influence of electrospun separator materials properties on electrochemical performance of electrical double-layer capacitors. Tartu, 2013, 147 p.
127. **Kaija Põhako-Esko.** Novel organic and inorganic ionogels: preparation and characterization. Tartu, 2013, 124 p.
128. **Ivar Kruusenberg.** Electroreduction of oxygen on carbon nanomaterial-based catalysts. Tartu, 2013, 191 p.
129. **Sander Piiskop.** Kinetic effects of ultrasound in aqueous acetonitrile solutions. Tartu, 2013, 95 p.
130. **Ilona Faustova**. Regulatory role of L-type pyruvate kinase N-terminal domain. Tartu, 2013, 109 p.
131. **Kadi Tamm.** Synthesis and characterization of the micro-mesoporous anode materials and testing of the medium temperature solid oxide fuel cell single cells. Tartu, 2013, 138 p.
132. **Iva Bozhidarova Stoyanova-Slavova.** Validation of QSAR/QSPR for regulatory purposes. Tartu, 2013, 109 p.
133. **Vitali Grozovski**. Adsorption of organic molecules at single crystal electrodes studied by *in situ* STM method. Tartu, 2014, 146 p.
134. **Santa Veikšina**. Development of assay systems for characterisation of ligand binding properties to melanocortin 4 receptors. Tartu, 2014, 151 p.
135. **Jüri Liiv.** PVDF (polyvinylidene difluoride) as material for active element of twisting-ball displays. Tartu, 2014, 111 p.
136. **Kersti Vaarmets.** Electrochemical and physical characterization of pristine and activated molybdenum carbide-derived carbon electrodes for the oxygen electroreduction reaction. Tartu, 2014, 131 p.
137. **Lauri Tõntson**. Regulation of G-protein subtypes by receptors, guanine nucleotides and Mn^{2+}. Tartu, 2014, 105 p.
138. **Aiko Adamson.** Properties of amine-boranes and phosphorus analogues in the gas phase. Tartu, 2014, 78 p.
139. **Elo Kibena**. Electrochemical grafting of glassy carbon, gold, highly oriented pyrolytic graphite and chemical vapour deposition-grown graphene electrodes by diazonium reduction method. Tartu, 2014, 184 p.
140. **Teemu Näykki.** Novel Tools for Water Quality Monitoring – From Field to Laboratory. Tartu, 2014, 202 p.
141. **Karl Kaupmees.** Acidity and basicity in non-aqueous media: importance of solvent properties and purity. Tartu, 2014, 128 p.

142. **Oleg Lebedev**. Hydrazine polyanions: different strategies in the synthesis of heterocycles. Tartu, 2015, 118 p.
143. **Geven Piir.** Environmental risk assessment of chemicals using QSAR methods. Tartu, 2015, 123 p.
144. **Olga Mazina.** Development and application of the biosensor assay for measurements of cyclic adenosine monophosphate in studies of G protein-coupled receptor signalinga. Tartu, 2015, 116 p.
145. ***Sandip Ashokrao Kadam.*** *Anion receptors: synthesis and accurate binding measurements. Tartu, 2015, 116 p.*
146. **Indrek Tallo.** Synthesis and characterization of new micro-mesoporous carbide derived carbon materials for high energy and power density electrical double layer capacitors. Tartu, 2015, 148 p.
147. **Heiki Erikson.** Electrochemical reduction of oxygen on nanostructured palladium and gold catalysts. Tartu, 2015, 204 p.